

Structural and Functional Studies on Noxious Stimuli Sensing of the Transient Receptor  
Potential Ankyrin 1 Channel

by

Yang Suo

Department of Biochemistry  
Duke University

Date: \_\_\_\_\_

Approved:

\_\_\_\_\_  
Seok-Yong Lee, Supervisor

\_\_\_\_\_  
Richard G. Brennan

\_\_\_\_\_  
Jörg Grandl

\_\_\_\_\_  
Huanghe Yang

\_\_\_\_\_  
Pei Zhou

Dissertation submitted in partial fulfillment of  
the requirements for the degree of Doctor  
of Philosophy in the Department of  
Biochemistry in the Graduate School  
of Duke University

2021

ABSTRACT

Structural and Functional Studies on Noxious Stimuli Sensing of the Transient Receptor  
Potential Ankyrin 1 Channel

by

Yang Suo

Department of Biochemistry  
Duke University

Date: \_\_\_\_\_

Approved:

\_\_\_\_\_  
Seok-Yong Lee, Supervisor

\_\_\_\_\_  
Richard G. Brennan

\_\_\_\_\_  
Jörg Grandl

\_\_\_\_\_  
Huanghe Yang

\_\_\_\_\_  
Pei Zhou

An abstract of a dissertation submitted in partial  
fulfillment of the requirements for the degree  
of Doctor of Philosophy in the Department of  
Biochemistry in the Graduate School of  
Duke University

2021

Copyright by  
Yang Suo  
2021

## Abstract

Transient receptor potential channel subfamily A member 1 (TRPA1) is a Ca<sup>2+</sup>-permeable cation channel that serves as the primary sensor of environmental irritants, noxious substances, and temperature. Many TRPA1 agonists are electrophiles that are recognized by TRPA1 via covalent bond modifications of specific cysteine residues located in the cytoplasmic domains. TRPA1 is also a temperature activated channel displaying unique species-specific thermo sensitivity. Preceding this work, however, a mechanistic understanding of electrophile sensing by TRPA1 has been limited by a lack of structural information. Moreover, the mechanism by which TRPA1 sense temperature has been elusive.

Using cryo-electron microscopy, we determined the structures of nanodisc-reconstituted human TRPA1 in ligand free state and in complex with the covalent agonists JT010 or BITC at 2.8, 2.9, and 3.1 Å, respectively. Our structural and functional studies provide the molecular basis for electrophile recognition by the extraordinarily reactive Cys621 in TRPA1 and grant mechanistic insights into electrophile-dependent conformational changes in TRPA1. This work illustrates the fundamental principles of irritant sensing in humans at the molecular level and provides a platform for future drug development targeting TRPA1. Moreover, we determined the cryo-EM structure of

rattlesnake TRPA1 in nanodisc-reconstituted condition at 3.3 Å. This structural revealed a novel N-terminal ankyrin repeat domain that was not resolved in previous structures. Our structural and functional studies on rattlesnake TRPA1 provides a framework in understanding the principles of thermo sensitivity in TRPA1.

# Contents

Abstract .....	iv
List of Tables .....	ix
List of Figures .....	x
List of Abbreviations .....	xii
Acknowledgements .....	xv
1. Introduction .....	1
1.1 TRPA1 – An Introduction.....	1
1.1.1 General Introduction to TRP Channels and TRPA1 .....	1
1.1.2 Electrophile Sensing of TRPA1.....	5
1.1.3 Species-specific Temperature Sensitivity of TRPA1 .....	9
1.1.4 Previous Structural Studies of TRPA1.....	17
1.2 Cryo-electron Microscopy: Principles and Common Practices.....	18
1.2.1 Introduction.....	18
1.2.2 Common workflow of cryo-EM .....	24
2. Structural Basis of Electrophile Irritant Sensing by Human TRPA1 Ion Channel.....	27
2.1 Biochemical Optimization and Structural Determination of Human TRPA1 for Cryo-EM.....	27
2.2 Overview of the Human TRPA1 Structures .....	31
2.2.1 S1-S2 linker structure and pore helices .....	33
2.2.2 Lipids and the interfacial helix.....	36

2.3 The Electrophile-binding Pocket and Structural Basis for High Reactivity of Cys621 .....	41
2.3.1 JT010 and BITC binding in TRPA1 .....	41
2.3.2 Structural basis of high reactivity of Cys621 in TRPA1 .....	46
2.4 Conformational Changes Upon Ligand Binding .....	49
2.5 Discussion.....	53
2.6 Materials and Methods .....	56
2.6.1 Expression and purification of human TRPA1 .....	56
2.6.2 Nanodiscs Reconstitution.....	58
2.6.3 Cryo-EM Sample Preparation and Data Collection.....	58
2.6.4 Cryo-EM Data Processing .....	60
2.6.5 Model Building and Refinement .....	63
2.6.6 Patch-clamp Electrophysiology in HEK-293 cells.....	65
3. Structural Basis of Heat Sensing by the Rattlesnake TRPA1 Channel .....	67
3.1 Biochemical Optimization of Rattlesnake TRPA1 for Cryo-EM Studies .....	67
3.2 Overall Architecture of Rattlesnake TRPA1 .....	70
3.3 Structural Basis for Heat-dependent Activation of Rattlesnake TRPA1 .....	78
3.4 Discussion.....	80
3.5 Materials and Methods .....	82
3.5.1 Rattlesnake TRPA1 expression, purification and nanodiscs reconstitution .....	82
3.5.2 Cryo-EM sample preparation, data collection and data processing .....	83

3.5.3 Two-electrode voltage clamp electrophysiology in <i>X. laevis</i> oocytes .....	85
4. Conclusions.....	87
Appendix A: Supplementary Figures .....	90
References .....	100
Biography.....	112

## List of Tables

Table 1: Cryo-EM data collection, refinement and validation statistics for human TPRA1 structures.....	30
Table 2: Cryo-EM data collection, refinement and validation statistics for rattlesnake TPRA1 structures .....	69

## List of Figures

Figure 1: Phylogenetic tree of human TRP channels. ....	2
Figure 2: TRPA1 agonists.....	8
Figure 3: A chemical model for cysteine modification of TRPA1 by JT010 and BITC .....	9
Figure 4: Evolutionary scheme of TRPA1 and TRPV1. ....	11
Figure 5: TRPA1 heat sensing modules. ....	16
Figure 6: Biochemical and initial cryo-EM characterization of human TRPA1. ....	28
Figure 7: Overview of hTRPA1 structures. ....	32
Figure 8: S1-S2 linker and pore structures of TRPA1.....	35
Figure 9: Lipids in TRPA1.....	39
Figure 10: JT010 and BITC binding in TRPA1.....	44
Figure 11: Density around the ligand binding site in TRPA1 <sub>WT-JT010</sub> and TRPA1 <sub>WT-BITC</sub> . ....	45
Figure 12: The architecture of the electrophile binding pocket endows C621 with high reactivity.....	48
Figure 13: Conformational changes in the electrophile binding pocket and the CD upon JT010 and BITC binding.....	51
Figure 14: Proposed electrophile sensing mechanism for TRPA1. ....	56
Figure 15: Overall architecture of rattlesnake TRPA1. ....	71
Figure 16: The ARD-ARD interface could potentially be critical for temperature sensing. ....	75
Figure 17: rsTRPA1 ARD appears to be twisted comparing to other ankyrin repeats. ....	76
Figure 18: Proposed mechanism for rsTRPA1 heat activation. ....	82

Figure 19: Sequence alignment between human and rattlesnake TRPA1. ....	90
Figure 20: Overview of human TRPA1 cryo-EM data processing. ....	91
Figure 21: Cryo-EM density coverage around key structural elements in human TRPA1 reconstructions. ....	92
Figure 22: Comparison with the previously published structure of human TRPA1 (PDB ID 3J9P). ....	93
Figure 23: Electrophysiology characterization of hTRPA1. ....	94
Figure 24: Electrophysiology characterization of hTRPA1. ....	96
Figure 25: COCOMAPS analysis of rsTRPA1 interactions. ....	98
Figure 26: rsTRPA1 cryo-EM data processing. ....	99

## List of Abbreviations

AITC	Allyl isothiocyanate
AR(D)	Ankyrin repeat (domain)
ATP	Adenosine triphosphate
BITC	Benzyl isothiocyanate
BME	$\beta$ -mercaptoethanol
CC	Coiled coil
CCD	Charge coupled device
CD	Coupling domain (of TRPA1)
cDNA	Complementary deoxyribonucleic acid
CTD	C-terminal domain
CTF	Contrast transfer function
DED	Direct electron detection (camera)
DQE	Detective quantum efficiency
DRG	Dorsal root ganglia
DTT	Dithiothreitol
EC <sub>50</sub>	Half-maximum effective concentration
EM	Electron microscope/electron microscopy

FSC	Fourier shell correlation
FSEC	Fluorescent size exclusion chromatography
GlcNAc	N-acetylglucosamine
GnTI	N-acetylglucosaminyltransferase I
HEK	Human embryonic kidney
HSP70	Heat shock protein 70kDa
IFH	Interfacial helix (of TRPA1)
InsP <sub>6</sub>	Inositol hexaphosphate
LC-MS	Liquid chromatography – Mass spectrometry
NMR	Nuclear magnetic resonance
NOMPC	No mechanoreceptor potential C
PDB	Protein Data Bank
PH	Pore helix
PI(4,5)P <sub>2</sub>	Phosphatidylinositol-(4,5)-bisphosphate
POPC	(1-palmitoyl-2-oleoyl-sn-glycero-3-phosphocholine
POPE	1-palmitoyl-2-oleoyl-sn-glycero-3-phosphoethanolamine
POPG	1- palmitoyl-2-oleoyl-sn-glycero-3-phospho-(1'-rac-glycerol)
RELION	Regularised Likelihood Optimisation

SDS-PAGE	Sodium dodecyl sulphate polyacrylamide gel electrophoresis
SEC	Size-exclusion chromatography
SNR	Signal-to-noise ratio
TCEP	Tris(2-carboxyethyl)phosphine
TEVC	Two-electrode voltage clamp
TG	Trigeminal ganglia
TM	Transmembrane helix
TMD	Transmembrane domain
TRP	Transient receptor potential
TRPA1	Transient receptor potential ankyrin 1
TRPV	Transient receptor potential vanilloid
VSLD	Voltage sensor-like domain
WT	Wild-type

## Acknowledgements

This work would have not been possible for the incredible contribution and support from many people. First and foremost, I would like to express my gratitude for my mentor and advisor, Seok-Yong Lee, for his support and guidance for the past few years during my graduate work. I would also like to thank my lab mates in the Lee Lab, for their advice and help and on both science and life: Zachary Johnson, Ben Chung, Lejla Zubcevic, Ellene Mashalidis, Jiho Yoo, William Borschel, Marshca Hirschi, Alvin Kuk, Ying Yin, Nicholas Wright, Aili Hao, Dohoon Kwon, Justin Fedor and Feng Zhang. I would also like to express my gratitude for my thesis committee members for the valuable feedback on my progress and insight: Richard Brennan, Jörg Grandl, Huanghe Yang and Pei Zhou.

I would also like to acknowledge Lejla Zubcevic for advising and guiding me since my rotation, and the participation of human TPRA1 work including initial biochemistry, and manuscript preparation. I give special thanks to our collaborators, including Mario Borgnia and Allen Hsu, for their collaboration on cryo-EM, Ru-Rong Ji group and for their collaboration on electrophysiology. To the staff at Duke University Shared Materials Instrumentation Facility for the cryo-EM resource: Mark Walters and Michelle Plue. Last but not least, I would also like to thank my family and friends who have been always with me at all times, on this long and wonderful journey.

# 1. Introduction

## 1.1 *TRPA1 – An Introduction*

### 1.1.1 General Introduction to TRP Channels and TRPA1

The ability to sense and respond to noxious environmental stimuli is essential for the survival of animals. These noxious stimuli can be thermal (heat or cold), mechanical, or chemical (e.g. capsaicin, mustard oil). In mammals, the sensation of pain, or nociception, is perceived by a class of primary sensory neurons termed nociceptors, which originate in the dorsal root ganglia (DRG) and trigeminal ganglia (TG). To date, many receptors that are responsible to pain sensing have been identified. Among them, the transient receptor potential (TRP) channels are considered to be as one of the most important family of receptors, as many TRP channels are critically involved in the generation of pain sensation [1].

By their sequence homology, vertebrate TRP channel superfamily can be split into two groups, and further, six families. The group 1 consists of TRPA (ankyrin), TRPC (canonical), TRPM (melastatin), TRPV (vanilloid) families, group 2 contains TRPML and TRPP families (Figure 1). The TRP channel superfamily all share similar six transmembrane segment topology, and most of them are non-selective cation channels. However, TRP channel families share little homology which gives rise to their distinct functions throughout the body.

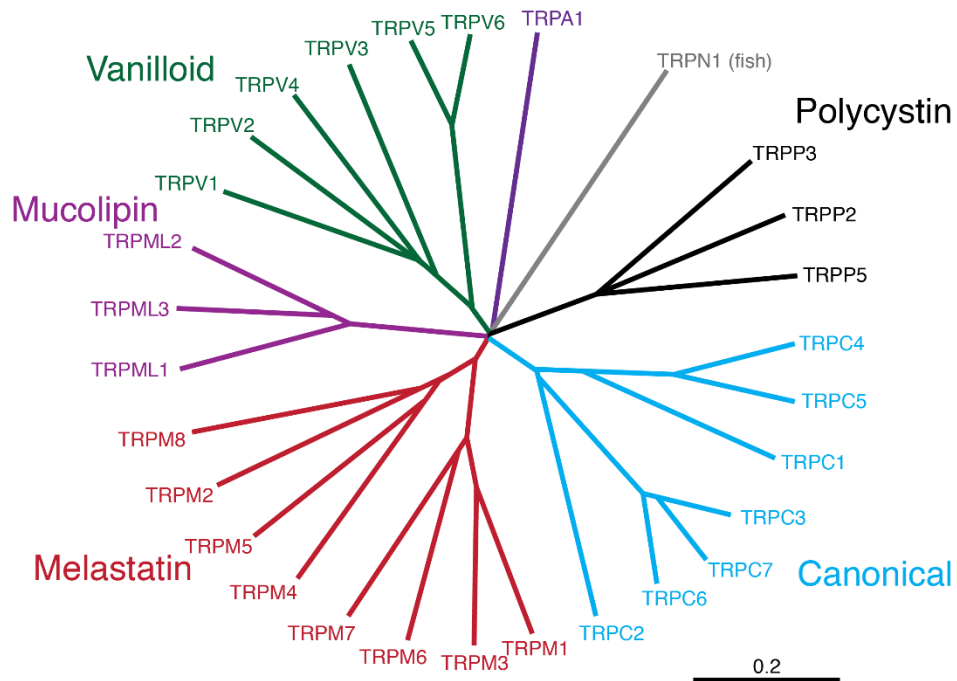


**Figure 1: Phylogenetic tree of human TRP channels.**

A phylogenetic tree of TRP channels. Phylogenetic distances were calculated using PAM matrix. The scale bar represents 0.2 substitutions. Figure adopted from [2].

TRPA1 was first identified in cultured human fibroblasts [3]. It was initially named ANKTM1 (ankyrin-like transmembrane protein) due to its characteristic 14-16 ankyrin repeat domains in the N-terminus [3]. It was later classified as a TRP channel and renamed TRPA1 [4], and remains the sole member of mammalian TRPA subfamily to date. In sensory neurons, TRPA1 is mainly expressed in small-diameter C- or A $\delta$ -primary afferent fibers of DRG and TG, with slight species-specific expression levels among mammals [5]. TRPA1 expression often largely overlaps with TRPV1, although TRPV1-absent TRPA1 expression does exist [6]. Noxious heat sensitization triggered by

bradykinin has been shown to be dependent on both TRPA1 and TRPV1, demonstrating their potentially close relationship in nociception [7]. It was suggested that the Ca<sup>2+</sup> influx via TRPV1 could activate TRPA1. Because of the Ca<sup>2+</sup> sensitivity, TRPA1 has also been suggested to act as an amplifier to TRPV1 [7, 8]. Recently, it was reported that TRPV1 and TRPA1 can form functional hetero-tetramers [9, 10], providing another interesting aspect to the interplay between these two channels.

Mammalian TRPA1 has long been recognized as the primary sensor for noxious chemicals that elicit pain, itch, and neurogenic inflammation. These noxious chemicals vary from pungent irritants such as mustard oil (allyl isothiocyanate, AITC), garlic-derived allicin and cinnamaldehyde to the environmental irritant acrolein and endogenous allogenens including 4-hydroxynonenal [7, 11-17]. TRPA1 is associated with inflammatory pain and chronic itch syndromes and is therefore a validated therapeutic target for treatment of these disease conditions [18-25]. A rare autosomal dominant channelopathy, Familial Episodic Pain Syndrome (FEPS) was recently found to be associated with a TRPA1 gain-of-function mutation, Asn855Ser [26].

Because of the physiological and therapeutic importance of TRPA1, great effort has been made to understand the mechanisms by which noxious chemicals bind and activate the TRPA1 channel [12, 27, 28]. Studies have shown that many TRPA1 agonists possess electrophile moiety which activate the channel via covalent modification of specific cysteine residues in the cytoplasmic domains of TRPA1 [12, 27, 28]. Notably,

TRPA1 electrophile agonists are structurally and chemically diverse and they participate in both reversible (thiol-Michael adduct formation) and irreversible (nucleophilic SN2 reaction and thiol- $\alpha,\beta$ -unsaturated aldehyde reaction) cysteine modification reactions [12, 28].

Activation of TRPA1 elicits both pain and itch in animal models. AITC was found to elicit pain and neurogenic inflammation after intradermal injection through the activation of TRPA1 [29]. Some agonists, however, activates TRPA1 but elicits physiological effects in a biased manner. Recently, Han et al. discovered a micro-RNA (miRNA), miR-711, that binds and activates TRPA1. Electrophysiology results showed that miR-711 and was able to activate TRPA1 in both heterologously expressed systems and cultured DRG neurons. Moreover, a mouse model demonstrated that miR-711 elicits pruritus via interaction and activation with TRPA1 [21]. While the conventional TRPA1 activator, AITC can elicit both pain and itch in a dose-dependent manner, miR-711 only induces itch in mice. The authors speculated that this biased signaling effect is due to the rapid transient activation by TRPA1 from the extracellular side [21]. More recently, Liu et al. discovered GNE551, to be a potent non-covalent TRPA1 agonist [30]. Interestingly, although GNE551 elicits pain in mouse models similar to AITC, GNE551-induced pain is much less sensitive to antagonist treatment compared to AITC-induced pain. This also indicates that GNE551 and AITC activates TRPA1 through different pathways. Moreover, a recently characterized TRPA1-activating scorpion toxin showed

a biased signaling behavior where it elicits pain without neurogenic inflammation [31]. Taken together, the notion of biased agonism of TRPA1 channels has been developing rapidly and may have profound implication to TRPA1-targeted drug development.

Because of the great interest in physiology and pharmacology on TRPA1, various topics regarding TRPA1 have been extensively reviewed over the past few years [5, 32-41].

### **1.1.2 Electrophile Sensing of TRPA1**

The sensing of environmental irritants is considered to be the major functionality of mammalian TRPA1. Mustard oil (AITC) has been used to elicit acute pain in animal models and thus a search was performed in effort to locate the “wasabi receptor” gene from a rat TG cDNA library [13]. This led to the discovery of TRPA1 as the ionotropic receptor of mustard oil and cannabinoids [13]. Shortly after, two notable independent studies identified several cysteine residues important for electrophile activation of TRPA1. Using mutagenesis screening, Hinman et al. located three conserved cysteine residues (Cys621, Cys641, and Cys665, numbered according to human TRPA1 sequence) underlie electrophile activation of TRPA1 [12]. Using mass spectrometry and mutagenesis studies, Macpherson et al. found three cysteine residues (Cys414, Cys421, and Cys621, numbered according to the human TRPA1 sequence) that are important for electrophile-dependent TRPA1 activation [42]. The cysteine residues identified by these

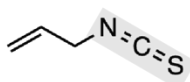
studies, albeit using different experimental methods, did not overlap entirely, but both indicated a critical role of Cys621 in TRPA1 channel gating by covalent-modification [12, 42]. The critical role of Cys621 is further highlighted by recent studies of multiple African rodents that evolved to be resistant to environmental irritants [43]. A recently identified TRPA1 agonist, JT010 (*2-chloro-N-(4-(4-ethoxyphenyl)thiazol-2-yl)-N-(3-methoxypropyl)acetamide*) is a highly selective and potent activator [44]. Mutagenesis studies revealed that JT010 modifies Cys621 with high specificity. JT010 has been shown to be a useful validation tool for TRPA1-specific pain model [45], rendering it a valid target for structural analysis as well.

The discovery that electrophile sensing by TRPA1 takes place through covalent modification of cysteine residues on the cytoplasmic side of the TRPA1 poses an intriguing question. The eukaryotic cytosol is rich in cysteine-containing antioxidants (e.g. ~ 5 mM glutathione) that react with electrophiles to alleviate oxidative stress [46], which suggests that process of electrophile detection by TRPA1 is much more efficient than that by cysteine-containing antioxidants. Therefore, TRPA1 must have developed a high-performing and sophisticated electrophile sensing apparatus, which is critical for nociceptive signaling in humans [27]. However, the molecular basis for its high reactivity remains unclear. It is also worthy to note that while the electrophilic agonists of TRPA1 have great diversity in chemical structure (Figure 2), it is also unclear how Cys621 can undergo different types of covalent modifications by a range of structurally

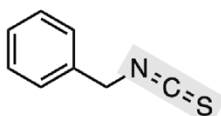
diverse electrophiles and how such covalent modifications might trigger channel activation (Figure 3).

## Covalent TRPA1 agonists

Reversible  
thiol-Michael adduct formation

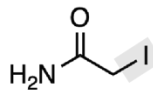


Allyl isothiocyanate  
(AITC)

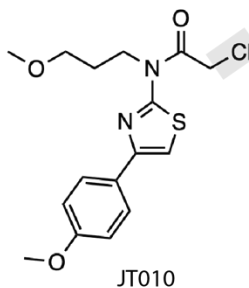


Benzyl isothiocyanate  
(BITC)

Irreversible  
Nucleophilic-SN2 reaction

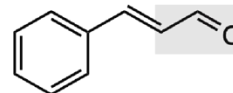


Iodoacetamide

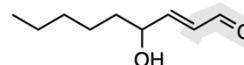


JT010

Irreversible  
thiol- $\alpha,\beta$ -unsaturated  
aldehyde reaction

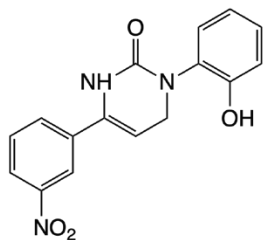


Cinnamaldehyde

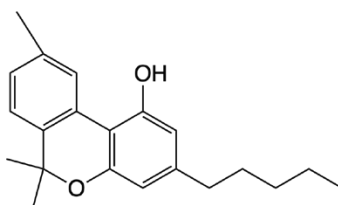


4-Hydroxynonenal

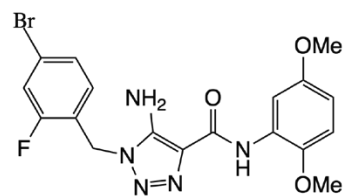
## Non-covalent TRPA1 agonists



Icilin



Cannabinol



GNE-551

**Figure 2: TRPA1 agonists.**

Examples of TRPA1 agonists, classified by their model of action and chemical nature.

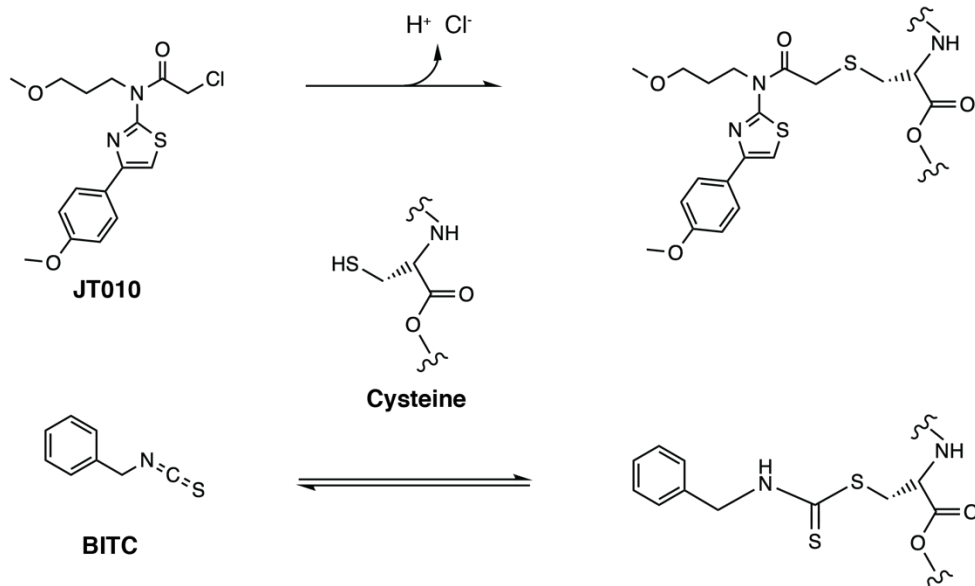


**Figure 3: A chemical model for cysteine modification of TRPA1 by JT010 and BITC**

### 1.1.3 Species-specific Temperature Sensitivity of TRPA1

In mammals, the ability to sense temperature change is enabled by the expression of a group of TRP channels that can be activated by either cold or heat. TRP vanilloid (TRPV) 1-4, namely thermoTRP channels, are well-known for their role in sensing noxious heat [47]. Nonetheless, the role of TRPA1 plays in temperature sensing has been controversial. Even before TRPA1 was identified to be sensitive to noxious compounds, it was already suggested that mouse TRPA1 is a putative sensor for noxious cold temperature [4]. Interestingly, functional comparison of TRPA1 among invertebrate and vertebrate species showed great diversity in thermal sensitivity. Human TRPA1 was shown to be either activated by cold or displays a U-shaped thermo

sensitivity where it can be activated by either warm or cold temperatures [48]. Rodent TRPA1 was clearly shown to be activated by cold [4, 42, 49]. In sharp contrast, heterologously expressed chicken and snake TRPA1 is activated by heat [50, 51]. Heterologously expressed zebrafish TRPA1 could be activated by both heat and cold, but TRPA1-knockout zebrafish do not exhibit behavioral anomalies in response of heat or cold [52]. These discrepancies suggest that the physiological role of temperature sensitivity of TRPA1 needs to be further scrutinized.

Evolutionary analysis pointed out that the chemical sensing can be traced down to an ancient modality of TRPA1, but it remains unclear whether the ancestral TRPA1 was temperature sensitive. Comparative analysis suggests that TRPA1 and TRPV1 co-evolved their temperature sensing capabilities allowing adaption to changing thermal environments [38]. While heat-induced response of TRPV1 remains relatively conserved among species, TRPA1 has been tuned to lean to either chemical or temperature modalities in different species (Figure 4). In mammals, for example, TRPA1 has high electrophile chemical sensitivity while temperature sensitivity is relatively low. In insects and vertebrate ectotherms, however, the chemical sensitivity was downgraded to a minimum to enhance temperature signaling of TRPA1 [53].

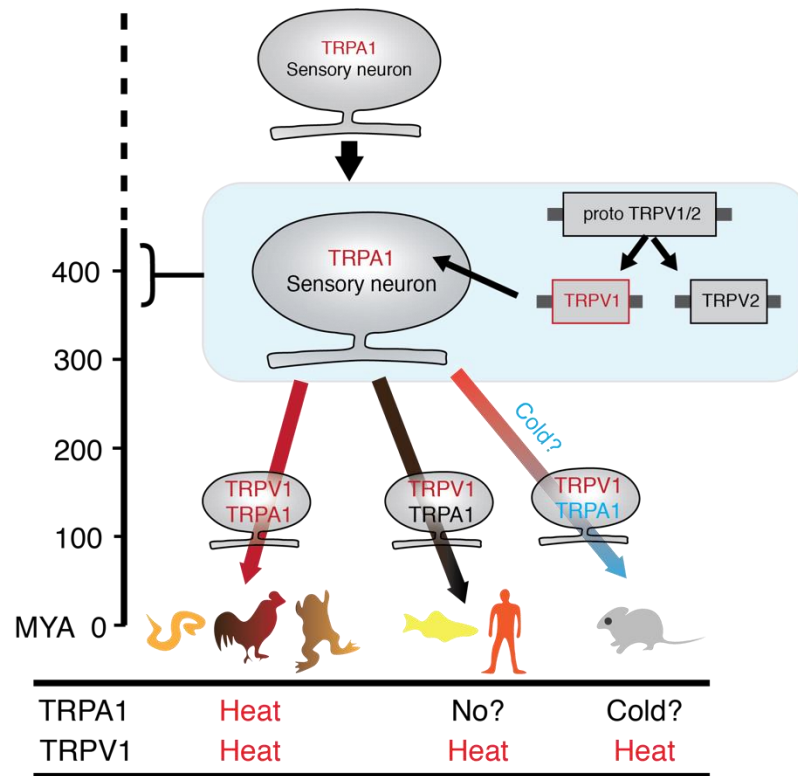


**Figure 4: Evolutionary scheme of TRPA1 and TRPV1.**

TRPA1 was likely appeared first as a polymodal sensor for temperature and chemicals. Subsequently, TRPV1 emerged as a heat sensor. MYA: million years ago. Figure adopted from [38]

Mouse TRPA1 was the first TRPA1 homolog found to be temperature sensitive.

Story et al. reported that the mouse ortholog TRPA1 could be activated in the sub-TRPM8 range temperature (<17 °C) [4]. However, contradictory results were soon reported to either support [11, 54] or to dispute [55] the notion of cold activation of rodent TRPA1. Furthermore, several studies of TRPA1 knockout mice lines resulted in a lack of clear evidence of TRPA1 acting as a temperature sensor in vivo [8, 56, 57], as the

knockout mice displayed no clear abnormal phenotype in terms of temperature regulation.

The role of temperature activation of human TRPA1 has been disputed and many groups have reported contradictory results over the past decade [32] under different experimental conditions. Recently, Chen et al. reported a side-by-side analysis of TRPA1 from human, mice, and rats. Interestingly, they found that under identical conditions, rodent TRPA1 showed cold activation while primate TRPA1 channels were insensitive to thermal stimuli [58]. To add more controversies to the issue, Moparthy et al. reported that purified human TRPA1 inserted in lipid bilayers displays an inherent U-shaped thermosensitivity, in which it can be activated by both cold and hot temperatures [48]. In conclusion, the solid evidence in which human TRPA1 is involved in temperature sensing still awaits further elucidation.

Soon after the discovery of mouse TRPA1, *Drosophila melanogaster* TRPA1 (dTRPA1) ortholog was cloned and found to be a heat activated channel. Like the mouse TRPA1, dTRPA1 was sensitive to AITC and electrophilic compounds. In stark contrast to mouse TRPA1, however, dTRPA1 was found to be able to be activated by a warm temperature between 27-29 °C [59]. *In vivo* experiments showed that the thermal activation of dTRPA1 plays a crucial role in chemotaxis and temperature preference in both larvae [60] and adult flies [61]. Many behavioral studies suggested that dTRPA1

functions as both a detector and contributes to avoidance of heat and noxious chemicals [60-62].

It is critical for insects to distinguish between the activation of TRPA1 by electrophiles and by heat. Insects achieve this discrimination through the spatially localized splice variant isoforms of TRPA1. For example, there has been two identified dTRPA1 variants, namely dTRPA1A and dTRPA1B, which differ by alternative N-termini. While both isoforms exhibit similar electrophile sensitivity, the TRPA1A isoform is significantly less thermosensitive, with the temperature coefficient ( $Q_{10}$ ) values being ~9 and ~116, for dTRPA1A and dTRPA1B, respectively [59]. Moreover, the less thermal sensitive TRPA1A is mainly expressed in proboscis, where the chemosensitive neurons are located. In comparison, dTRPA1B is expressed within the head of the fly where temperature sensors are located [59]. This spatial difference in dTRPA1 isoform expression helps the fly process and respond to chemical and temperature stimuli properly.

Some insects use thermal signal to locate warm-blooded animals for prey. Those organisms use similar strategy like *Drosophila* to effectively separate the TRPA1 thermal and chemical signals. The malaria host, *Anopheles gambiae*, for example, expresses two splice variants of TRPA1 (AgTRPA1A and AgTRPA1D) with different  $Q_{10}$  values [63]. This diverse TRPA1 variant expression pattern and their functional fine-tuning is required not only for localization of the prey, but also avoidance of high noxious

temperatures for mosquitos [64] . In addition, since mosquito TRPA1 can be robustly activated by electrophiles, it can also serve as a potential target for development of effective mosquito repellents [63].

The studies on thermo sensitivity of vertebrate ectotherms were pioneered by David Julius and colleagues. Many species in the *Viperidae* family, including rattlesnakes and rat snakes, possess the abilities of infrared vision which they use to detect warm-blooded prey even in dark. These vipers are able to superimpose visible and infrared vision in the brain and it enables them to track their prey with great precision and speed [65]. The snake infrared vision is mediated by a highly specialized loreal pit organ between the eye and nostril on the viper's face. The membrane within the pit was found to be the infrared sensor and is highly vascularized, densely innervated by primary afferent nerve fibers from the trigeminal (TG) nerves. Gracheva et al. chose the western diamondback rattlesnake (*Crotalus atrox*) and rat snake as subjects of interest, because they possess the pit organ and is highly effective in terms of infrared vision [51]. Interestingly, by transcriptome analysis and *in situ* hybridization, significantly high levels of TRPA1 expression were found in rattlesnake TG nerves, while only low TRPA1 expression was found in DRG neurons [51]. As a comparison, TRPV1, a closely related TRP channel, was found in both TG and DRG neurons. The rattlesnake TRPA1 was subsequently cloned for characterization. It was then demonstrated that rattlesnake TRPA1 is sensitive to heat with the threshold at 27.6 °C with a  $Q_{10} = 13.7$ , when

heterologously expressed in HEK293 cells [51]. Interestingly, rattlesnake TRPA1 showed a significantly lower sensitivity to AITC compared to mammalian TRPA1, despite the conserved cysteines being present in snake TRPA1 genes. This inverse relationship indicated the process of evolutionary tuning of chemo- versus thermosensation of TRPA1 in different species [51].

Despite recent reports that human TRPA1 can act as a heat sensor even without its cytoplasmic ankyrin repeat domain [66], efforts have been made over the years to identify a temperature sensor module throughout the whole channel protein. As introduced in section 1.1.1, TRPA1 contains long 14-16 ankyrin repeats in its N-terminus. More interestingly, rattlesnake TRPA1 was heat sensitive, while mammalian TRPA1 was shown to be cold-sensitive, despite rather high sequence similarity (human and rattlesnake TRPA1 share 61% amino acid sequence identity and 85% similarity) [67]. Taking advantage of this diversity, Cordero-Morales et al. utilized chimeric studies to further dissect the heat sensing module in TRPA1 [68]. By investigating a series of chimeras between human, rattlesnake, rat snake and drosophila TRPA1, they identified that the heat sensitivity can be conferred solely by N-terminal ankyrin repeat domain (ARD). Specifically, ankyrin repeat AR10-15 can confer the majority of heat sensitivity, while the AR3-8 alone could not bring heat sensitivity alone but could enhance the sensitivity with the presence of ARD 10-15. Based on these results, Cordero-Morales et al. termed AR 10-15 as the primary heat sensing module, with AR 3-8 as the enhancer

module [68] (Figure 5). Furthermore, many studies have supported the notion of the ARD as heat sensing module in TRPA1 as well [59, 69, 70].

Utilizing mutational screening and patch-clamp electrophysiology, Jabba et al. identified that three single mutations on AR6, most notably Ser250Asn, can independently reverse mouse TRPA1 thermo sensitivity from cold to warm sensitive while did not significantly affecting other channel behavior such as chemical sensitivity and channel expression [67]. All temperature dependence altering mutations they reported clustered on AR6, which suggested the critical role of AR6 in thermal sensitivity.

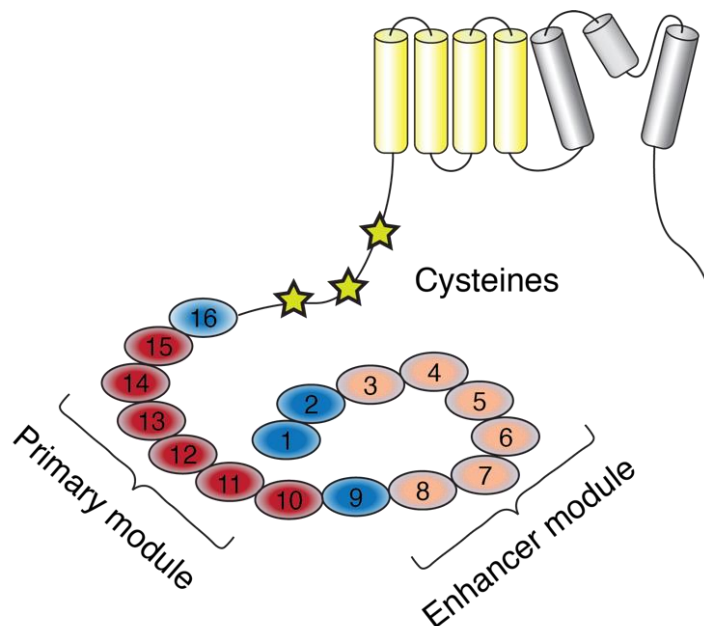


**Figure 5: TRPA1 heat sensing modules.**

Ankyrin repeats in red indicates the primary heat sensing module, and the pink indicates enhancer modules. Reactive cysteines are represented as stars. Adopted from [68]

The molecular mechanism by which TRPA1 and other thermoTRP channels respond to heat remains controversial. Clapham and Miller proposed that the temperature-dependent gating of TRP channels are driven by changes in heat capacity and partial unfolding [71]. This theory predicted that TRP channels should be both heat and cold activated. To date, however, there has been only one report on such dual thermosensitivity in TRP channels [48]. Additionally, it was proposed that 40-80 residues (10-20 residues per protomer for tetrameric TRP channels) are required to undergo change in solvation states in order to generate a sufficient heat capacity change for channel gating [71]. Given the high sequence homology among TRPA1 homologs, it was also believed that the species-specific difference in thermo sensitivity properties are likely a result of differences in allosteric coupling mechanisms between the temperature sensor and the gate, and not from the differences between structural rearrangements upon temperature change [72]. In conclusion, the specific heat sensitivity of rsTRPA1 renders it an interesting subject for structural studies.

#### **1.1.4 Previous Structural Studies of TRPA1**

In 2015, Paulsen et al. [73] reported the first cryo-EM structures of human TRPA1. These structures were one of the first sub-6 Å cryo-EM structures reported, highlighting advancements in the “resolution revolution”. The structures revealed several unexpected features. First, a TRP-like helix domain was found in close position to the Pre-S1 helix, after the transmembrane helix S6. Given that the TRP-like helix is

positioned between the pore and electrophile binding site, the authors believed that the TRP-like helix is likely to be the nexus for allosteric coupling [73]. Second, a long tetrameric coiled coil domain was found beneath the helix bundle gate, located in the C-terminus of the protein. The coiled-coil is stabilized by extensive interaction with ankyrin repeat domain, as well as the inositol hexaphosphate additive which was previously reported to stabilize channel activity [74]. The ankyrin repeats 12-16 maintains extensive interaction with coiled-coil and was thus resolved in the structures, while the N-terminal AR1-11 remained to be resolved. Taken together, the structures provided us with a framework for future TRPA1 structure and functional studies.

## ***1.2 Cryo-electron Microscopy: Principles and Common Practices***

### **1.2.1 Introduction**

Throughout modern history, structural biology has contributed substantially to our understanding of how biological systems work [75]. To date, three major techniques are available for structural biology: X-ray crystallography, nuclear magnetic resonance (NMR) spectroscopy, and electron microscopy (EM). X-ray crystallography has been the most prominent structural biology method over the past few decades, which contributed majority of atomic coordinates of biomolecules in the Protein Data Bank (PDB) [75]. However, crystallizing protein has been challenging, especially for membrane proteins. The trial-and-error process is tedious and does not always succeed. NMR has been very

successful in resolving the conformational ensembles of proteins or nucleic acids, yet the size limit renders NMR difficult for structural studies for large proteins and complexes.

Historically, EM has been a very useful tool in virology, pathology, microbiology and other fields that investigates the ultrastructure of relatively large specimens, such as tissues, cells and organelles [76]. Determining macromolecular structures by EM has been a challenging task over the past decades, as it poses a few unique challenges. First, the electron beam must be confined in a high vacuum due to their scattering effect with air, thus the sample to be imaged experiences vacuum-induced dehydration, which is usually devastating to biological samples. Moreover, because of the weak interaction between electrons and small atoms including carbon, oxygen, nitrogen, etc., biological samples are usually stained by heavy metal before they could be visible under EM.

In 1974, Taylor and Glaser demonstrated that biomolecules can be maintained in a frozen hydrated state during EM imaging and was able to achieve better than 3Å resolution diffraction [77, 78]. Later, Dubochet et al. developed the plunge freezing technique, where the sample solution is applied on a holey carbon-coated grid and subsequently blotted with a filter paper [79, 80]. The blotting process removed most of the sample from grid, creating an extremely thin layer of sample solution in the holes by surface tension. The grid was then immediately plunged into liquid ethane cooled by liquid nitrogen, during which sample is frozen into a vitreous, amorphous ice with biomolecules embedded in it [79]. The frozen grid is maintained in liquid nitrogen

temperature and was transferred into an electron microscope for imaging. This method is still widely used in sample preparation nowadays, but many of the steps have been automated.

The second challenge electron microscopists faced was the severe radiation damage caused by high-energy electrons. In a 300keV EM, the electrons travel at a fraction of speed of light and carry high energy. Inevitably, the interaction between electrons and biomacromolecules damages the sample. For that reason, the low-dose imaging scheme was developed for radiation damage-prone samples. However the low-dose scheme resulted in a poor signal-to-noise ratio (SNR) of the images. With such a low SNR (and low image contrast), it was not possible to observe high-resolution features of biomolecules from raw micrographs. Frank et al. overcame this problem by averaging many images of the same molecule viewed from the same angle, thus increasing the SNR and providing a better contrast [81]. Moreover, by combining many single images of a same molecule viewed from many angles, it was possible to reconstruct a 3D model from those noisy 2D images of a molecule. The methods to perform plunge-freezing purified sample in vitreous ice, micrograph collection in low-dose, and the 3D reconstruction from individual 2D images, became what we now term “single-particle cryo-electron microscopy” [76]. Jacques Dubochet, Joachim Frank and Richard Henderson shared 2017 Nobel Prize in Chemistry for their contribution in the development of cryo-EM.

In 1995, Henderson predicted that the single particle cryo-EM would be able to achieve atomic resolution [82]. In the past six or seven years, thanks to the development in new techniques, the resolution of cryo-EM 3D reconstruction was able to advance from 30-50 Å resolution in the 2000s, to 1.22 Å resolution most recently [83]. Since 2014, the revolutionary advancement in cryo-EM has been made possible by mainly three breakthroughs: the development of direct electron detection (DED) cameras, the development of Bayesian image processing algorithms, and the automation in data collection strategies [76, 84].

Historically, electron micrographs were recorded and collected using films, which were subsequently developed, digitized and subject to computational analysis. The films had an acceptable performance and were able to produce 3D reconstructions at sub-nanometer resolution [85], but it was difficult to push the resolution further and handling films was tedious thus limiting the throughput of structure determination. In the late 1990s, the charge-coupled device (CCD) cameras were introduced to electron microscopy and allowed data to be collected digitally and automatically. CCD cameras only detect photons so incoming electrons must be converted to photons by hitting a phosphor screen and elicit fluorescence for CCD camera to capture. Because of this conversion process, CCD cameras has a relatively low detective quantum efficiency (DQE) compared to films which is characterized by the fraction of signals retained by a camera at a certain spatial frequency. The introduction of direct election detection (DED,

or DDD, direct detection devices) cameras revolutionized the cryo-EM imaging process and pushed the resolution to sub-4 Å in the early 2010s [86]. DED cameras are designed to detect charging events upon receiving an electron with much higher spatial and temporal accuracy, resulting a substantially higher DQE comparing to CCD cameras. Moreover, the high frame rate DED camera could achieve enabled two major advantages: electron counting, and movie recording [76]. The DED camera could process electron events at a speed fast enough to track every single electron that hits the camera, providing resolution to a pixel, and even sub-pixel level, which even further elevates DQE in both low- and high- frequency. By recording “movie” stacks that consists of dozens of frames over the timespan of a few seconds instead of a single micrograph, while still retaining enough information in each frame for processing, it facilitated many novel image processing techniques to improve image quality and recover more high-resolution information [87]. Most importantly, it enabled the *in silico* correction of beam-induced motion, i.e. subtle sample movements caused by electron beam [87], as well as movie processing, which allowed allows dose fractionation and weighing to mitigate radiation damage [88]. Taken together, the application of DED cameras made obtaining atomic resolution for many proteins possible.

The second major advancement on high resolution cryo-EM was the development of novel image processing algorithms. A very high sample homogeneity and accurate image alignment are required for high-resolution 3D reconstruction. Thus,

the classification and alignment of particle images are critical for a successful 3D reconstruction. Because cryo-EM images typically have very low SNR and potentially high heterogeneity, Frank and his colleagues developed a maximum likelihood based probabilistic approach to properly classify and align those images [89]. In 2012, a novel Bayesian approach to cryo-EM image processing was proposed by Scheres and later implemented in RELION software [90, 91]. Unlike the maximum likelihood approach, the Bayesian approach gives uncertainty to each classification and alignment assignment. Subsequently, the uncertainty for each assignment was optimized to be reduced throughout repeated iterations. Using this method, the accuracies in image classification and alignment were much improved and resulted in a higher resolution 3D reconstruction [90]. The introduction of Bayesian approach and DED camera coincided around the same time and pushed single particle cryo-EM to atomic resolution.

As discussed before, large amount data is required to obtain a high-resolution EM reconstruction due to sample heterogeneity and low SNR in single particle images. Typically, thousands of micrographs in high quality are needed for one single reconstruction, which were collected over a timespan of days. Before the data collection could be automated, a highly skilled and patient operator was required for data collection. Luckily, this problem was alleviated by the development of several automated data acquisition methods such as SerialEM [92], Legion [93], autoEMation [94], and more recently, EPU (FEI) and Latitude S (Gatan). These software packages

have reduced the time and financial costs to EM data acquisition and made large-scale datasets accessible.

### **1.2.2 Common workflow of cryo-EM**

Compared to X-ray crystallography, which requires samples with very high homogeneity and stability, requirements for sample quality in cryo-EM studies are less demanding, allowing for structural determination of proteins with relatively higher instability and flexibility. In our experience, however, the biochemical behavior of the sample must be optimized to obtain a sub-3Å reconstruction. Although sub-optimal sample quality can often be offset by simply collecting more data, the current scarcity and cost in accessing high-end electron microscopes often discourages prolonged data collection. Thus, preparing sample to the highest purity and homogeneity should still be considered the top priority in single particle 3D cryo-EM reconstruction. Moreover, batch-to-batch consistency is necessary in order to optimize cryo-EM sample freezing conditions so that structures in complex with different ligands/binding partners, etc., may be obtained. [95]. It is critical to maintain consistency throughout different preparations to allow proper interpretation among these data. The sample should appear to be homogeneous by size exclusion chromatography (SEC), SDS-PAGE, and when possible, negative stain EM [96] before one proceeds to prepare cryo-EM samples. To obtain homogenous sample, one may need to find the optimal

expression/purification procedures, buffer conditions, protein concentration, etc. For macromolecular complexes, one may need glutaraldehyde crosslinking, GraFix crosslinking [97] and other crosslinking methods to stabilize complex formation.

The biomacromolecule specimen must be vitrified on a sample support grid before imaging. The most common type of grid is of copper material, coated with a holey carbon film on which the sample will vitrify within holes, forming a thin layer of ice. To deal with the inherent instability and beam-induced motion of vitreous ice in holey carbon films, an additional thin (~2 nm) amorphous carbon or graphene [98] may be coated on top of the holey carbon film, providing additional support for sample. Additionally, a more mechanically stable material, such as gold may be used as grid and film material [99]. Affinity-coated grids can also be used when necessary [100]. Before sample is applied, the grids are rendered hydrophilic by a glow discharger or a plasma cleaner. Sample vitrification is generally performed by a semi-automatic plunger system such as Vitrobot (Thermo Fisher), EM GP (Leica), or Cryoplunge (Gatan). On these machines, the environment in which the sample is applied on the grid and blotting is performed can be specifically controlled, allowing consistency, reproducibility and requirements for special sample treatment.

Before a grid is considered suitable for data collection, one must confirm that the grid is in high quality, which is referred to as screening. A proper vitrified specimen is usually characterized by a layer of amorphous ice thick enough to accommodate

particles while shielding them from the air-water interface, and thin enough to allow high resolution signal to pass through. The particles should appear to be homogenous to eye, and the density of particles needs to be appropriate. Occasionally the particles may adopt a preferred orientation, most often caused by interaction with air-water interface. This issue can be overcome by increasing ice thickness, addition of low concentrations of detergent, or by using a continuous support grid [101].

To obtain high-resolution 3D reconstructions, high quality images must be acquired. To date, a few software packages are available that allow automated data collection which greatly eases the workload for large dataset acquisition. Still many aspects regarding microscope and data acquisition strategy must be taken account to ensure high data quality. First, the microscope optics must be properly aligned to ensure proper optical conditions, including but not limited to the proper use of condenser aperture, minimalization of astigmatism and coma. As for data acquisition strategies, specific parameter regarding data collection, such as the use of objective aperture and energy filter, proper magnification (which determines the pixel size, and in turn determines the resolution cutoff), dose rate, frame number, etc. must be optimized.

## **2. Structural Basis of Electrophile Irritant Sensing by Human TRPA1 Ion Channel**

### ***2.1 Biochemical Optimization and Structural Determination of Human TRPA1 for Cryo-EM***

Using homolog screening assessed by size-exclusion chromatography (SEC), fluorescence size exclusion chromatography (FSEC) and negative-stain single particle electron microscopy, Paulsen et al. identified that human TRPA1 is the best biochemically behaving construct among 10 TRPA1 homologs [73, 102], and most suitable for cryo-EM structural studies.

In order to study the activation mechanisms of hTRPA1 by structurally and chemically different ligands, we conducted cryo-EM experiments in the presence of a reversible covalent agonist benzyl isothiocyanate (BITC) found in the seeds of the papaya plant [103], and the synthetic JT010 compound which selectively modifies Cys621 through an irreversible SN2 reaction [44]. BITC was chosen because it activates hTRPA1 in a similar manner to AITC while contains a bulkier benzyl ring and can therefore be more easily identified and modelled in cryo-EM maps [12].

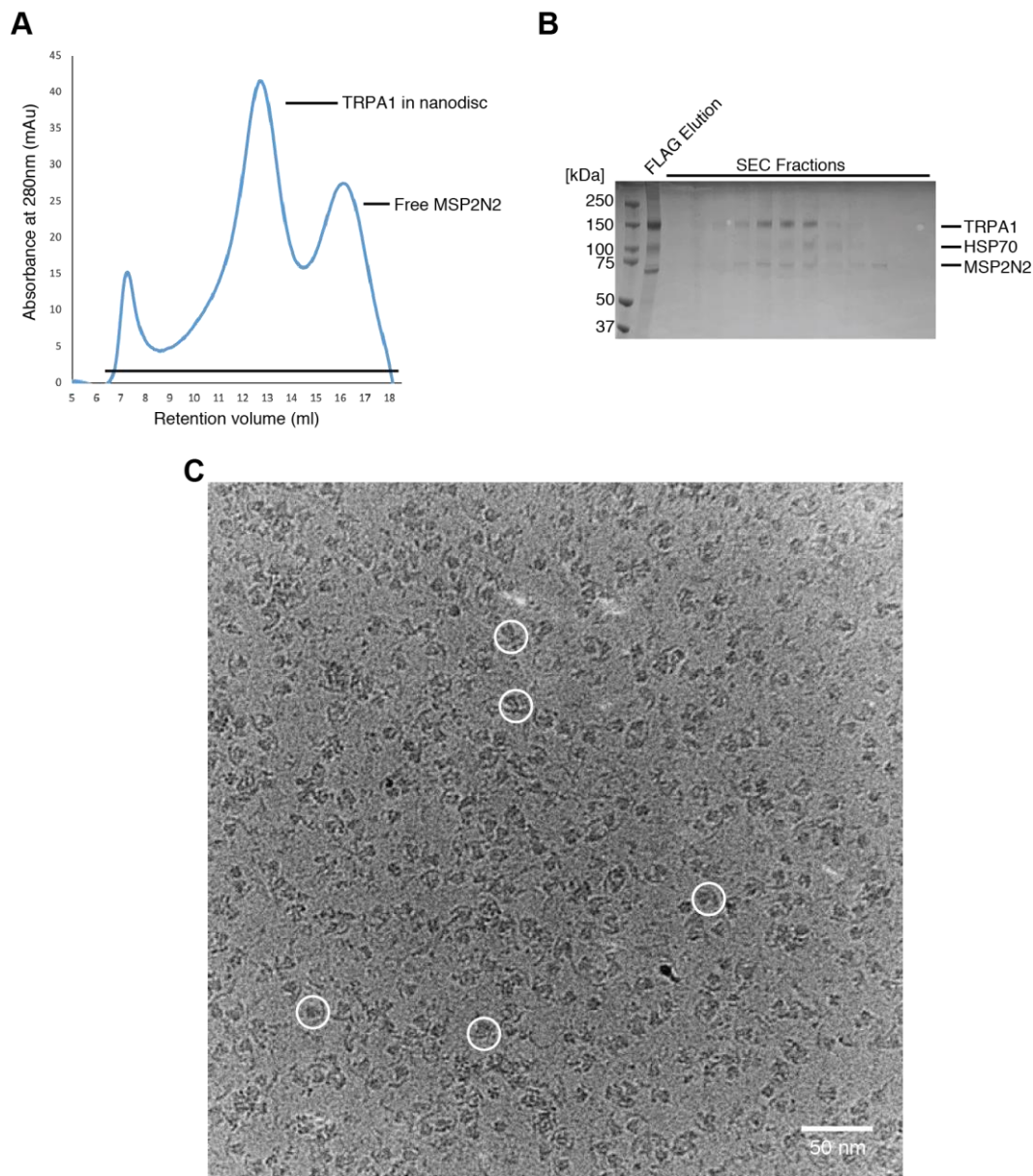


**Figure 6: Biochemical and initial cryo-EM characterization of human TRPA1.**

(A) representative SEC profile of hTRPA1 reconstituted in lipid nanodiscs. (B) SDS-PAGE profile of SEC fractions, corresponding to panel A. (C) Representative cryo-EM micrograph of hTRPA1. Representative hTRPA1 particles are circled out.

TRPA1 activity was known to be regulated by lipids [104, 105]. To visualize protein-lipid interaction and placing protein in a more native environment, the purified wild type TRPA1 channels were reconstituted in lipid nanodiscs and incubated with or without ligands before being freezing onto grids. The structures were then determined by single particle cryo-EM 3D reconstruction (see section 2.6.1, Figures 6 and 7). To obtain a ligand-free state, the Cys621Ser mutation (TRPA1<sub>C621S</sub>) was introduced to silence the reactive electrophile site and prepared the cryo-EM sample without the addition of ligands. The final 3D reconstructions of ligand-free TRPA1<sub>C621S</sub> and the wild type TRPA1 in complex with JT010 (TRPA1<sub>WT-JT010</sub>) and BITC (TRPA1<sub>WT-BITC</sub>), are resolved to 2.8, 2.9, and 3.1 Å, respectively (Figure 7 and Table 1). The overall quality of the 3D reconstructions in the transmembrane region (Figure 21) is excellent, revealing multiple cryo-EM densities corresponding to glycans (Figure 8) and several annular lipid molecules (Figure 9). Consistent with the previous cryo-EM study [73], a significant part of the N-terminal region (AR1-AR11) was not resolved in the cryo-EM reconstructions.

**Table 1: Cryo-EM data collection, refinement and validation statistics for human TPRA1 structures**

	<b>C621S Apo</b> <b>EMD-20451</b> <b>PDB 6PQQ</b>	<b>WT JT010</b> <b>EMD-20449</b> <b>PDB 6PQO</b>	<b>WT BITC</b> <b>EMD-20450</b> <b>PDB 6PQP</b>
<b>Data Collection</b>			
Microscope	Titan Krios	Titan Krios	Titan Krios
Voltage (kV)	300	300	300
Nominal magnification	22,500x	75,000x	22,500x
Electron dose (e <sup>-</sup> Å <sup>-2</sup> )	60	42	60
Exposure rate (e <sup>-</sup> /pixel/sec)	15	0.8	15
Detector	Gatan K3	Falcon III	Gatan K3
Pixel size (Å)	1.07	1.08	1.07
Defocus range (µm)	-2.5 to -0.75	-3.0 to -1.25	-2.5 to -0.75
<b>Reconstruction</b>			
Total extracted particles	1,150,312	752,104	396,597
Final particles	119,697	189,927	74,677
Symmetry imposed	C4	C4	C4
Resolution (global)	2.81 Å	2.88 Å	3.06 Å
FSC 0.5 (unmasked/masked)	3.59/3.21 Å	3.41/3.14 Å	3.90/3.45 Å
FSC 0.143 (unmasked/masked)	3.10/2.81 Å	3.07/2.88 Å	3.41/3.06 Å
Applied B-factor (Å <sup>2</sup> )	-30	-30	-30
<b>Refinement</b>			
Protein Residues	2,416	2,448	2,464
Ligand	28	40	36
Map correlation coefficient	0.84	0.84	0.85
R.m.s deviations			
Bond lengths (Å)	0.005	0.007	0.008
Bond angles (°)	0.896	0.950	0.999
Ramachandran plot			
Outliers	0.00%	0.00%	0.00%
Allowed	3.20%	3.48%	4.11%
Favored	96.80%	96.52%	95.89%
Poor rotamers	0.00%	0.00%	0.00%
MolProbity score	1.18	1.33	1.38
All-atom Clashscore	2.13	3.09	3.02

## **2.2 Overview of the Human TRPA1 Structures**

The overall resolved structure of the homotetrameric human TRPA1 (hTRPA1) channel can be divided into three layers: the top, middle and bottom layer. The top layer is composed of the transmembrane domain (TMD), while the middle layer contains the coupling domain (CD) and the bottom layer consists of the ankyrin repeat domain (ARD). The TMD is composed of the voltage-sensor like domain (VSLD, S1-S4) and the pore domain (S5, S6, and pore helix PH) arranged in a domain-swapped manner. The N- and C-termini form a two-layered cytoplasmic assembly. The CD, which forms the middle layer, is composed of 8 short helices (H1-H7 and pre-S1), a  $\beta$ -sheet (we term  $\beta_{CD}$ ) composed of three  $\beta$  strands ( $\beta_{1.1}$ -  $\beta_{1.3}$ ), and the TRP-like helix (termed TRPL hereafter) (Figure 7G). Ankyrin repeats 11-16 (AR11-AR16) from four subunits surround the central tetrameric C-terminal coiled coil, resulting in the stabilization and visualization of the ARD (Figure 7).

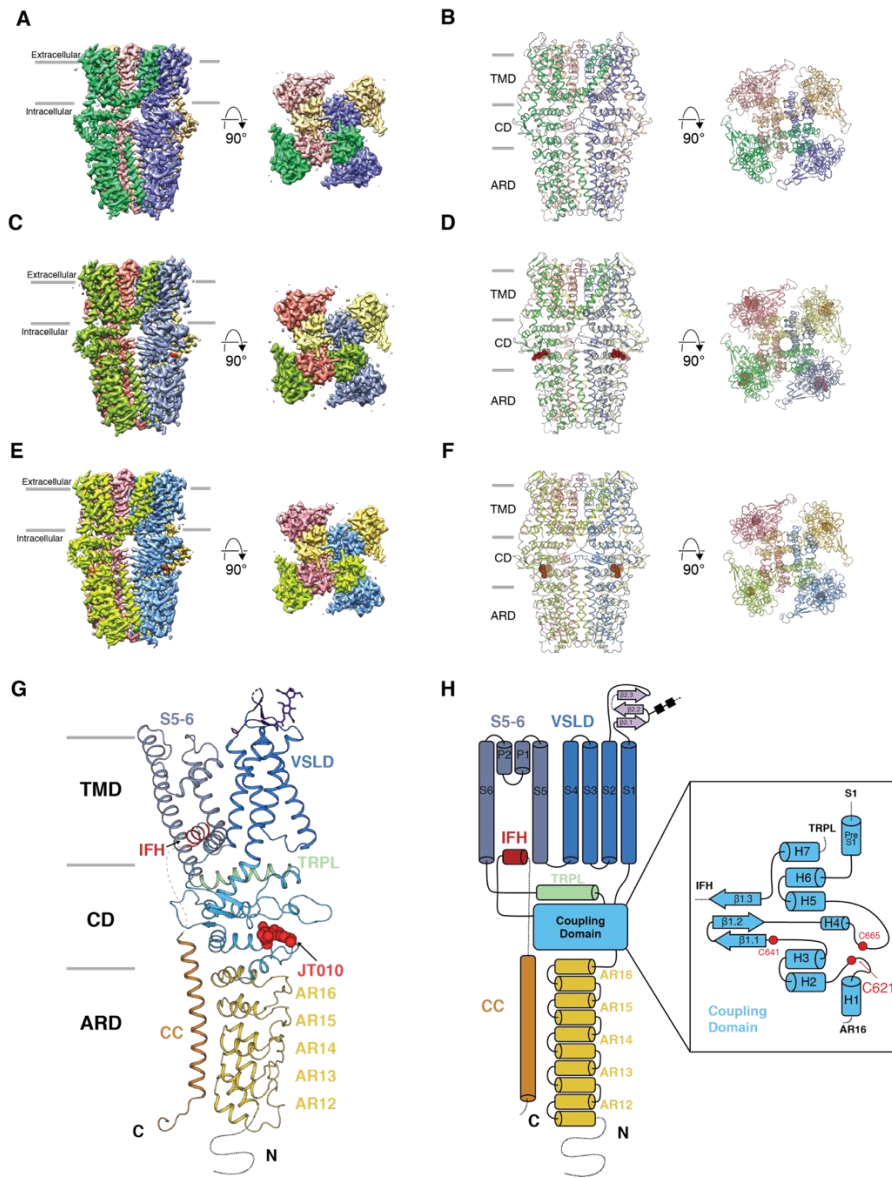


**Figure 7: Overview of hTRPA1 structures.**

(A and B) 3D reconstruction (A) and model (B) of the ligand-free TRPA1<sub>C621S</sub> structure. (C and D) 3D reconstruction (C) and model (D) of the TRPA1<sub>JT010</sub> structure. The JT010 molecule is indicated in red. (E and F) 3D reconstruction (E) and model (F) of the TRPA1<sub>BITC</sub> structure. BITC is indicated in red. The reconstruction and coordinates are colored by chain in panels A to F. (G and H) The structure (left) and topology overview (right) of a single TRPA1 protomer with a close-up of the structural arrangement elements within the Coupling Domain (box).

### 2.2.1 S1-S2 linker structure and pore helices

Our high-resolution 3D reconstructions of hTRPA1 reconstituted in nanodiscs have allowed us to visualize several structural features that were not resolved in the previous structural study. First, our 3D reconstruction allowed us to build the S1-S2 linker region, which has been found to play a role in both ligand- and voltage-dependent gating of TRPA1 [106] and is the binding site of the spider toxin Pro-toxin 1 (ProTx-1) [107]. Surprisingly, this region, which was previously predicted to be an unstructured loop, adopts a three-stranded  $\beta$ -sheet structure. Furthermore, we observe an additional cryo-EM density at the C-terminal of the first  $\beta$  strand, Asn747, which we assigned as two N-acetylglucosamine (GlcNAc) molecules according to the N-linked protein glycosylation pattern of HEK293S GnTI- cells [108] (Figure 8). In our structure, the  $\beta$ 2 and the two sugar moieties appear to act as a single entity to plug the crevice of VSLD. This arrangement is stabilized by interactions between Phe746 from  $\beta$ 2.2 and the surrounding aromatic and hydrophobic amino acids in the extracellular groove of VSLD (Figures 8B and 8C). Consistent with our structure, previous studies have shown that mutations in  $\beta$ 2, and specifically the mutation of Phe746 to alanine, substantially affects voltage-dependence of TRPA1 [106]. Studies have also shown that mutation of Asn747 reduces the channel's sensitivity to various types of agonists [109]. It is also worth noting that the functional role of this unique glycosylated  $\beta$  sheet in hTRPA1 appears to be reminiscent of the interactions between voltage-sensor toxins or small molecules with

voltage sensor domains in voltage-gated cation channels [110, 111]. Second, our high-resolution 3D reconstructions reveal the intricate selectivity filter architecture in TRPA1 (Figures 8D, 8E and 8F). The selectivity filter is composed of backbone carbonyls of residues Leu913 and Gly914 and the side chain of Asp915. The selectivity filter is wider than that of the previously reported TRPA1 structure (9.2-10.6 Å distance between the backbone carbonyls and the aspartate side chains of diagonally opposing subunits) and large enough to accommodate a hydrated Ca<sup>2+</sup> ion. In addition, hTRPA1 contains two pore helices (PH1 and PH2), similar to the pores of TRPML channels [112]. Interestingly, we found that the PH2 of TRPA1 adopts a  $\pi$  helical turn at its N-terminal end, and it appears that the  $\pi$  -helix is maintained by the interactions between the Arg919 on PH2 from one subunit and Asn919 and Ser921 on PH2 from the adjacent subunit (Figure 8D). PH2 also interacts with PH1 (Figure 8D). Because we have not observed any structural changes associated with ligand binding in the selectivity filter of hTRPA1, and because the analogous selectivity filter in TRPML channels does not act as gate [112, 113], we propose that the S6 gate is solely responsible for TRPA1 channel gating.

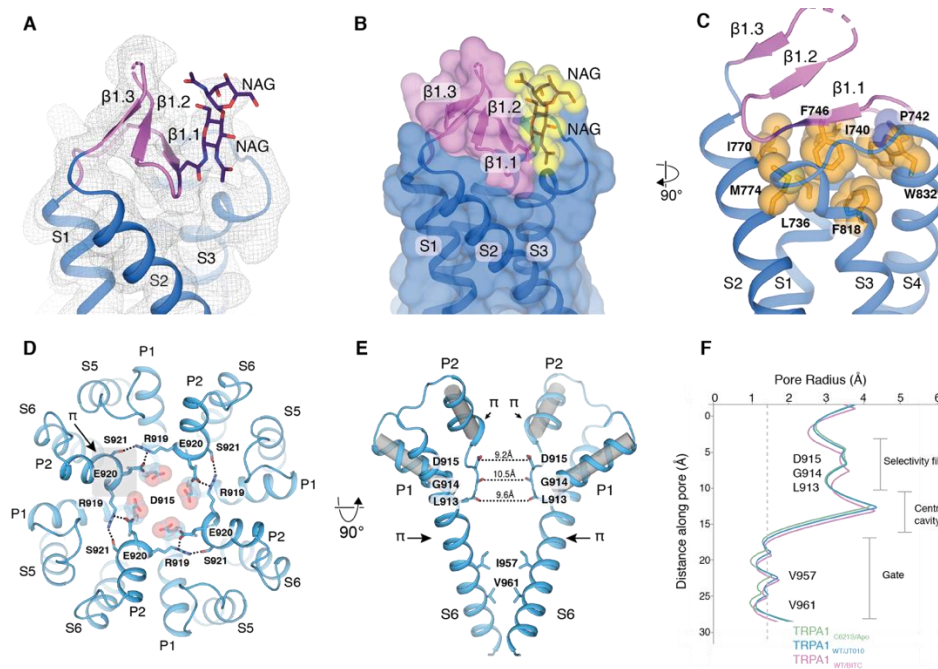


**Figure 8: S1-S2 linker and pore structures of TRPA1.**

(A) Cryo-EM density surrounding the S1-S2 linker in the TRPA1<sub>WT-JT010</sub> 3D reconstruction. The density is shown at 0.024 thresholding. The linker adopts a three-stranded  $\beta$ -sheet conformation. Residue Asn747 is glycosylated. The glycans are shown in stick representation. NAG, N-acetylglucosamine. (B) The three-stranded  $\beta$ -sheet (cartoon and yellow surface representation) and the NAG molecules (magenta surface representation) plug the extracellular crevice of the VSLD domain. (C), Residue F476 from the S1-S2 linker is nestled into the hydrophobic crevice formed by aromatic and hydrophobic residues at the extracellular face of the VSLD helical bundle. Residues involved in interaction are shown in stick and orange sphere representation. (D) Top view of the TRPA1 channel pore, using TRPA1<sub>WT-JT010</sub> as an example. The side chains of the acidic residue Asp915 line the entry to the pore. Interactions are observed between P2 segments of neighboring protomers. Arg919 forms interactions with Glu920 and S921 from the neighboring protomer. All three residues reside in the  $\pi$ -helical turn in P2. Asp915 is shown in stick and sphere representation. Arg919, Glu920, and Ser921 are shown in stick representation. Dashed lines are drawn between residues which are within interaction distance. (E) Side view of the pore of TRPA1<sub>WT-JT010</sub>, the residues that form the selectivity filter and the gate are shown in stick representation. (F) Pore radii calculated by HOLE program for TRPA1<sub>C621S/Apo</sub> (light green), TRPA1<sub>WT/JT010</sub> (light blue) and TRPA1<sub>WT/BITC</sub> (salmon). Dashed line represents the approximate radius of a water molecule (1.4 Å).

### 2.2.2 Lipids and the interfacial helix

In our 3D reconstructions of TRPA1 channel, we identified a novel protein density consistent with a helix at the cytosol-membrane interface located near the side of S1 and S4 of the VSLD (Figure 9). Because of its position, we term this structural motif the interfacial helix (IFH). Cryo-EM maps show that the IFH is part of the C-terminal region which connects the  $\beta_{CD}$  ( $\beta$  1.3) and the coiled coil (CC) (Figures 7, 9A and 9B). The cryo-EM density around this region is well resolved in the TRPA1<sub>WT-BITC</sub> reconstruction and allows unambiguous placement and register assignment of the IFH as well as the linker between  $\beta$ 1.3 and IFH. However, in the ligand-free TRPA1<sub>C621S</sub> and TRPA1<sub>WT-JT010</sub> reconstructions the corresponding cryo-EM density is less defined thus IFH regions in these two models were built as polyalanine chains.

We were also able to resolve and identify several annular phospholipids bound to the TRPA1 channel in our reconstructions. Six to seven phospholipids per subunit (a total of 24-28 per tetramer) are resolved in the 3D reconstructions (numbered lipid 1-7, Figure 9A and 9B). Four phospholipids (lipids 1-4) in the extracellular leaflet of the membrane mostly occupy the interfaces between the grooves of adjacent subunits and between VSLD and pore (Figure 9A). Several lipids are also observed in the space corresponding to the cytoplasmic leaflet of the membrane side. Notably, we observe a phospholipid located in the vicinity of S3, S4, and the S4-S5 linker. In the analogous position phosphatidyl inositol or PI(4,5)P<sub>2</sub> were observed in TRPV1 and TRPV5,

respectively [114, 115]. However, in our TRPA1 structure, the bound lipid in this position is most consistent with a phospholipid. Because PI(4,5)P<sub>2</sub> was not included in the preparation of the nanodisc reconstituted hTRPA1, it remains to be determined whether this site serves as PI(4,5)P<sub>2</sub> site in TRPA1. Interestingly, in the reconstructions of both TRPA1<sub>WT-JT010</sub> and TRPA1<sub>C621S</sub>, we also identified a phospholipid located in the cavity formed by S4, the S4-S5 linker, pre-S1, S1, and IFH (termed interfacial cavity, Figure 9). The bound lipid molecule is most consistent with phosphatidylcholine (PC) where the choline head group of PC is sandwiched between Trp711 of pre-S1 and Glu854 of the S4-S5 linker (Figure 9C). The location of this phospholipid in TRPA1 is reminiscent of the PI(4,5)P<sub>2</sub> binding site recently identified in TRPM8 (Figure 9F) [116]. In TRPM8, PI(4,5)P<sub>2</sub> binding at this site is essential for channel function [117, 118].

Notably, the conformation of the interfacial cavity in the TRPA1<sub>WT-BITC</sub> is different to those observed in the TRPA1<sub>WT-JT010</sub> and TRPA1<sub>C621S</sub> and the density corresponding to this lipid is missing in the TRPA1<sub>WT-BITC</sub> reconstruction (Figures 9D and 9E). To compensate this missing lipid, the IFH in TRPA1<sub>WT-BITC</sub> is positioned closer to the VSLD, resulting in a reduced size of the cavity and thus the elimination the lipid binding (Figure 9E).

Notably, the recently identified gain-of-function mutation Asn855Ser, which causes a familial episodic pain syndrome (FEPS) in humans [26], is located at the junction between S4 and the S4-S5 linker and interacts with IFH in the TRPA1<sub>WT-BITC</sub> structure. Interestingly, a recently published hTRPA1 structure in complex with a non-covalent

agonist GNE551 occupies a pocket near Asn855 [30], demonstrating the potential important function of this region. Furthermore, Cys1021 which is located in the IFH was proposed to be the binding site for zinc, which can potentially activate TRPA1 [119]. Our structures have now revealed that the IFH is a distinct structural motif which forms a part of a dynamic interfacial cavity that can be occupied by lipids and contains the potential binding site for zinc. The dynamic movement of IFH appears to be a determinant for lipid binding in the interfacial cavity as well as for the interactions between the IFH and the Asn855 residue which is a site for a disease-inducing gain-of-function mutation. We therefore propose that the IFH plays an important role in TRPA1 gating by engaging in dynamic interactions with phospholipids and the junction between S4 and the S4-S5 linker. Consistent with this idea, deletion of IFH substantially affects hTRPA1 channel function (Figure 23).

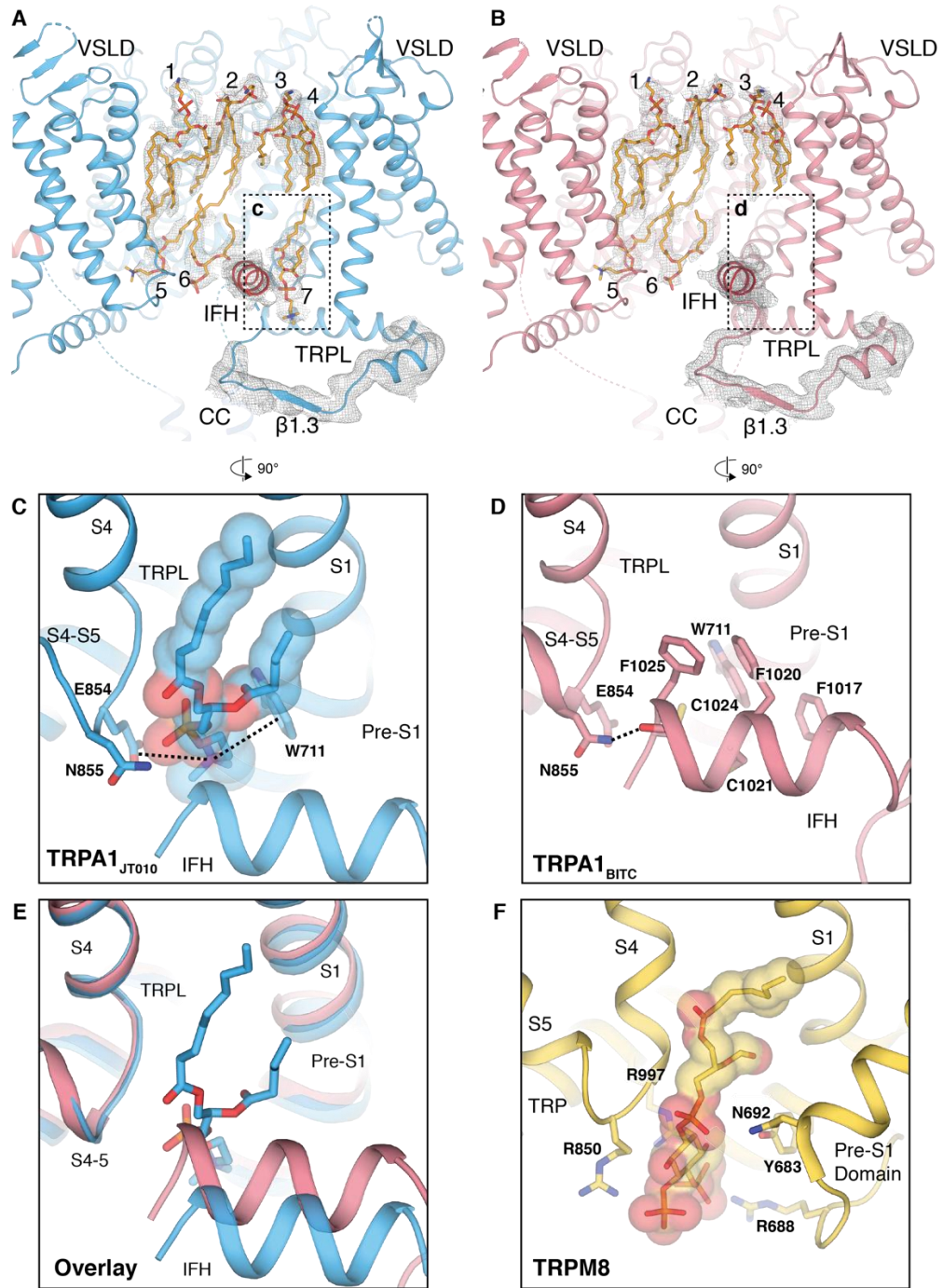


**Figure 9: Lipids in TRPA1.**

Figure captions continue to next page.

(A) Lipids captured in the TRPA1<sub>WT-JT010</sub> structure. In TRPA1<sub>WT-JT010</sub> a phospholipid molecule is observed in the interfacial cavity between the Pre-S1, S4, the S4-S5 linker and the IFH (boxed region). The cryo-EM map is shown at 0.02 thresholding. (B) Lipids captured in the TRPA1<sub>WT-BITC</sub> structure. In the TRPA1<sub>WT-BITC</sub>, the interfacial cavity contains no lipid density (boxed region). The cryo-EM map is shown at 0.018 thresholding. (C) A close-up view of the interfacial cavity in TRPA1<sub>WT-JT010</sub> shows that the phospholipid interacts with residues Trp711 in the Pre-S1 and Glu854 in the loop connecting the S4 to the S4-S5 linker. Residue Asn855, the location of a gain-of-function disease mutation, is also located at this interface. Trp711, Glu854, and Asn855 are shown in stick representation and the phospholipid molecule is shown in stick and sphere representation. (D) A close-up of the interfacial cavity in TRPA1<sub>WT-BITC</sub> shows that the space occupied by phospholipid in TRPA1<sub>WT-JT010</sub> is filled with aromatic residues from IFH and Pre-S1. In this structure, a direct interaction is observed between Asn855 and the backbone carbonyl of Cys1024 in the IFH. Residues Trp711, Glu854, Asn855, Phe1020, Cys1021, Cys1024, and Phe1025 are shown in stick representation. (E) An overlay of the interfacial cavities of TRPA1<sub>WT-JT010</sub> (blue) and TRPA1<sub>WT-BITC</sub> (salmon) shows that the IFH in the TRPA1<sub>WT-BITC</sub> moves closer to the Pre-S1, S4 and the S4-S5 linker, thereby reducing the size of the cavity and making it incompatible with lipid binding. (F) A close-up view of the interfacial cavity in TRPM8 with a PI(4,5)P<sub>2</sub> molecule bound. The presence of a large number of positively charged residues, absent in the interfacial cavity in TRPA1, facilitates coordination of PI(4,5)P<sub>2</sub>. PI(4,5)P<sub>2</sub> is shown in stick and sphere representation and the interacting residues (Arg688, Tyr683, Asn692, Arg850, and Arg997) are shown in stick representation.

## **2.3 The Electrophile-binding Pocket and Structural Basis for High Reactivity of Cys621**

### **2.3.1 JT010 and BITC binding in TRPA1**

When applied to HEK293 cells expressing hTRPA1, JT010 elicits robust inward and outward currents, which desensitize over time (Figure 23A). Based on our dose-response curves, the EC<sub>50</sub> of JT010 is ~7.6 nM (Figure 24B) which is slightly higher than the previously reported value measured by a cell-based calcium uptake assay [44]. To confirm that Cys621 in hTRPA1 is indeed the site for covalent modification by JT010 and other electrophiles, we introduced a Cys621Ser mutant (TRPA1<sub>C621S</sub>) and observed that the HEK293 cells expressing TRPA1<sub>C621S</sub> do not exhibit any currents upon application of 3 μM of JT010 (Figure 23C).

In the 2.88 Å reconstruction of the JT010-TRPA1 complex, we observed a strong EM density located in the CD at the Cys621 residue (Figures 10A and 10C) We assigned this density to JT010 because it matches the size and shape of the JT010 molecule and is absent in the reconstruction of TRPA1<sub>C621S</sub> (Figures 11A and 11D). The cryo-EM density peaks for JT010 and Cys621 are connected, consistent with formation of a covalent bond between JT010 and Cys621 (Figure 11B). The JT010 binding site is reminiscent of a clamshell, with H1, H2 and the H1-H2 loop forming the bottom half, while H4 and the H4-H5 loop forming the top half (Figures 7G and 10A). Residue Cys621 is located at the base of the bottom half of the binding site (Figure 10A). Four aromatic residues (Phe612, His614, Phe669 and Tyr680) from both halves of the pocket

participate in sealing the lateral entries to the binding site and complete the pocket (Figures 10C and 10D). The acetamide group of JT010 is covalently linked to the thiol moiety of Cys621 while its methoxyphenyl thiazol group interacts with above-mentioned aromatic amino acids. Specifically, the thiazol group interacts with Phe612 and Tyr680 through CH- $\pi$  and sulphur- $\pi$  interactions, respectively (Figures 10C and 10D) and the methoxyphenyl group is surrounded by and interacts with His614, Pro666, Phe669 (Figure 10C). To test the role of these observed interactions in JT010-dependent TRPA1 activation, we performed site-directed mutagenesis on the relevant residues and electrophysiological studies, and found that mutations of the aromatic amino acids result in near complete loss of JT010-dependent TRPA1 currents (Figures 23 and 24) without affecting channel expression.

BITC is an isothiocyanate that reacts with cysteine thiols via a reversible thiol-Michael addition reaction. To capture the BITC bound conformation, we incubated the nanodisc-reconstituted wild type TRPA1 with a high concentration of BITC (1 mM) before freezing. The cryo-EM reconstruction of the BITC-TRPA1 complex was resolved to an overall resolution of 3.1 Å and we observed a clear EM density located in the pocket of the CD and connected to Cys621 (Figures 10B and 11C). This density matches the size and shape of an BITC molecule and also absent from the reconstruction of TRPA1<sub>C621S</sub> (Figure 11). We therefore assigned this EM density to BITC. Interestingly, we observed an additional cryo-EM density of a similar shape by Cys665 in the upper half

of the binding site (Figure 11G). Cys665 has previously been implicated in AITC sensing [12], but because the density connected to this residue was not as strong as the one observed near Cys621, we chose not to assign it to BITC. We speculate that the high concentration of BITC might have forced covalent modification of Cys665. Our electrophysiological data shows that the Cys621Ser mutation does not exhibit BITC-dependent TRPA1 currents while the Cys665Ser mutation does, indicating that BITC modification of Cys665 is not necessary for TRPA1 activation (Figures 23G-L and 24S-X). However, it is possible that Cys655 can be covalently modified by BITC without contributing to TRPA1 activation. Indeed, our structure suggests that the binding pocket may accommodate simultaneous binding of two BITC molecules (Figure 11G). The benzyl ring of BITC fits snugly into the groove generated by the loop between  $\beta$ 1.2 and H4, Ile623 on H2, and H1 (Figure 10B, 10E and 10F). Notably, the residues that are important for JT010 binding (Pro666, Phe669, and Tyr680) adopt a similar conformation in the TRPA1<sub>WT-BITC</sub> and TRPA1<sub>WT-JT010</sub>. The turn of the H4-H5 loop appears to differ slightly in the two structures but given that the density is poorly resolved in TRPA1<sub>WT-BITC</sub>, we refrain from drawing conclusions from this observation. Taken together, our structural and functional data show that the electrophile-sensing site in human TRPA1 centers around Cys621 and provide the structural basis for electrophile recognition in TRPA1.

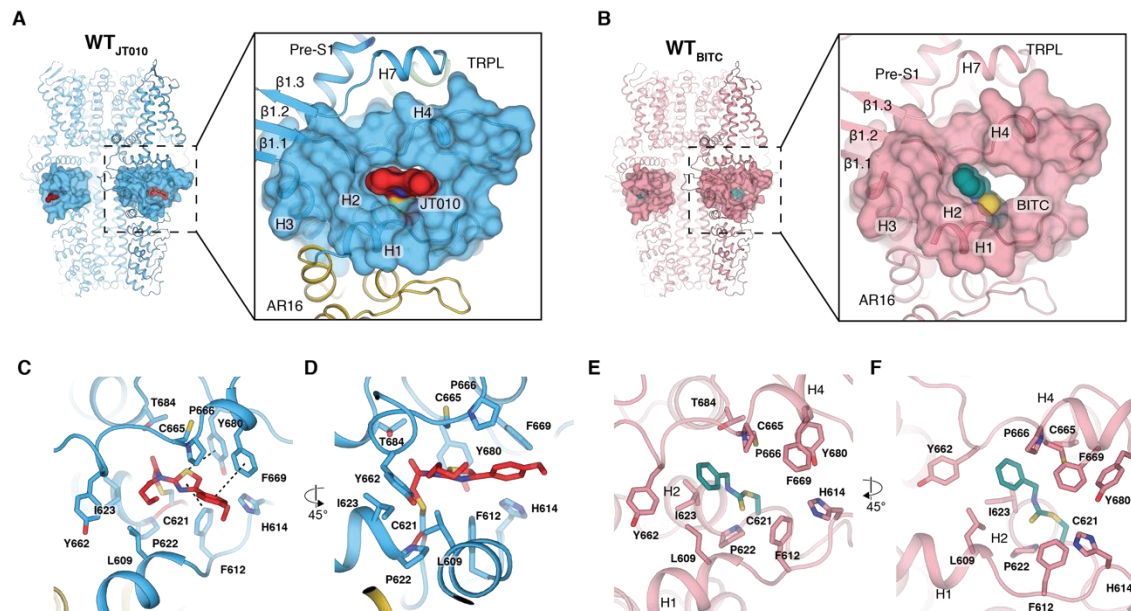


**Figure 10: JT010 and BITC binding in TRPA1.**

(A and B) The electrophile (JT010 (A) and BITC (B)) binding pocket is located in the coupling domain of TRPA1. The binding site is shaped as a clam shell, with H1, H2 and the H1-H2 loop forming the bottom part, and H4, H5 and the H4-H5 loop forming the upper part. The pocket is shown in cartoon and surface representation, and the modeled JT010 (A) and BITC (B) molecules are shown in sphere representation. (C and D) A close-up view of the JT010 binding site. JT010 is covalently bound to the C621 residue via its acetamide group. Its thiazol group forms CH-  $\pi$  and sulphur-  $\pi$  interactions with Phe612 and Try680, respectively. In addition, the methoxyphenyl group interacts with His614, Pro666, and Phe669. Residues Leu609, Phe612, His614, Cys621, Pro622, Ile623, Tyr662, Cys665, Pro666, Phe669, Try680, and Thr684 are shown in stick representation. (E and F) A close-up view of the BITC binding site. BITC is covalently bound to Cys621. Residues Leu609, Phe612, His614, Cys621, Pro622, Ile623, Try662, Cys665, Pro666, Phe669, Try680, and T684 are shown in stick representation.

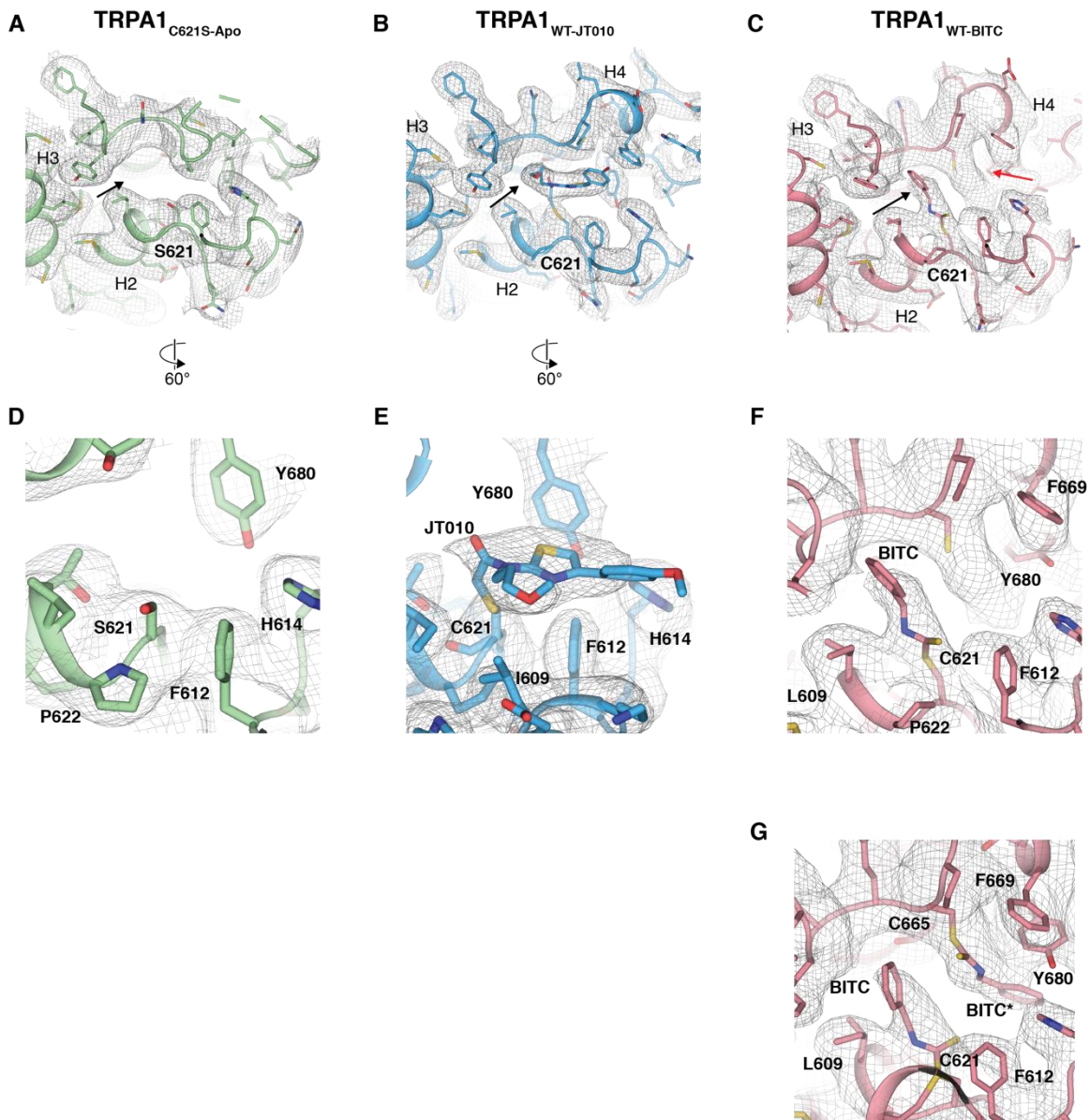


**Figure 11: Density around the ligand binding site in TRPA1<sub>WT-JT010</sub> and TRPA1<sub>WT-BITC</sub>.**

(A-F) The full map contoured around the electrophile binding region in TRPA1<sub>C621S</sub> (A and D), TRPA1<sub>WT-JT010</sub> (B and E) and TRPA1<sub>WT-BITC</sub> (C and F). Map is contoured at 0.02, 0.018 and 0.017 thresholding, respectively. (G) Proposed model for the second BITC density around Cys665 residue. Map is contoured at 0.017 thresholding.

### 2.3.2 Structural basis of high reactivity of Cys621 in TRPA1

Although the first structure of hTRPA1 has been invaluable for our understanding of the channel architecture, the low local resolution around the CD did not allow for unambiguous register assignment [73] which in turn precluded detailed insights into the structural basis for the high reactivity of Cys621 in TRPA1 (Figure 22).

In all ligand-free and ligand-bound structures, the bottom half of the electrophile binding pocket maintains a similar conformation (Figures 13C-D). Cys621 is located near the base of H2 and is separated from the helix by Pro622 which points the N-terminus of H2 toward the thiol group of Cys621 (Figure 12). In this arrangement, the helical dipole (N-cap) exerts electrostatic force on the thiol group of Cys621. Furthermore, directly opposite Cys621 in the H1-H2 loop, Phe612 is positioned facing the Cys621 thiol moiety and engages it in a thiol- $\pi$  interaction (Figure 12). Notably, H1 is oriented perpendicular to H2, and its C-terminus with its helical dipole (C-cap) forms an electrostatic interaction with the quadrupole of Phe612. This apparently stabilizes the Cys621-Phe612 thiol- $\pi$  interaction by fixing the Phe612 side chain in the optimal rotamer conformation for this interaction. We suggest that this unique structural arrangement serves two roles. First, the pKa of Cys621 is lowered synergistically by interaction between the N cap and Cys621 and by the thiol- $\pi$  interaction that exists between Cys621 and Phe612. However, as was previously discussed [120], lowering of the pKa alone is not sufficient to account for the extraordinary reactivity of Cys621. Second, the orientation of aromatic ring of

Phe612 is fixed due to helical dipole of H1 and this rigidified aromatic ring of Phe612 reduces the entropy of the thiol group of Cys612 and thus fixes it in the optimal orientation. The combined effect of these interactions contributes to the high reaction rate of Cys621 in hTRPA1 by enhancing the effective collision of the electrophile-thiol reaction. Finally, one side of the binding pocket in the CD is decorated with aromatic amino acid residues (Phe612, His614, Phe669 and Tyr680) and the other side with two aromatic amino acids (Tyr662 and Trp605). We suggest that the role of these electron-rich aromatic amino acids surrounding Cys621 is to attract electrophiles into this binding pocket and increase their local concentration.

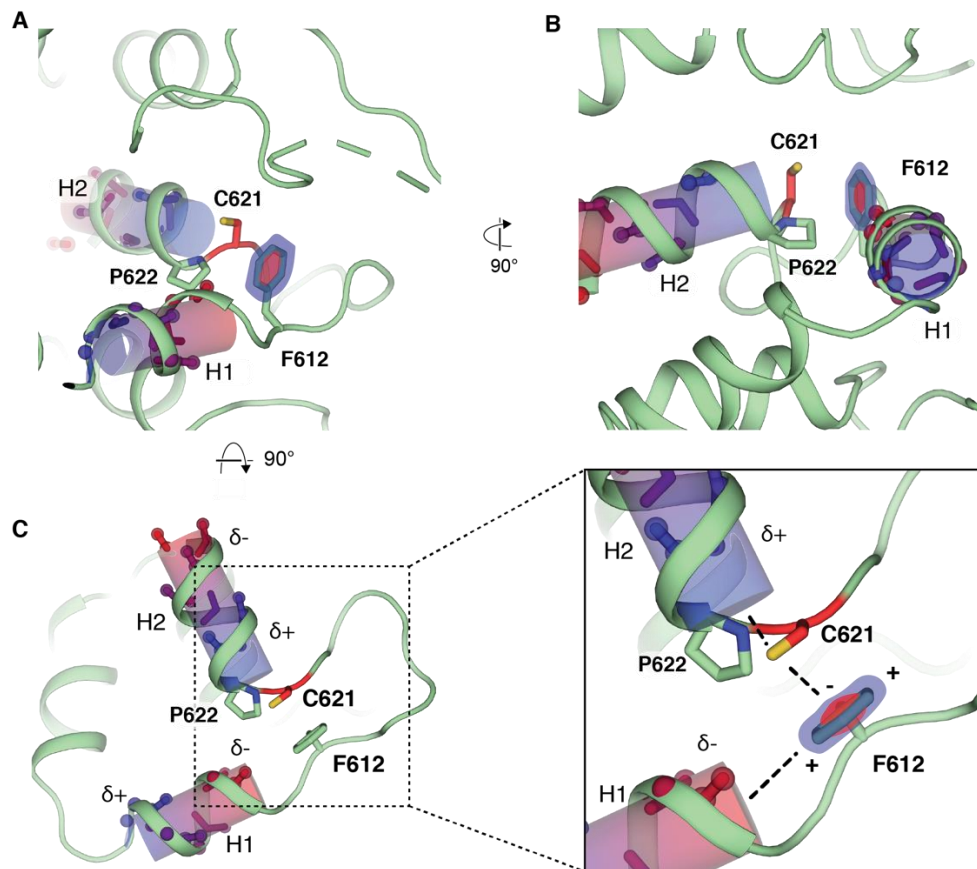


**Figure 12: The architecture of the electrophile binding pocket endows C621 with high reactivity.**

(A and B) The environment in the electrophile binding pocket TRPA1<sub>C621S</sub> Apo. Residue 621 is surrounded by helical dipoles of H1 and H2 helices (shown in cylinder and stick-and-ball representation). (C) The close-up of the interactions between H1, H2, F612 and Cys621. The helical dipole of H2 exerts electrostatic force on the thiol group of Cys621, lowering its pKa. The conformation of the F612 residue is held in place by the helical dipole of H1, which exerts electrostatic force on the positively charged edge of the Phe612 quadrupole. The combination of these interactions results in stabilization of the Cys621-Phe612 thiol- $\pi$  interaction, which in turn reduces the entropy of the Cys621 side chain. The lowering of the pKa by the helical dipole of H2 and the stabilization of the thiol- $\pi$  interaction by the helical dipole of H1 contributes to the high reactivity of Cys621. The high reactivity is also aided by the electron-attracting aromatic residues in the pocket. (D) The close-up interactions showing that the residue Lys620 forms salt bridge interactions with Glu625 and Glu628 located within the H2 and appears to maintain the structural integrity of the electrophile binding site.

## **2.4 Conformational Changes Upon Ligand Binding**

In all TRPA1 structures, the Ile957 and Val961 in S6 form the gate (Figure 8E). Despite being bound to ligand, both the TRPA1<sub>WT-JT010</sub> and TRPA1<sub>WT-BITC</sub> structures apparently adopt non-conducting states (Figure 8F), suggesting that our cryo-EM reconstructions have captured conformations that either precede or follow the open state. Because covalent agonist-dependent TRPA1 activation is followed by desensitization (Figure 23A), our sample might contain multiple different conformational states. It is also possible, as is often observed in cryo-EM structures of ion channels [73, 116, 121, 122], that we have captured energetically favored conformational states of the channel.

Despite the fact that the ligand-bound structures adopt non-conducting states, we observe substantial conformational changes that are associated with binding of electrophile agonists. As discussed earlier, the bottom half of the CD binding pocket remains unchanged in all of our TRPA1 structures. However, the top half of this pocket appears to experience a large degree of plasticity and undergoes ligand-dependent conformational changes. In the ligand-free TRPA1<sub>C621S</sub> the top half of the pocket adopts a conformation that allows Pro666 to interact with Tyr680 through CH- $\pi$  interactions (Figure 13A). Upon binding of JT010, the thiazole group of JT010 displaces Pro666 and interacts with Tyr680, resulting in a large rotation of the H4-H5 loop containing Cys665 and Pro666 (Figure 13C-E). This JT010-dependent conformational change in the binding

pocket is propagated laterally to the  $\beta_{CD}$  which swings outwards and in turn causes a change in the position of the IFH (Figure 13G-H). The conformational change is also propagated vertically to result in a  $\sim 3^\circ$  counterclockwise rotation of ARD and CD when viewed from the extracellular side (Figure 13B). Interestingly, binding of BITC leads to similar global conformational changes in the CD and the ARD (Figure 13F-H). Importantly, BITC elicits a rotation of Cys665 and Pro666 as well as an outward swing motion of  $\beta_{CD}$  similar to that observed in the JT010-bound structure (Figure 11 and 13F-H). Importantly, our mutagenesis studies show that the mutation Tyr680Ala in the H4-H5 loop has significant impact on channel activation. The comparison of these structures and the mutational studies have led us to speculate that the local conformational changes in the top half of the binding pocket would be similar regardless of the type of covalent agonist used to activate the channel. This, in combination with the apparent plasticity of the top half of the binding pocket, might explain why TRPA1 can be activated by so many structurally and chemically diverse covalent agonists. Based on this idea, we hypothesize that the Cys665 and Pro666 are not the main targets of covalent modification but instead act as a conformational switch that senses covalent modification of Cys621. Consistent with our hypothesis, we found that introduction of the isosteric Cys665Ser mutation results in functional channels that can be activated by either JT010 or BITC while introduction of larger sidechain (Cys665Leu) results in a channels with no JT010-dependent activity [120] (Figure 24C and 24D)

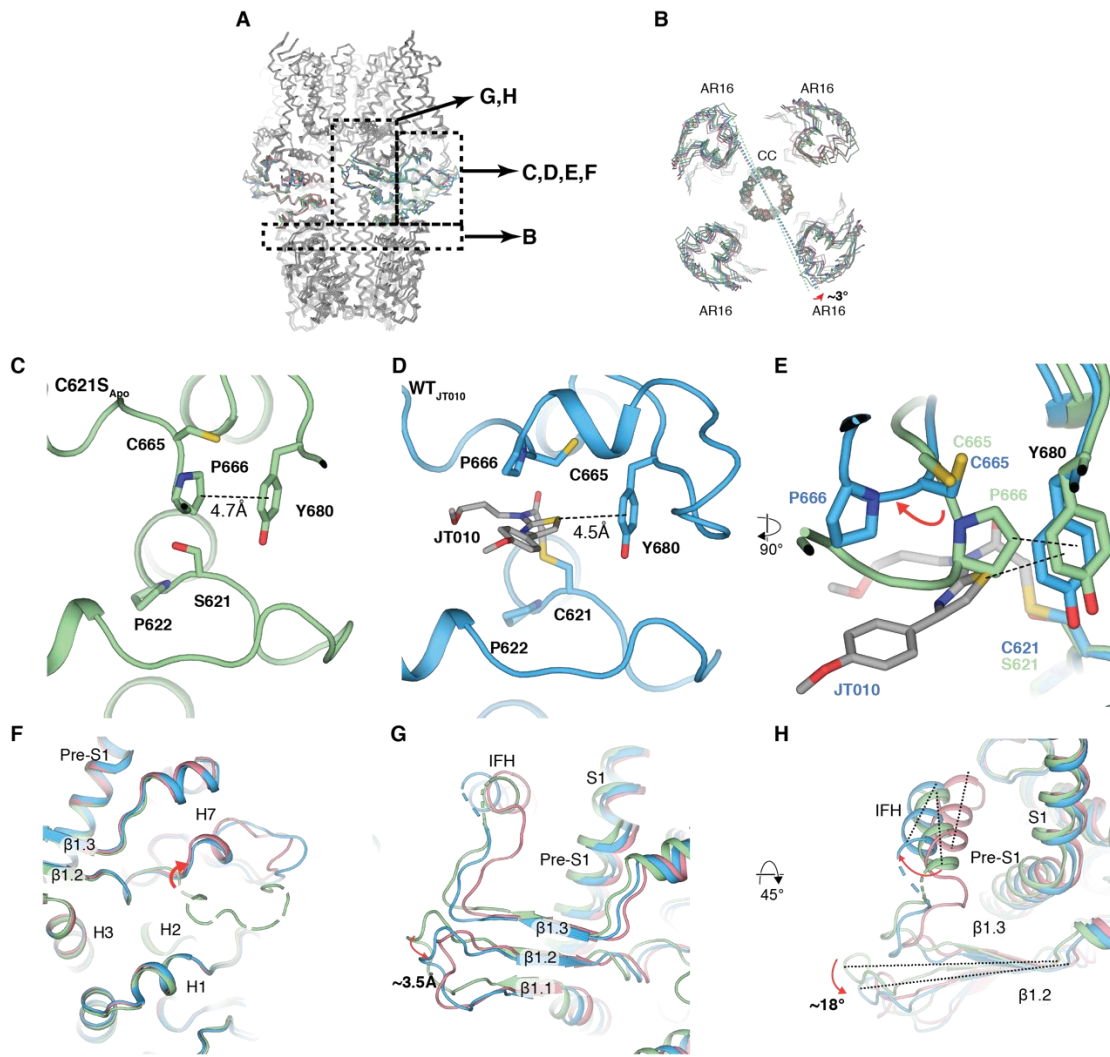


**Figure 13: Conformational changes in the electrophile binding pocket and the CD upon JT010 and BITC binding.**

Figure captions continue to next page.

(A) Orthogonal view of the channels TRPA1<sub>C621S</sub> (light green), TRPA1<sub>WT-JT010</sub> (light blue) and TRPA1<sub>WT-BITC</sub> (salmon) overlaid via their TMDs. The boxes indicate the views shown in panels (B-H). (B) The ARDs of the ligand-bound structures also undergo a counter-clockwise rotation. Rotation angles are measured between C $\alpha$  atoms in His570. In all panels TRPA1<sub>C621S</sub> is shown in green, TRPA1<sub>WT-JT010</sub> in blue and TRPA1<sub>WT-BITC</sub> in salmon. (C) In the ligand-free TRPA1<sub>C621S</sub> structure, Pro666 and Tyr680 engage in a CH- $\pi$  interaction. (D) Upon binding of JT010, the thiazole moiety of the molecule displaces P666 and engages in interactions with Tyr680. This causes a large conformational change in the loop containing Cys665 and Pro666. The JT010 molecule is shown in stick representation. (E) Overlay of the electrophile binding pockets in TRPA1<sub>C621S</sub> (green) and TRPA1<sub>WT-JT010</sub> (blue). The conformational change in the loop containing Cys665 and Pro666 is indicated with a red arrow. The JT010 molecule is shown in stick representation. (F) To observe the local conformational changes in the CD upon ligand binding, the CDs of TRPA1<sub>C621S</sub> (green), TRPA1<sub>WT-JT010</sub> (blue) and TRPA1<sub>WT-BITC</sub> (salmon) are aligned. The alignment shows that only the upper half of the binding site undergoes a conformational change. (G) Relative to the TMD, the CD undergoes a  $\sim 3.5$  Å outward swing upon ligand binding. TRPA1<sub>C621S</sub> is shown in green, TRPA1<sub>WT-JT010</sub> in blue and TRPA1<sub>WT-BITC</sub> in salmon. (H) The  $\beta$ -sheet of the CD undergoes a counter-clockwise rotation when viewed from the extracellular space. The IFH is also displaced during ligand binding. In the TRPA1<sub>WT-JT010</sub> (blue) structure, the IFH moves away from the Pre-S1. In the TRPA1<sub>WT-BITC</sub> (salmon) structure the IFH moves closer to the Pre-S1.

## **2.5 Discussion**

Our structural and functional analyses revealed that TRPA1 adopts a distinct design principle and its mechanisms of ligand sensing in stark contrast to the menthol sensor TRPM8 [116] and the capsaicin sensor TRPV1 [114, 123, 124]. First, unlike TRPV1 and TRPM8, the electrophile sensing site is located at the cytoplasmic side. The highly-orchestrated design of helical dipoles as well as  $\pi$  interactions within the CD confers onto Cys621 not only high reactivity but also the ability to react with various types of electrophiles. Furthermore, the ability of TRPA1 to react with various types of electrophiles could be explained by the unique design of the “clam shell” binding pocket where the bottom half contains the highly reactive C621 that is modified by electrophiles and the top half acts as a conformational switch (Figure 14). To the best of our knowledge, this design is unique and different from active sites in highly substrate-specific enzymes that utilize reactive cysteines. Interestingly, this configuration of the binding pocket also appears to be important for the binding of the cell-penetrating scorpion toxin WaTx. WaTx activates the human TRPA1 but not the rat snake ortholog, which carries an alanine but not a proline in position 622 (Ala627 in rat snake TRPA1). An alanine-to-proline substitution at this position confers WaTx-sensitivity to the rat snake TRPA1 [125].

Second, the conformational step that is required for TRPA1 activation is different from TRPV1 and TRPM8. The binding of covalent agonists to the CD leads to a

conformational change in  $\beta_{CD}$ , which in turn repositions the IFH to interact with the S4-S5 linker to open the S6 gate. This is in stark contrast to TRPV1 and TRPM8 where ligand binding to the S4-S5 linker or VSLD cavity and the TRP domain, respectively, leads to opening of the S6 gate [117, 126]. Furthermore, it is important to note that the TRPL domain in TRPA1 does not appear to fulfil the same function as the TRP domain in TRPV or TRPM channels. TRPL is located in the cytosol, unlike the TRP domain which is positioned at membrane-cytosol interface. In addition, unlike the TRP domain the TRPL does not engage in extensive interaction networks with the TMD. We therefore speculate that the role of TRPL in the gating of TRPA1 might not be as essential as that of the TRP domain in TRPV and TRPM channels. Third, the role of lipids in TRPA1 gating appears to be different to the mechanisms identified in TRPV1 and TRPM8. Even though we observe a phospholipid in the interfacial cavity, a site that is analogous to the PI(4,5)P<sub>2</sub> site in TRPM8, the cavity is electrostatically incompatible with PI(4,5)P<sub>2</sub>. Importantly, our data suggest that the phospholipid might be a negative regulator of TRPA1 as it blocks the interaction between the S4-S5 linker and the IFH. We therefore speculate that the dynamic interactions between IFH and the phospholipid in the interfacial cavity are critical for TRPA1 gating.

After our study described in this chapter was published [127], Zhao et al. [30] reported several TRPA1 structures, including a structure where the channel adopting an open conformation. By comparing structures of different conformations, the authors

were able to propose a two-step model for electrophile-dependent activation. The binding of electrophiles would trigger a conformational rearrangement in the A-loop (which we term “upper clamshell loop”), located above the binding pocket. This rearrangement is subsequently propagated to the TRP-like domain, and finally S6, to open the channel gate. Moreover, a calcium binding site located between S2 and S3 was identified and characterized. This site was conserved in TRPM2, 4 and 8 [117, 128, 129], and is believed to be the major calcium regulation site in TRPA1. The authors’ conclusion regarding the mechanism of electrophile binding and activation largely coincides with ours.

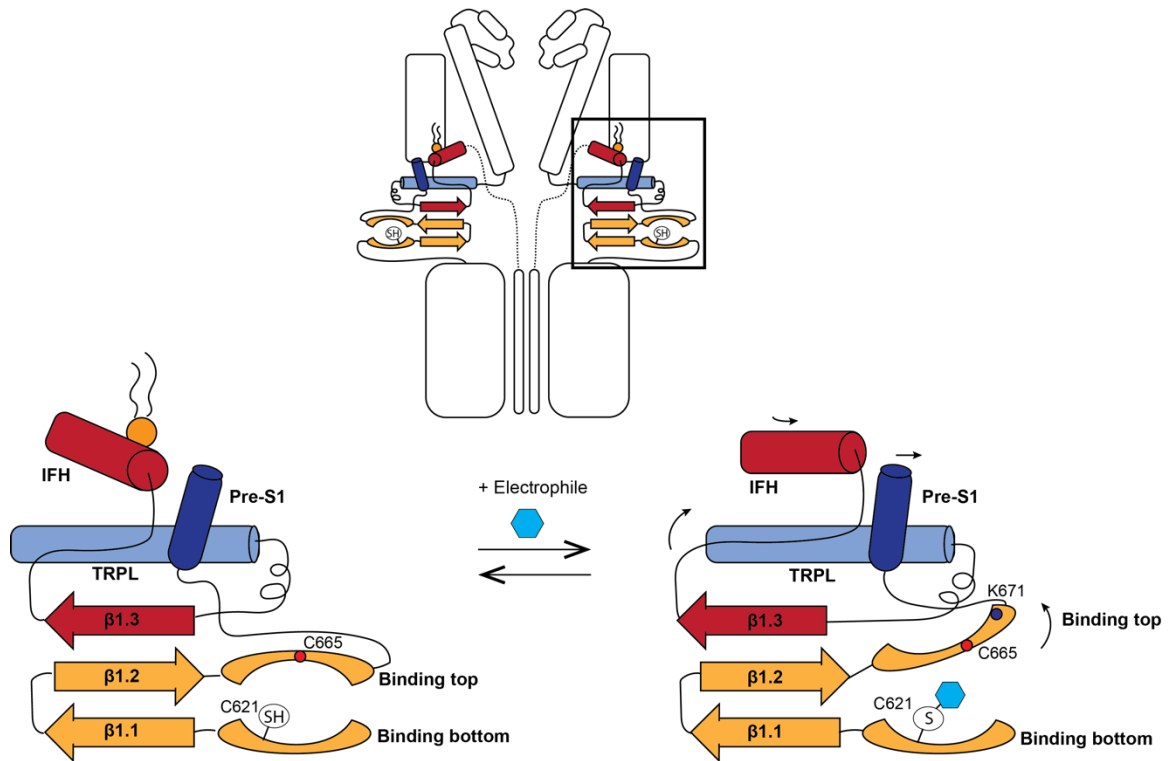


**Figure 14: Proposed electrophile sensing mechanism for TRPA1.**

The electrophile binding site adopts a clam shell conformation. The loop which forms the top part of the binding site flips when an electrophile covalently modifies Cys621, triggering a swing of the  $\beta$ -sheet ( $\beta$ 1.1-  $\beta$ 1.3) and a change in the position of the IFH.

## 2.6 Materials and Methods

### 2.6.1 Expression and purification of human TRPA1

The *Homo sapiens* full-length human TRPA1 was synthesized (BioBasic) and cloned into BacMam vector, in-frame with a FLAG-tag followed by 10 $\times$  His-tag in C-terminus. The wild type human TRPA1 (hTRPA1) was used to obtain the JT010- and

BITC-bound structures. To obtain the ligand-free state, the C621S mutation was introduced using the QuickChange site-directed mutagenesis kit (Agilent). Baculovirus was generated according to manufacturer's protocol (Bac-to-Bac, Invitrogen). For TRPA1 protein expression, HEK293S GnTI<sup>-</sup> cells (ATCC) was cultured in Freestyle 293 media (Life Technologies) supplemented with 2% (v/v) FBS (Gibco) at 8% CO<sub>2</sub>. Cells were infected with 8% (v/v) P3 baculovirus at 3×10<sup>6</sup> ml<sup>-1</sup> density. After 20 hours shaking incubation at 37°C in the presence of 8% CO<sub>2</sub>, 10 mM sodium butyrate (Sigma-Aldrich) was added to cell culture and the incubation temperature was lowered to 30°C to boost protein expression. The cells were harvested after an additional 40-44 hours by centrifugation at 550× g, and were subsequently resuspended in lysis buffer (20 mM Tris pH8, 150 mM NaCl, 12 µg mL<sup>-1</sup> leupeptin, 12 µg mL<sup>-1</sup> pepstatin, 12 µg mL<sup>-1</sup> aprotinin, DNase I, 1 mM phenylmethylsulphonyl fluoride, 1 mM inositol hexaphosphate (InsP<sub>6</sub>), 5 mM TCEP-HCl and 1% (w/v) digitonin). Protein extraction was performed at 4°C for 1 hour, followed by centrifugation at 13000× g for 30 min to remove insoluble material. The supernatant was subsequently incubated with anti-FLAG M2 resin (Sigma-Aldrich) at 4°C for 1 hour. The resin was then packed onto a gravity-flow column (BioRad), followed by washing with 10 column volumes of wash buffer (20 mM Tris pH 8, 150 mM NaCl, 0.07% digitonin, 1 mM InsP<sub>6</sub>, 1 mM TCEP). The TRPA1 protein was then eluted with 5 column volumes of elution buffer (20 mM Tris pH 8, 150 mM NaCl, 0.07% digitonin, 3 mM TCEP, 1 mM InsP<sub>6</sub>, 100 µg mL<sup>-1</sup> FLAG peptide). The eluted protein was

concentrated and further purified on a Superose 6 size-exclusion column equilibrated with GF buffer (20 mM Tris pH 8, 150 mM NaCl, 0.07% digitonin, 3 mM TCEP, 1 mM InsP<sub>6</sub>). The peak fraction was collected and subjected to nanodiscs reconstitution.

### **2.6.2 Nanodiscs Reconstitution**

MSP2N2 was purified according to previously published protocol [130]. Detergent-solubilized TRPA1 was concentrated to 1-1.5 mg mL<sup>-1</sup>, and mixed with purified MSP2N2 and extruded lipid mix (1-palmitoyl-2-oleoyl-sn-glycero-3-phosphocholine (POPC), 1-palmitoyl-2-oleoyl-sn-glycero-3-phosphoethanolamine (POPE), 1- palmitoyl-2-oleoyl-sn-glycero-3-phospho-(1'-rac-glycerol) (POPG), POPC:POPE:POPG=3:1:1) at 1:3:200 molar ratio. The mixture was incubated in 4°C for 30 min with constant rocking. 100 mg mL<sup>-1</sup> Bio-Beads SM2 (Bio-Rad) was then added to the mixture to initialize the reconstitution reaction. The Bio-Beads were exchanged after two hours (100 mg mL<sup>-1</sup>), and the mixture incubated with constant rocking in 4°C for 12-15 hours. The mixture was then subjected to size exclusion chromatography on a Superose 6 column pre-equilibrated with buffer DF (20 mM Tris pH 8, 150 mM NaCl, 3 mM TCEP, 1 mM InsP<sub>6</sub>).

### **2.6.3 Cryo-EM Sample Preparation and Data Collection**

The peak fractions from the final size exclusion chromatography containing nanodisc-reconstituted TRPA1 were concentrated to ~0.5mg/ml. For TRPA1<sub>WT-JT010</sub>, the protein was incubated with 100uM JT010 (Sigma-Aldrich) for 30 minutes before

freezing. For TRPA1<sub>WT-BITC</sub>, 1 mM BITC (Sigma-Aldrich) was added to the protein sample 100 minutes before freezing. The TRPA1<sub>WT-JT010</sub> and TRPA1<sub>C621S-Apo</sub> samples were plunge frozen using Leica EM GP Automatic Plunge Freezer operated at 24°C and ~95% humidity. A sample volume of 3µl was applied to a freshly glow-discharged UltrAuFoil R1.2/1.3 300mesh (Quantifoil), blotted with Whatman No. 1 filter paper for 3 seconds followed by plunge-freezing in liquid-ethane cooled by liquid nitrogen. The TRPA1<sub>WT-BITC</sub> sample was plunge frozen using Vitrobot Mk IV (FEI) Plunge Freezer operated at 24°C and ~100% humidity. As before, a sample volume of 3 µl sample was applied to a freshly glow-discharged UltrAuFoil R1.2/1.3 300mesh (Quantifoil), blotted with Whatman No. 1 filter paper for 2 seconds followed by plunge-freezing in liquid-ethane cooled by liquid nitrogen.

TRPA1<sub>WT-JT010</sub> dataset was collected using a Titan Krios (Thermo Fisher) transmission electron microscope operating at 300 kV equipped with a Falcon III detector in counting mode, using the EPU automated data acquisition program. 2313 movies were collected at a nominal magnification of 75,000× with a pixel size of 1.08 Å/pix at specimen level. Each movie contains 30 frames over 60.0 s exposure time, using a dose rate of 0.8 e<sup>-</sup>/px/s, resulting a total accumulated dose of ~42e<sup>-</sup>/Å<sup>2</sup>. The nominal defocus range was set from -1.25 to -3 µm. TRPA1<sub>C621S-Apo</sub> and TRPA1<sub>WT-BITC</sub> datasets were collected using a Titan Krios operating at 300kV equipped with a K3 (Gatan) detector operated in counting mode, using Latitude automated data acquisition program. 3,544

movies for the TRPA1<sub>C621S-Apo</sub> dataset and 4,418 movies for the TRPA1<sub>WT BITC</sub> dataset were collected at a nominal magnification of 22,500 $\times$  with a pixel size of 1.07  $\text{\AA}/\text{px}$  at specimen level. Each movie contains 60 frames over 4.6 s exposure time, using a dose rate of 15e<sup>-</sup>/px/s, resulting a total accumulated dose of  $\sim 60 \text{ e}^-/\text{\AA}^2$ . The defocus range was set from -0.75 to -2.5  $\mu\text{m}$ .

#### 2.6.4 Cryo-EM Data Processing

*For TRPA1<sub>WT-JT010</sub> dataset,* Beam-induced motion correction and dose-weighting was performed using MotionCor2 [88], followed by CTF estimation using Gctf [131]. Micrographs were subsequently selected based on CTF fit quality, yielding 2,031 good quality micrographs. 1,035 particles were manually picked and subjected to a reference-free 2D classification (k=8, T=2), from which the best six classes were selected as reference for automated particle picking in RELION 3.0 [83]. A total of 752,104 particles were picked from 2,031 micrographs and extracted (4x4 Fourier binned, 4.32  $\text{\AA}/\text{pix}$  pixel size and 64 pix box size). Reference free 2D classification (k=50, T=2) was performed in RELION resulting in 21 classes (571,201 particles) which showed clear secondary structure features of TRPA1. These particles were subsequently subjected to 3D auto-refine in RELION, using previously published TRPA1 map (EMD-6267, low-passed filtered to 30  $\text{\AA}$ ) as reference, without masking. Refined particles were re-extracted, re-centered and un-binned (1.08  $\text{\AA}/\text{pix}$ ) and subjected to another round of 3D refinement, using the result of the previous 3D refinement as a reference. A 3D classification without image alignment

was then performed using the output from the un-binned 3D refinement (k=6, T=8), with a soft solvent mask covering the best resolved region of the channel (AR12 to CC). One class, containing 137,605 particles and displaying the most high-resolution features of the channel was isolated and subjected to 3D refinement, producing a 3.06 Å map. The particles from this refinement were then subjected to another round of 2D classification (k=15, T=2), and the best 8 classes were utilized as a template for automated particle picking, resulting in 380,605 particles. 2D classification, 3D refinement and 3D classification were repeated for this set of particles. One class from this new round of 3D classification, which displayed the most high-resolution features, was subjected to 3D refinement yielding a 3.04 Å map. CTF refinement and Bayesian polishing were subsequently carried out on this set of particles using RELION, which yielded a final map with 2.88 Å resolution. Local resolution was calculated using RELION 3.0[83].

*For TRPA1<sub>WT-BITC</sub> dataset*, Beam-induced motion correction and dose-weighting was performed using MotionCor2 [88], followed by CTF estimation using Gctf [131]. Good micrographs were selected based on quality of CTF fit, resulting in 2,186 good micrographs. 1,435 particles were manually selected and used in a reference-free 2D classification (k=8, T=2). From this classification, the six classes showing the best-defined TRPA1 features were selected as template for automated reference-based particle picking in RELION. A total of 396,597 particles were extracted (4x4 Fourier binned, 4.28 Å/pixel size and 64 pixel box size). Reference free 2D classification (k=50, T=2) was performed

in RELION and 8 classes containing a total of 283,493 particles which showed clear, crisp TRPA1 features were selected. These particles were then subjected to 3D auto-refinement without masking in RELION, using the 3D reconstruction of TRPA1<sub>WT-JT010</sub> low-pass filtered to 30 Å as reference map. Refined particles were re-extracted, re-centered and unbinned (1.07 Å/pix, 256 pix box size) and subjected to another round of 3D refinement, using the map generated from previous 3D refinement as a reference. Particles and the refined coordinates from the 3D refinement were then subjected to a no-alignment 3D classification (k=4, T=8), using a soft solvent mask covering the best resolved region of the channel (AR12 to CC). One class, containing 74,677 particles and displaying the most high-resolution features of the channel, was selected and subjected to 3D refinement, producing a 3.37 Å map. CTF refinement (with per-micrograph astigmatism estimation and beam tilt fitting) and Bayesian polishing (using first 40 frames only) was subsequently carried out using RELION, which yielded a final map with 3.06 Å resolution. Local resolution was calculated using RELION 3.0 [83].

*For TRPA1<sub>C621S-Apo</sub> dataset,* Beam-induced motion correction and dose-weighting was performed using MotionCor2 [88], followed by CTF estimation using Gctf [131]. 2,856 micrographs were selected for further data processing based on CTF fit quality. 1,362 particles were manually picked and subjected to a reference-free 2D classification (k=10, T=2), from which the best six classes, showing highly defined TRPA1 features were selected as template for automated reference-based particle picking in RELION. A total of

1,150,312 particles were boxed and then extracted (4x4 Fourier binned, 4.28 Å/pix pixel size and 64 pix box size). Reference free 2D classification (k=50, T=2) was performed in RELION and 14 classes containing 639,334 particles which showed well-defined TRPA1 features were selected. A 3D auto-refinement without masking was then performed with the selected particles, using the TRPA1<sub>WT-JT010</sub> map low-pass filtered to 30 Å as reference map. The refined particles were re-extracted, re-centered and un-binned (1.07 Å/pix, 256pix box size) and subjected to another round of 3D refinement, using the map generated from the previous 3D refinement. Particles and refined coordinates from this 3D refinement were then subjected to a no-alignment 3D classification (k=4, T=8), using a soft solvent mask covering the best resolved region of the channel (AR12 to CC). One best class, containing 119,697 particles, displayed the best-defined features of TRPA1 and was selected and subjected to 3D refinement, producing a 3.13 Å map. Two iterative rounds of CTF refinement (with per-micrograph astigmatism estimation and beam tilt fitting) and Bayesian polishing was subsequently carried out using RELION, which yielded a final map with 2.81 Å resolution. Local resolution was calculated using RELION 3.0 [83].

### **2.6.5 Model Building and Refinement**

The previously published TRPA1 structure (PDB 3J9P) [73] was used as a reference for building TRPA1<sub>WT-JT010</sub> and the coupling domain, the interfacial helix (IFH), the S1-S2 linker, and P2 were built *de novo*. During model building the register assignment was guided by the presence of large aromatic side chains. The structure was

refined manually with ideal secondary structure geometry restraints in Coot [132] and using the *phenix-real\_space\_refine* function with global minimization and secondary structure restraints as implemented in the Phenix suite [133]. The models for the TRPA1<sub>WT-BITC</sub> and TRPA1<sub>C621S-Apo</sub> were built using the TRPA1<sub>WT-JT010</sub> coordinates as a reference. The placement of individual structural elements was performed by rigid body fitting, and the structures were refined in Coot, with ideal secondary structure geometry imposed, as well as using *phenix-real\_space\_refine* with global minimization and secondary structure restraints in Phenix. The restraints for lipids, sugars and ligands, including POPC, POPE, POPG, N-acetylglucosamine, JT010 and BITC, were calculated in Elbow (as implemented in Phenix [133]) from canonical SMILES strings and optimized using the REEL QM2 method (as implemented in the Phenix suite [133]). These were then inspected manually to ensure correct stereochemistry before being fitted into the experimental densities in Coot. The MolProbity server (<http://molprobity.biochem.duke.edu>, [134]) was utilized to identify errors and problematic regions in the models, which were then corrected manually in Coot. The Fourier shell correlation of the half- and full-maps against the model, calculated in Phenix, were in good agreement, indicating that the models were not over-refined. The model of TRPA1<sub>WT-JT010</sub> contains residues 446-1079 with ARD1-11, C-terminus and three loops missing (residues 1-445, 754-760, 1013-1014, 1026-1038, 1079-1119 missing); TRPA1<sub>WT-BITC</sub> contains residues 446-1079 with ARD1-11, C-terminus and two loops missing (residues

1-445, 754-760, 1027-1038, 1079-1119 missing); TRPA1<sub>C621S-Apo</sub> contains residues 446-1079 with ARD1-11, C-terminus and four loops missing (residues 1-445, 754-760, 669-676, 1013-1014, 1026-1038, 1079-1119 missing). Structural analysis and illustrations were performed using Pymol and UCSF Chimera [135].

### **2.6.6 Patch-clamp Electrophysiology in HEK-293 cells**

Patch-clamp electrophysiology experiments were carried out by Dr. Zilong Wang.

HEK-293 cells were obtained from Duke Cell Culture Facility and maintained in DMEM containing 10% fetal bovine serum (FBS, Sigma), 1% penicillin and streptomycin (Gibco) and supplemented with 5% CO<sub>2</sub> at 37 °C. Cells grown in a 6-well plate reaching 40-60% confluency were transiently transfected using Lipofectamine 2000 (Invitrogen). Generally, 2.5 µg of TRPA1 or TRPA1 mutant's DNA and 1 µg of pEGFP DNA were used for each well. At 24 h after the transfections, the cells were digested with 0.05% trypsin and plated on poly-L-lysine coated glass coverslips.

Whole-cell patch clamp recordings were performed at room temperature using an Axopatch-200B amplifier with a Digidata 1440A, acquired with Clampex 10.6, and analyzed with Clampfit 10.6 (Axon Instruments, Union City, CA). The patch pipettes were pulled from borosilicate capillaries (World Precision Instruments) using a P-97 Flaming/Brown micropipette puller (Sutter Instrument). Pipettes with the resistance of 4-6 MΩ were used for the whole-cell recordings. Whole cell recordings were performed

in an extracellular solution that contained (in mM): 140 NaCl, 5 KCl, 2 MgCl<sub>2</sub>, 10 HEPES, and 10 glucose, adjusted to pH 7.4 with NaOH and osmolality to 300-310 mOsm. The internal solution contained (in mM): 140 CsCl, 10 EGTA, 10 HEPES, and 2 Mg-ATP, adjusted to pH 7.3 with CsOH. TRPA1-expressing HEK293 cells were identified by co-expressed GFP. The cell was held at -70 mV, and the membrane potential was ramped from -120 mV to 120 mV over 200 ms, as previously reported (Macpherson et al., 2007a). The interval of each sweep is 10 s. The TRPA1 agonists were perfused for 1 min following a 2 min baseline recording. The whole cell current densities (pA/pF) after drug perfusion at  $\pm$  120 mV were baseline subtracted and used for generating the statistics shown in the figures.

### **3. Structural Basis of Heat Sensing by the Rattlesnake TRPA1 Channel**

#### ***3.1 Biochemical Optimization of Rattlesnake TRPA1 for Cryo-EM Studies***

Compared to human TRPA1 (hTRPA1), rattlesnake TRPA1 (rsTRPA1) was biochemically unstable as demonstrated by FSEC and negative stain EM [73]. In our hands, the purified protein yield of rsTRPA1 was ~50% compared to human TRPA1 under similar expression and purification conditions. Since rsTRPA1 is activated in HEK293S GnTI<sup>-</sup> cell culture temperatures (37 °C and 30 °C), it is possible that the simultaneous opening of rsTRPA1 during expression is toxic to cells. Despite the presence of ruthenium red in cell culture, it is possible that not all channels are blocked. We used a similar procedure to express and purify rsTRPA1 and reconstituted it into nanodiscs with some key modifications to increase the yield and sample homogeneity. Notably, due to the low yield and in order to increase protein recovery, the first SEC after FLAG affinity purification was skipped, as the eluent from FLAG resin was directly used for nanodiscs reconstitution. Moreover, the potential toxicity of rsTRPA1 expression has triggered cellular protein misfolding response as we observed a significantly increased amount of molecular chaperone being co-purified with rsTRPA1. The chaperone contaminant was analyzed by LC-MS and confirmed to be mainly heat shock protein 70 (HSP70). HSP70 contains an ATPase domain and its affinity to protein

substrate reduces when bound to ATP [136], thus we included an ATP wash step during affinity purification and were able to remove ~50% of the HSP70 contaminant.

Furthermore, recently it was reported that reducing agents including DTT and TCEP have inhibitory effects on the temperature sensitivity of hTRPA1 [48]. Although there is no evidence that rsTRPA1 would undergo the same inhibition by reducing agents, we removed all reducing agents from protein purification procedures. Initial screening of the plunge frozen grids showed acceptable particle behavior, with individual particles visible, albeit less homogenous and monodisperse than hTRPA1. We subsequently collected a cryo-EM dataset on this sample. Because all purification procedures were performed at 4°C before plunge freezing, and there was no heating applied, the structure we observe here should be consider inactivate, or resting state of the rsTRPA1 channel (Table 2).

**Table 2: Cryo-EM data collection, refinement and validation statistics for rattlesnake TPRA1 structures**

	<b>Rattlesnake TRPA1 4 °C</b>
<b>Data Collection</b>	
Microscope	Titan Krios
Voltage (kV)	300
Nominal magnification	81,000x
Electron dose (e <sup>-</sup> Å <sup>-2</sup> )	50
Exposure rate (e <sup>-</sup> /pixel/sec)	15
Detector	Gatan K3
Pixel size (Å)	1.079
Defocus range (µm)	-2.5 to -0.75
<b>Reconstruction</b>	
Total extracted particles	713,674
Final particles	14,972
Symmetry imposed	C4
Resolution (global)	3.33 Å
FSC 0.5 (unmasked/masked)	3.40/3.30 Å
FSC 0.143 (unmasked/masked)	2.9/2.9 Å
Applied B-factor (Å <sup>2</sup> )	-30
<b>Refinement</b>	
Protein Residues	3,956
Ligand	0
Map correlation coefficient	0.82
R.m.s deviations	
Bond lengths (Å)	0.005
Bond angles (°)	0.896
Ramachandran plot	
Outliers	0.00%
Allowed	9.78%
Favored	92.70%
Poor rotamers	0.00%
MolProbity score	2.64
All-atom Clashscore	7.91

### **3.2 Overall Architecture of Rattlesnake TRPA1**

We solved the cryo-EM structure of rsTRPA1 to an overall resolution of 3.3 Å. The excellent map quality allowed *de novo* model building of the AR1-11 and other regions not resolved in previous hTRPA1 structures (Figure 15 and 23). The hTRPA1 and rsTRPA1 share 61% sequence identity, thus rsTRPA1 is expected to have similar structure as hTRPA1. Indeed, the transmembrane domains between two homologs are almost identical (Figure 17A and 17B). The S1-S2 linker, which adopts a three short beta strand structure in hTRPA1, was not resolved in rsTRPA1 structure. Multiple sequence alignment and secondary structure prediction also suggested that such beta strand structure does not exist in rsTRPA1. Compared to hTRPA1 structures, the density quality of the annular lipids was poor in rsTRPA1, thus we did not model these lipids. The S6 helix bundle gate, formed by Ile957 and Val961 adopted non-conducting conformation, and was consistent with the notion that sample was prepared in the resting state.

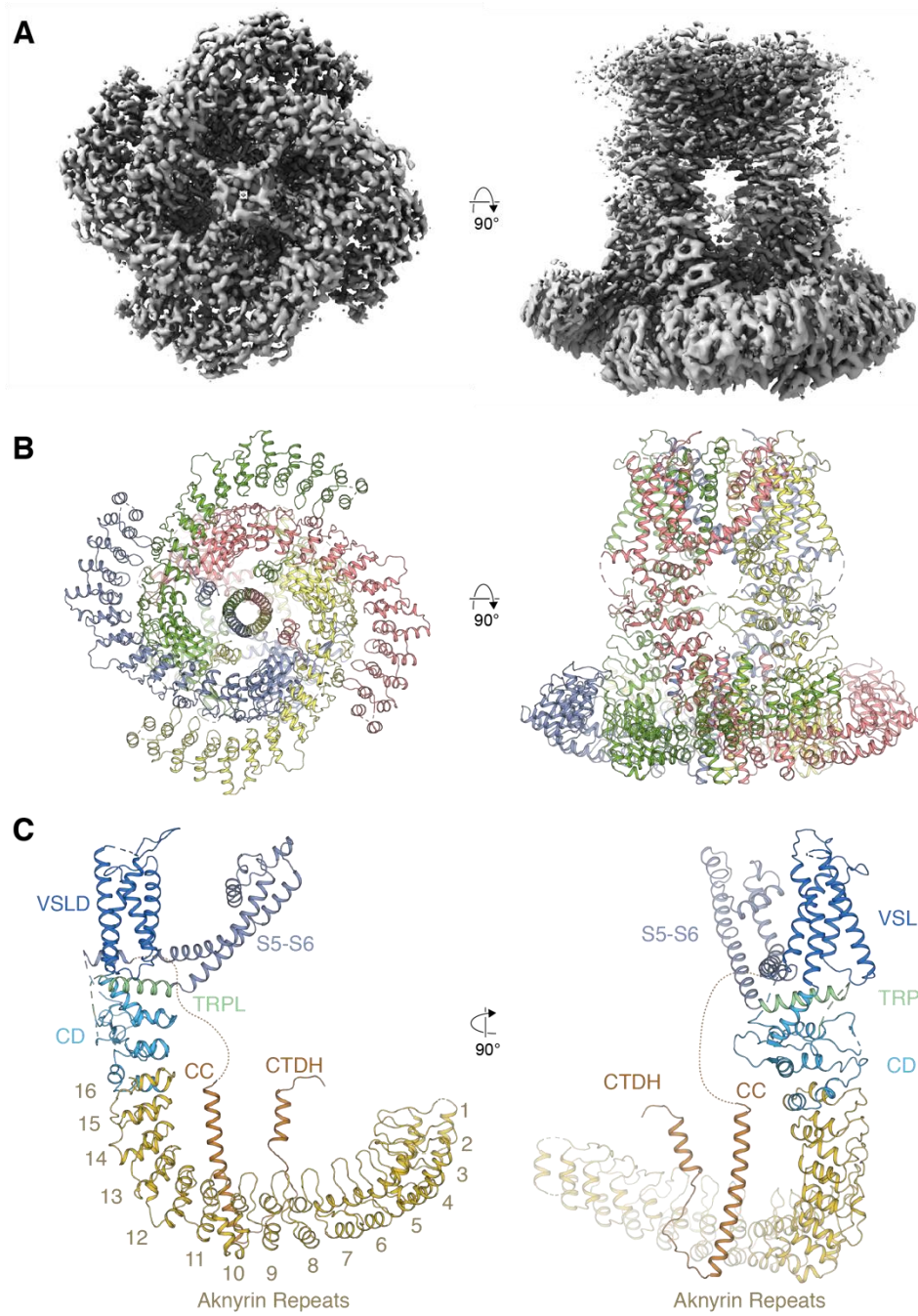


**Figure 15: Overall architecture of rattlesnake TRPA1.**

(A and B) 3D-reconstruction (A) and atomic model (B) of rattlesnake TRPA1. (C) The structural overview of a rattlesnake TRPA1 protomer, functional domains are labelled with different color.

In rsTRPA1 structure, the most striking new feature resolved were the AR1-11 domains. In our 3D reconstructions of rsTRPA1, the AR1-11 was very well ordered and resolved that allowed *de novo* model building (Figure 15). In previous hTRPA1 reconstructions, AR1-11 was visible in 3D reconstructions as fuzzy densities, and they were too flexible relative to the rest of the channel to be resolved by cryo-EM. Indeed, it was speculated that the AR1-11 in human TRPA1 acts as a propeller-like structure around central axis [73]. The rsTRPA1 AR1-11 was stabilized by extensive interactions, mainly through a neighboring ARD. To analyze this new interaction pattern, we used COCOMAPS to map this interface [137]. COCOMAPS server identified a major interaction interface between the N-terminal ARDs from two neighboring protomers (Figure 24). In one protomer, this interface spans from AR5 to AR8, while in the other protomer the interacting residues spans from AR11 to AR13. Because this interface is centered at AR6 and AR12 in respective protomers, we term this interface the AR6-AR12 interface (Figure 16A). Interestingly, the AR6-AR12 interface is composed of a variety of amino acid residues, including hydrophobic, charged and non-charged, polar residues, with a roughly equal distribution among three types (Figure 16B). This diversity in interface interaction draws stark contrast with NOMPC [138] in which the ARD-ARD interactions are predominantly charged and polar. This difference might be explained by the inherent difference in function between NOMPC and rsTRPA1 ARDs, where one is

considered to be a mechanic force sensor [138], while the other is hypothesized as the temperature sensor[68], respectively.

After inspecting all major inter-protomers analyzed by COCOMAPS, we then focused our analysis on the specific interactions between AR6 and AR12. The ankyrin repeat domains and specific residues were previously implicated as functionally crucial for temperature sensitivity [67, 139], and the functional studies we carried out also supported that this region could bear elements critical for function. On the AR6 side, we identified four most important residues in this interaction, Gln254, Ser255, Arg256 and Asp257. On the AR12 side, Thr478 interacts with Arg256 while Arg479 forms charged interaction with Asp257 (Figure 16C). We emphasized these residues because of the following reasons. First, Jabba et al. identified that a single Ser250Asn (rsTRPA1 equivalent Ser255) mutation could convert mouse TRPA1 from cold- to warm-sensitive [67], highlighting the critical role of this residue and its surrounding environment in temperature sensing. Furthermore, Tseng et al. discovered a small molecule hTRPA1 inhibitor which presumably binds to the region surrounding Asn249 (rsTRPA1 equivalent Ser255) [139], further demonstrating the criticality of this interface. Finally, among the interacting residues mapped in this interface, this region contains the most divergent residues between human, mouse and rattlesnake TRPA1 sequences (Figure 16D). Considering the diversity in their temperature sensing properties, their differences are most likely conferred by this region. We carried out site-directed mutagenesis and

electrophysiology experiments to validate our hypothesis (Figure 16E-F). We created several point or double mutations and recorded heat-activated response in *Xenopus laevis* oocytes and calculated the  $Q_{10}$  values of each mutant (Figure 16F). Many alanine mutants on the aforementioned AR6-AR12 interface had negative impact on channel heat sensitivity, including Ser255Ala. Strikingly, the charge-neutralizing and reversal mutations of Arg479Ala and Arg479Asp almost completely abolished heat sensitivity of rsTRPA1. Similar decrease of  $Q_{10}$  value were also observed in Asp257Ala/Arg479Ala double mutants. Interestingly, the charge swapping double mutant Asp257Arg/Arg479Asp could rescue the phenotype (Figure 16E-F). All the previous evidence, structural observation from rsTRPA1 and electrophysiology experiments could support the critical role of this AR6-AR12 interface in temperature sensing.

Furthermore, when compared with hTRPA1, the AR12-16 in rsTRPA1 seems to be bending or twisting counterclockwise (viewing from extracellular side) by about 20° (Figure 17A). The bending originated from Coupling and TRP-like domains, where pre-S1 helix and TRP-like domain swing counterclockwise by about 15°, together with the entire coupling domain and ARD. In this way, the entire ARD poses itself a spring-like structure. The twisting seems to be a result from a stabilized AR1-11 domain, where AR1-11 anchors itself with the ARD from a neighboring protomer through the ARD-ARD interface. This twisting reminisces the subtle conformational changes reported

previously between ligand-bound and ligand-free states of human TRPA1 [127] described in chapter 2, albeit much more pronounced.

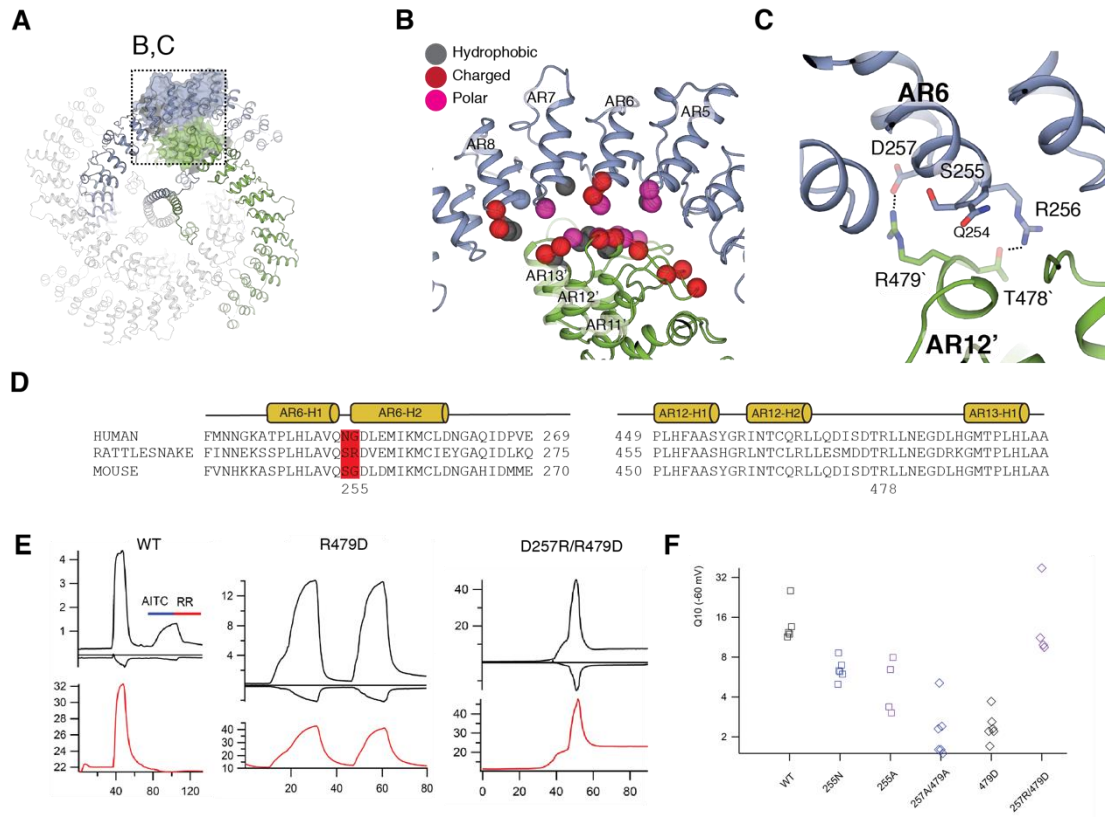


**Figure 16: The ARD-ARD interface could potentially be critical for temperature sensing.**

(A), The location of ARD-ARD interface within the whole channel. (B) close-up view of the AR6-AR12 interface, the interacting residues are labelled as spheres. Dark grey, red and pink spheres denote hydrophobic, charged and non-charged polar residues, respectively. (C), close-up view of the AR6-AR12 interface. Stick represents interacting residues. (D), Sequence alignment between human, rattlesnake and mouse TRPA1 showing the sequence conservation and divergence in AR6 and AR12-13. (E), TEVC recordings for rsTRPA1 WT and Ser255Asn, Asp257Arg/Arg479Asp mutants. (F), summary of  $Q_{10}$  values for key interface mutants.

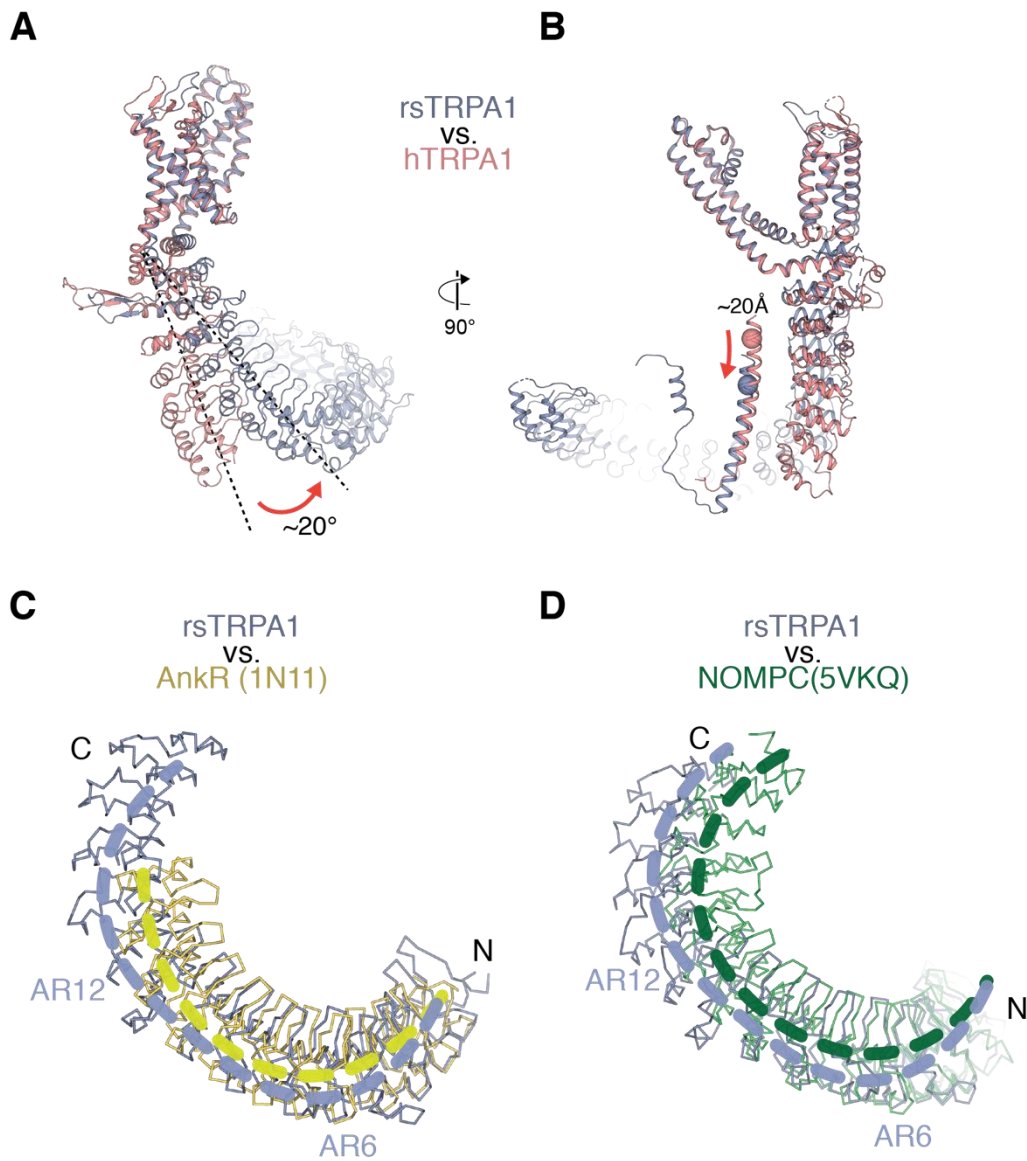


**Figure 17: rsTRPA1 ARD appears to be twisted comparing to other ankyrin repeats.**

(A), overlay of hTRPA1 (PDB ID: 6PQQ) and rsTRPA1 with transmembrane S1-S6 aligned, showing the bending of ARD and CD. (B), the same overlay with (A) and rotated 90 degrees, showing the movement of CC. Sphere denotes a conserved residue Glu1081 (human) or Glu1083(rattlesnake), (C) overlay of human Ankr (1N11) domain with rsTRPA1 ARD. (D), overlay of rsTRPA1 ARD and ARD of *Drosophila* NOMPC (5VKQ), showing the unusual bending.

Together with the twisting of AR11-16, the coiled-coil domain, which makes extensive interactions with AR12 and presumably stabilizes AR12-16 in hTRPA1, undergoes significant conformational changes in rsTRPA1. In rsTRPA1, the coiled-coil moves down away from the membrane by  $\sim 20\text{\AA}$ , measured by the movement of  $C\alpha$  of the conserved glutamine residue in the N-terminus of the CC (Glu1081 and Glu1083 for human and rattlesnake, respectively, Figure 17B). This downward movement is coupled to a change in CC-ARD interaction pattern. In hTRPA1, the CC possesses a cluster of conserved acidic residues that interact with AR12 from the neighboring protomer, including Gln1079 and Gln1081. In contrast, rsTRPA1 CC interacts with ARD through another cluster of acidic residues downstream, including Asp1079 and Asp1081 (equivalent to hTRPA1 Asp1083 and Asp1085). This change in interaction pattern is likely to be the reason CC sliding downwards. Interestingly, after the end of coiled coil helix, the peptide chain turned 180 degrees and folded back towards membrane. A newly resolved short helix was located there, and we term it C-terminal domain helix (CTDH). The CTDH was predicted by PSIPRED server [140] for both hTRPA1 and rsTRPA1 but was not previously resolved in hTRPA1.

A better resolved C-terminal domain allowed us to identify an interesting interaction of Trp1102 with coupling domain. It was previously shown that rsTRPA1 was not sensitive to AITC, despite the presence of the conserved reactive cysteines [68]. In rsTRPA1 structure, the presumed electrophile binding pocket seems intact, including

the two  $\alpha$ -helices providing helical dipole moment to the reactive Cys627 (human Cys621 equivalent), the benzene quadruple provider Phe618 (human Phe612 equivalent), and a hydrophobic residue-filled binding pocket, sharing great resemblance to hTRPA1 [127]. Interestingly however, Trp1102 from another subunit inserts its indole group into the binding pocket, making the pocket space relatively confined compared to hTRPA1. It is possible that the occupation of Trp1102 in electrophile binding pocket renders the pocket sterically hindered for electrophile binding, which might explain the weak electrophile sensitivity of rsTRPA1.

### ***3.3 Structural Basis for Heat-dependent Activation of Rattlesnake TRPA1***

Cordero-Morales et al. proposed that rsTRPA1 ARD acts as the thermal sensor [68]. Specifically, AR10-15 alone could confer heat sensitivity, while AR3-8 serves as an enhancer module on top of AR10-15. Moreover, Clapham and Miller's heat capacity change theory [71] would require the exposure of 40-80 residues to allow enough heat capacity change leading to channel activation. Applying this theory to rsTRPA1, there must be some form of conformational change happening upon temperature change, presumably around ARD-ARD interface, that exposes enough buried surface to the solvent and triggers subsequent gating.

Indeed, molecular dynamics simulations suggested that mouse TRPA1 ARD is capable of extending more than 60 Å when force is applied [141]. As previously

discussed, the rsTRPA1 ARD is dramatically twisted compared to hTRPA1. Moreover, comparing to conventional human ankyrin repeat domains such as AnkR (PDB ID: 1N11), the rsTRPA1 ARD appears to be slightly bent as well. Furthermore, the crystal structure of AnkR[142], the ARD of NOMPC [138] and rsTRPA1 structures all adopt a slightly different conformation (Figures 17C-D). Notably, when compared with AnkR and NOMPC ARDs, the rsTRPA1 ARD seems to be more distorted, and the distortion pivot point appears to be around AR6 and AR12 (Figures 17C-D). Consistent with the idea that ankyrin repeats could serve as molecular nano springs [143], the rsTRPA1 ARD is capable of undergoing significant conformational changes upon temperature change, and can transmit such change to coupling domain. It was previously proposed that AR10-15 serves as the primary module while AR3-8 serves as enhancer module in rsTRPA1 thermo sensation, and our rsTRPA1 structure showing such arrangement of ARD-CC interactions provides a structural support for this model. The potential conformational changes initiated either from AR3-8, or CC, or AR10-15 itself, can be propagated to AR10-15, which in turn can be transduced to the coupling domain, and finally trigger gating events.

Based on our observations and analysis on the ARD-ARD interface, together with patch-clamp electrophysiology data on mutants, we hypothesize the following model for temperature-dependent gating of the rsTRPA1 channel. A change in temperature would disassociate ARD-ARD interface, which is centered at AR6-AR12.

This conformational change further exposes a cluster of hydrophobic and polar residues, causing the change in heat capacity of the channel protein. Furthermore, this conformational change will be propagated through AR12 to the coupling domain, and subsequently trigger channel opening.

### **3.4 Discussion**

The thermosensitivity of TRPA1 has been controversial. Despite solid functional studies work has been done over the past few years regarding thermo sensitivity of TRPA1 channel across multiple species, the mechanism of temperature sensing by TRPA1 remains elusive. Here we report the rsTRPA1 structure with >90% of the peptide resolved and modelled, including AR1-11, which were missing from previous structures of TRPA1. AR1-11 was previously shown to be critical for temperature-dependent activation of TRPA1 [67, 68]. The Analysis on novel inter-protomer interactions in ARD led us propose a working model for the heat sensing for rattlesnake TRPA1. The interface between AR6 and AR12 contains 22-27 residues per protomer involved in interaction and is buried in the interface in our structure. This interface is composed of a variety of residues, and can have dramatic binding entropy/heat capacity change during temperature change. Moreover, the ARD of rsTRPA1 is unusually twisted comparing to hTRPA1 and other ARDs, in which energy could store in resting state we observe. We propose that during temperature rise, this interface would weaken and the transition

starts with the breaking of hydrogen bonding, which can be easily disrupted. The initial disruption of the interface could lead to exposure of hydrophobic residues and breaking of salt bridges, resulting a heat capacity change of the channel protein. A larger conformational change is then followed and presumably followed by the disengagement of ARD-ARD, releasing energy and causing the broader conformational change in the entire ARD, which transduces to CD, and trigger channel opening (Figure 18).

Because we lack direct evidence of this hypothesis, we refrain from drawing a solid conclusion. It would be beneficial to carry out molecular dynamics simulations in different temperatures, observing conformational changes and test our hypothesis. More directly, obtaining high-resolution structures with a heat-treated sample would help us validate or dispute our hypothesis. Regardless we observe channel opening in this heat-treated structure, we can start to draw conformational landscape of rsA1 and thus propose more meaningful hypothesis on thermal-sensitive channel conformational changes.

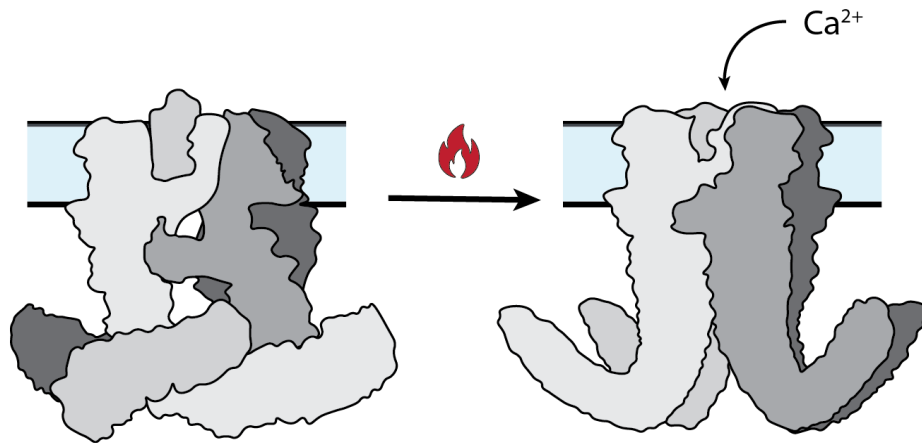


Figure 18: Proposed mechanism for rsTRPA1 heat activation.

### 3.5 Materials and Methods

#### 3.5.1 Rattlesnake TRPA1 expression, purification and nanodiscs reconstitution

Rattlesnake TRPA1 was expressed and purified using the similar manner as hTRPA1 described in previous section 2.6. In short, freshly harvested P3 baculovirus was used to infect 2-3 L HEK293S GnTI- cell culture. BME, DTT and TCEP were removed from all purification steps to avoid potential channel inhibition. The rsTRPA1 protein was solubilized and purified in digitonin, and the elution from FLAG affinity column was used directly for nanodiscs reconstitution. The rsTRPA1 was reconstituted in MSP2N2 nanodiscs with POPC:POPE:POPG=3:1:1 lipids in a 1:3:200 ratio where rsTRPA1 was treated as tetramer. The reconstitution mix was injected to Superose 6 for SEC equilibrated in detergent-free buffer (20 mM Tris pH8, 150 mM NaCl) for SEC

analysis and peak fractions were pooled and concentrated for cryo-EM sample preparation.

### **3.5.2 Cryo-EM sample preparation, data collection and data processing**

The peak fractions from the final size exclusion chromatography containing nanodisc-reconstituted rattlesnake TRPA1 were concentrated to  $\sim 0.6 \text{ mg ml}^{-1}$ . Samples were plunge frozen using Leica EM GP Automatic Plunge Freezer operated at  $4^\circ\text{C}$  and  $\sim 95\%$  humidity. A sample volume of  $3\mu\text{l}$  was applied to a freshly glow-discharged UltrAuFoil R1.2/1.3 300mesh (Quantifoil), blotted with Whatman No. 1 filter paper for 3 seconds followed by plunge-freezing in liquid-ethane cooled by liquid nitrogen.

rsTRPA1 dataset was collected using a Titan Krios (Thermo Fisher) transmission electron microscope operating at 300 kV equipped with a K3 detector in counting mode, using the SerialEM automated data acquisition program [92]. 2,444 movies were collected at a nominal magnification of  $81,000\times$  with a super-resolution pixel size of  $0.5395 \text{ \AA/pix}$  at specimen level. Each movie contains 61 frames over  $\sim 5 \text{ s}$  exposure time, using a dose rate of  $8 \text{ e}^-/\text{px}/\text{s}$ , resulting a total accumulated dose of  $40 \text{ e}^-/\text{\AA}^2$ . The nominal defocus range was set from  $-2.5$  to  $-0.75 \mu\text{m}$ .

Beam-induced motion correction and dose-weighting was performed using MotionCor2 [88] with  $2\times$  Fourier binning from super-resolution, followed by CTF estimation using Gctf [131]. 1,974 micrographs were selected for further data processing based on CTF fit quality.  $\sim 1,000$  particles were manually picked and subjected to a

reference-free 2D classification ( $k=10$ ,  $T=2$ ), from which the best six classes, showing defined TRPA1 features were selected as template for automated reference-based particle picking in RELION. A total of 171,134 particles were boxed and then extracted (4x4 binned) Reference free 2D classification ( $k=50$ ,  $T=2$ ) was performed in RELION and classes showing clear secondary structures are selected. A 3D auto-refinement without masking was then performed with the selected particles, using the TRPA1<sub>WT-JT010</sub> (EMDB-20449) map low-pass filtered to 30 Å as reference map. The refined particles were re-extracted, re-centered and un-binned (1.079 Å/pix, 256pix box size) and subjected to another round of 3D refinement, using the map generated from the previous 3D refinement. Particles and refined coordinates from this 3D refinement were then subjected to a no-alignment 3D classification ( $k=4$ ,  $T=20$ ), using a soft solvent mask covering the best resolved region of the channel. One best class, containing 13,325 particles, displayed the best-defined features of TRPA1 and was selected and subjected to 3D refinement, producing a 4.2 Å map. The particles from this 3D reconstruction were subjected to 2D classification, whose output was used to re-pick particles from original micrographs, resulting in 713,674 particles. A similar procedure as previously described was carried out, yielding a 3.6 Å map. Subsequently, three iterative rounds of CTF refinement and Bayesian polishing were carried out using RELION, which yielded a final map with 3.3 Å resolution. Local resolution was calculated using RELION 3.1 [83].

### 3.5.3 Two-electrode voltage clamp electrophysiology in *X. laevis* oocytes

The TEVC electrophysiology experiments were carried out by Dr. Feng Zhang. The WT rattlesnake TRPA1 channels was subcloned into the pGEM-HE vector. The construct was linearized with SbfI and cRNA was synthesized by in vitro transcription using T7 RNA polymerase (Thermo Fisher). rsTRPA1 cRNA was injected to *Xenopus laevis* oocytes and incubated at 17 °C for 1-2 days in a solution containing (in mM) 96 NaCl, 2 KCl, 1 MgCl<sub>2</sub>, 1.8 CaCl<sub>2</sub>, 5 HEPES, pH 7.6 (with NaOH). All defolliculated oocytes were ordered from Ecocyte (Austin, Texas). For the two-electrode voltage clamp (TEVC) recording, oocyte membrane voltage was controlled using an OC-725C oocyte clamp (Warner Instruments, Hamden, CT). Data were filtered at 1–3 kHz and digitized at 20 kHz using pClamp software (Molecular Devices, Sunnyvale, CA) and a Digidata 1440A digitizer (Axon Instruments). Microelectrode resistances were 0.1–1 MΩ and filled with 3 M KCl. The external recording solution contained 100 mM KCl, 2 mM MgCl<sub>2</sub>, 10 mM HEPES, pH 7.6 (with KOH) and 0.01 mM 2-[(4-methoxy)-2-naphthalenyl]amino]-5-nitro-benzoic acid (Tocris), and 0.01 mM flufenamic acid were added to the recording solution to minimize calcium-activated chloride currents. AITC and Ruthenium Red (RR) were applied using a gravity-fed perfusion system. Voltage was initially held at –60 mV and ramped to +60 mV for 300 ms every 0.5 s. Heat stimuli were achieved by passing the external recording solution through glass capillary coils immersed in a water bath maintained at about 70-80 °C, and recordings were performed during constant perfusion with temperature

measured using a thermistor (TA-29, Warner Instruments). The thermistor was connected to the digitizer via a temperature controller (TC-324B, Warner Instruments). All data analysis was carried out using Igor Pro 6.3 (Wavemetrics, Portland, OR). Q10 values were calculated using the equation

$$Q_{10} = 10^{\frac{10 \times (-S_{Arrhe})}{T_1 \times T_2}}$$

where  $S_{Arrhe}$  is the slope of linear fit to Arrhenius plotted data between absolute temperatures  $T_1$  and  $T_2$  [59].

## 4. Conclusions

In this work, we report human TRPA1 structures in a ligand-free state, JT010-bound and BITC-bound conformations. These structures were the first high resolution TRPA1 structures since the 4 Å resolution structure reported in 2015. Our structures with different ligand bound not only elucidated the mechanism of exceptionally high reactivity of Cys621 using a simple model, in which the Cys621 is positioned within a rigid and tightly regulated chemical environment, but also explained the promiscuity of Cys621 being able to accept many structurally diverse electrophiles. We also observed the conformational changes around the ligand binding pocket and beyond, where the upper clamshell loop flips out to adopt the ligand, and presumably transduce the conformational change to the channel. Thanks to the higher resolution in our structures, we were also able to correct some of the register errors in ambiguously modelled areas in the 2015 structure. After our work was published, Zhao et al. reported a series of TRPA1 structures, in which our model of channel activation upon electrophile ligand binding largely coincided [144].

We also solved the high-resolution rattlesnake TRPA1 structure in the resting state. This structure revealed unprecedented AR1-11 which was not resolved in previous human TRPA1 structures. Using this new structure, we analyzed critical interactions in AR1-11 which provided insights on temperature sensitivity of rattlesnake TRPA1

channel, and we hope the findings we have on rattlesnake TRPA1 channel can be readily used to explain the diverse temperature sensitivity of TRPA1 across species.

Since 2013, the “resolution revolution” in cryo-EM has provided us a more powerful than ever tool for structural determination. In the short span of my graduate school years from 2014-2020, we witnessed an explosion of TRP channel structures. Indeed, we went from having nearly no structural information on TRP channels to having at least one structure in every TRP channel subfamily, and in some cases we have the entire conformational ensembles structurally available [145]. Looking forward, there is still much work to be done. First, despite the human TRPA1 with an open gate conformation has been reported [144], it is still imperative to obtain structures with more physiologically relevant ligand-induced open conformations, in order to avoid artifacts brought into structures that are irrelevant to its intrinsic mechanism. Moreover, as mentioned in the introduction (Section 1.1), the biased signaling mechanism of TRPA1 channels are getting traction [30, 31, 146], yet currently the TRPA1 structures are too scarce to reveal why and how different agonists could induce different response. It would be fascinating if we could obtain different conformations in complex with different agonists and hopefully to begin explaining the molecular mechanism of TRPA1 biased agonism. For rattlesnake TRPA1, it is imperative that we obtain a heat-induced open structure. Since rattlesnake TRPA1 is biochemically unstable, this task has proven challenging. We will need to find ways to stabilize the protein when heated, and

hopefully solve more structures with heat-treated sample, in order to come up with a series of conformational changes from heat-induced conformational changes leading to channel opening. By explaining how rattlesnake TRPA1 response to heat structurally, we hope to apply our knowledge to mammalian TRPA1 and hopefully explain the structural basis for their differences in thermo sensitivity.

# Appendix A: Supplementary Figures

## Human vs. rattlesnake

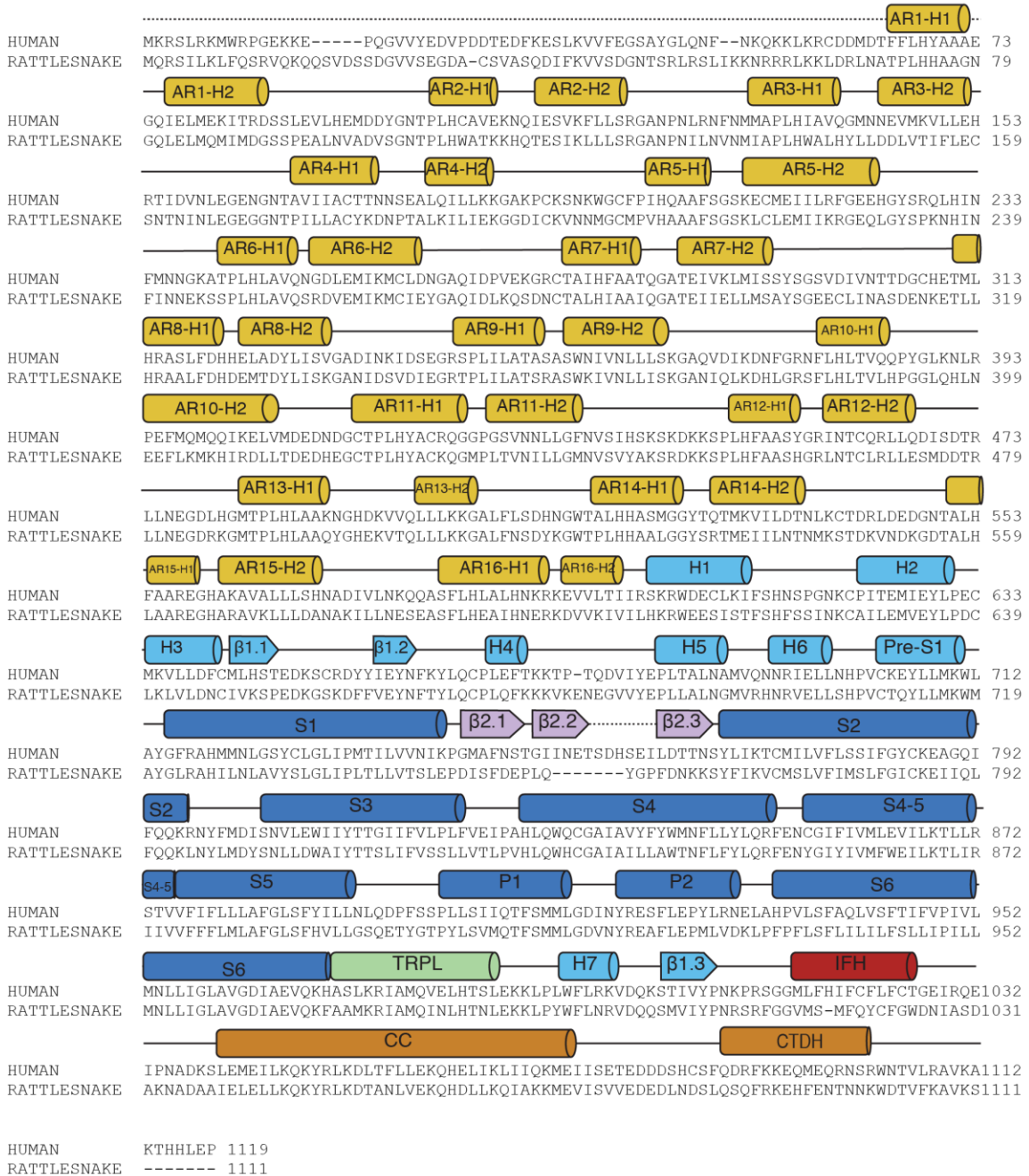
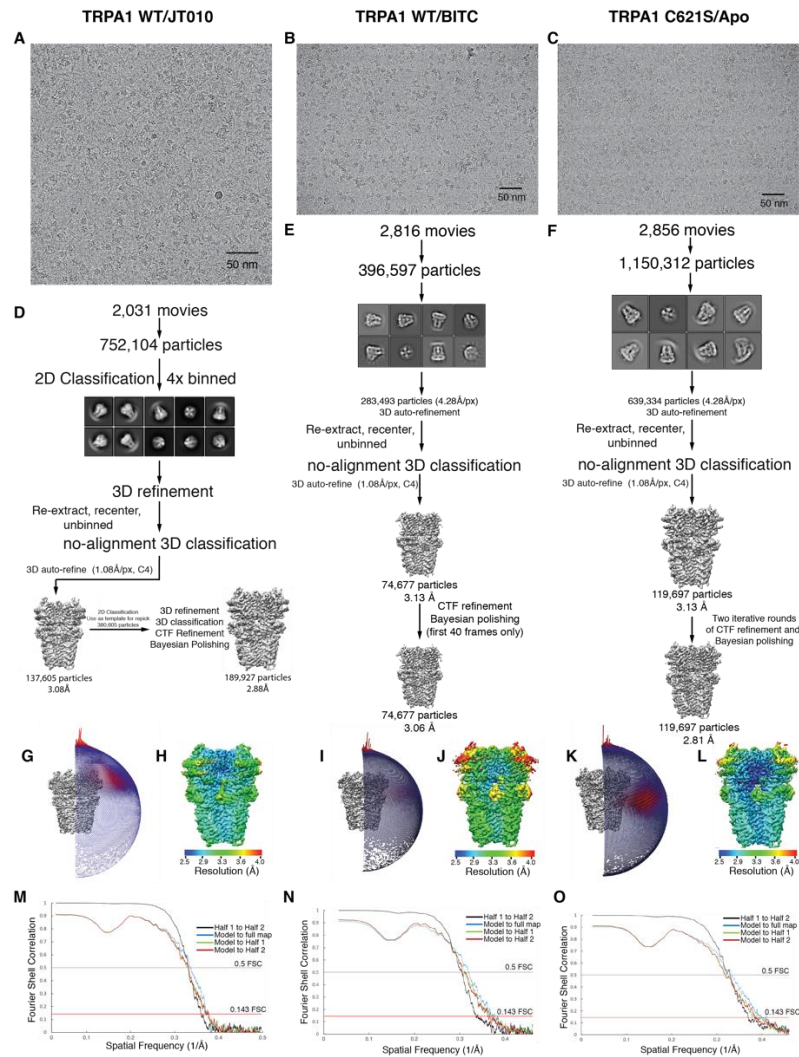
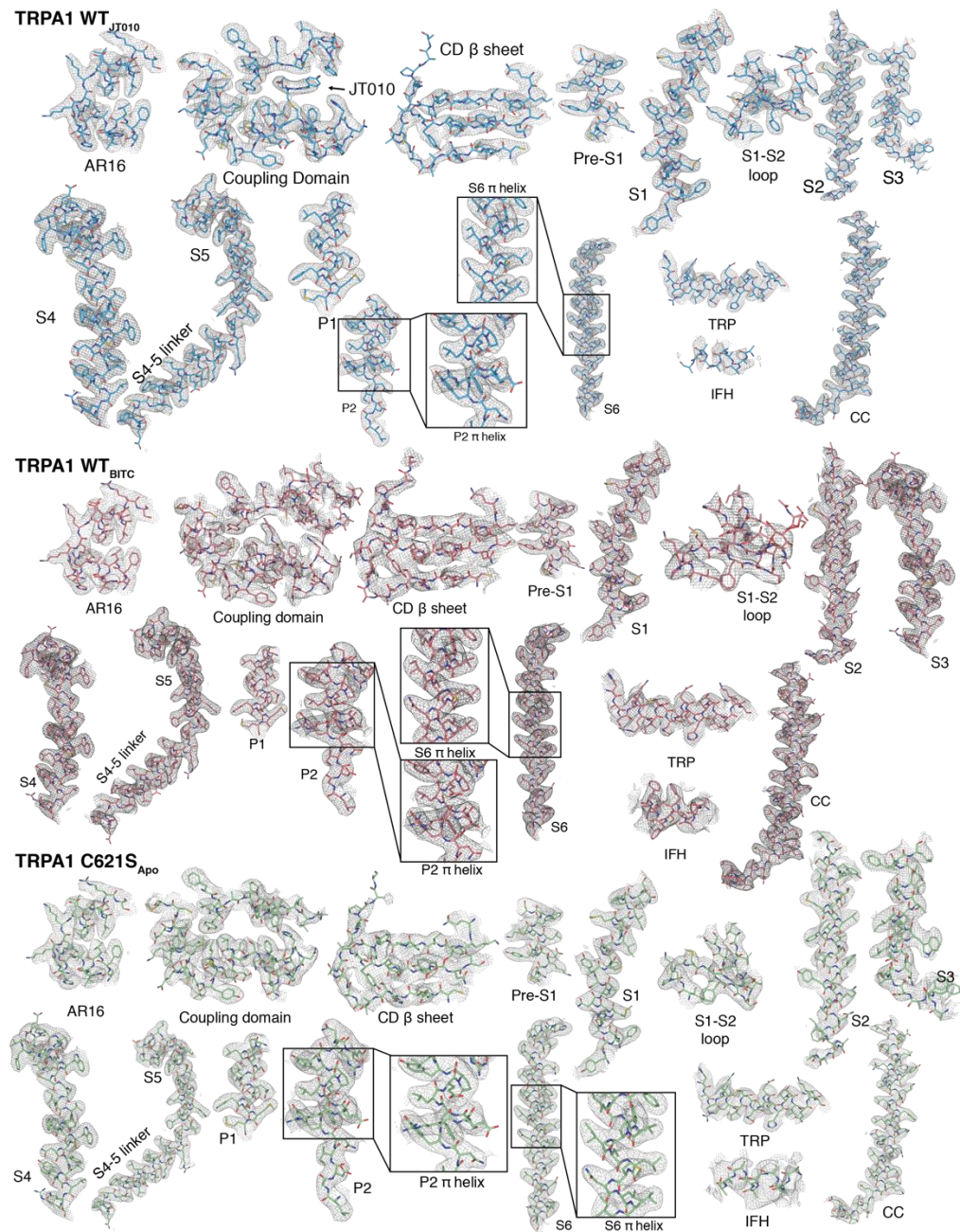


Figure 19: Sequence alignment between human and rattlesnake TRPA1.



**Figure 20: Overview of human TRPA1 cryo-EM data processing.**

(A-C) A representative micrograph from the TRPA1<sub>WT-JT010</sub>(A), TRPA1<sub>WT-BITC</sub> (B) and TRPA1<sub>C621S-Apo</sub>(C) datasets, respectively. (D-F) Data processing procedure of the TRPA1<sub>WT-JT010</sub>(D), TRPA1<sub>WT-BITC</sub> (E) and TRPA1<sub>C621S-Apo</sub> (F) datasets, respectively. (G, I, K) Euler distribution plot of the TRPA1<sub>WT-JT010</sub>(G), TRPA1<sub>WT-BITC</sub> (I) and TRPA1<sub>C621S-Apo</sub> (K) datasets, respectively. The red regions indicate the most represented views. (H, J, L) Local resolution in the 3D reconstruction of the TRPA1<sub>WT-JT010</sub>(H), TRPA1<sub>WT-BITC</sub> (J) and TRPA1<sub>C621S-Apo</sub> (L) datasets, respectively, calculated in RELION. (M-O) FSC curves of the TRPA1<sub>WT-JT010</sub>(M), TRPA1<sub>WT-BITC</sub> (N) and TRPA1<sub>C621S-Apo</sub> (O) datasets, respectively. Model-to-map (blue), model-to-half map 1 (green), model-to-half map 2 (red) and half map 1-to-half map 2 (black).



**Figure 21: Cryo-EM density coverage around key structural elements in human TRPA1 reconstructions.**

(A) TRPA1<sub>WT-JT010</sub> (thresholding 0.02), (B) TRPA1<sub>WT-BITC</sub> (thresholding 0.018), and (C) TRPA1<sub>C621S-Apo</sub> (thresholding 0.017).

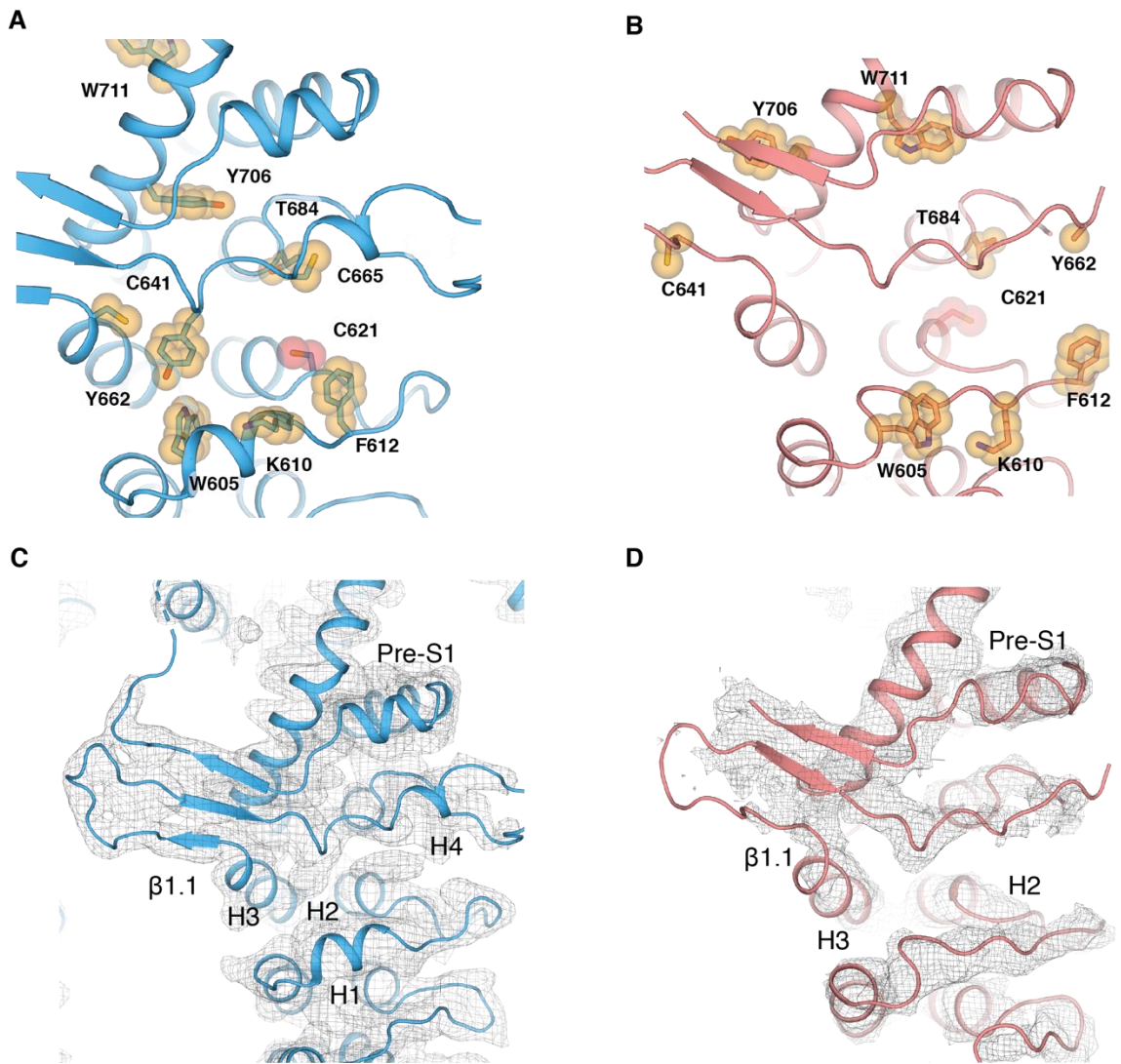


**Figure 22: Comparison with the previously published structure of human TRPA1 (PDB ID 3J9P).**

(A) Coordinates and cryo-EM density of the TRPA1<sub>WT-JT010</sub> coupling domain structure. (B) Coordinates of the previously reported human TRPA1 coupling domain structure (PDB ID 3J9P). Representative residues are shown in stick and sphere representation in the coupling domain in (A) and (B) to illustrate differences in the register. (C) Cryo-EM map of the TRPA1<sub>WT-JT010</sub> coupling domain region. The cryo-EM map is zoned at 0.02 thresholding. (D) Cryo-EM map of the previous published TRPA1 coupling domain region (EMD-6267). The cryo-EM map is zoned at 0.06 thresholding.

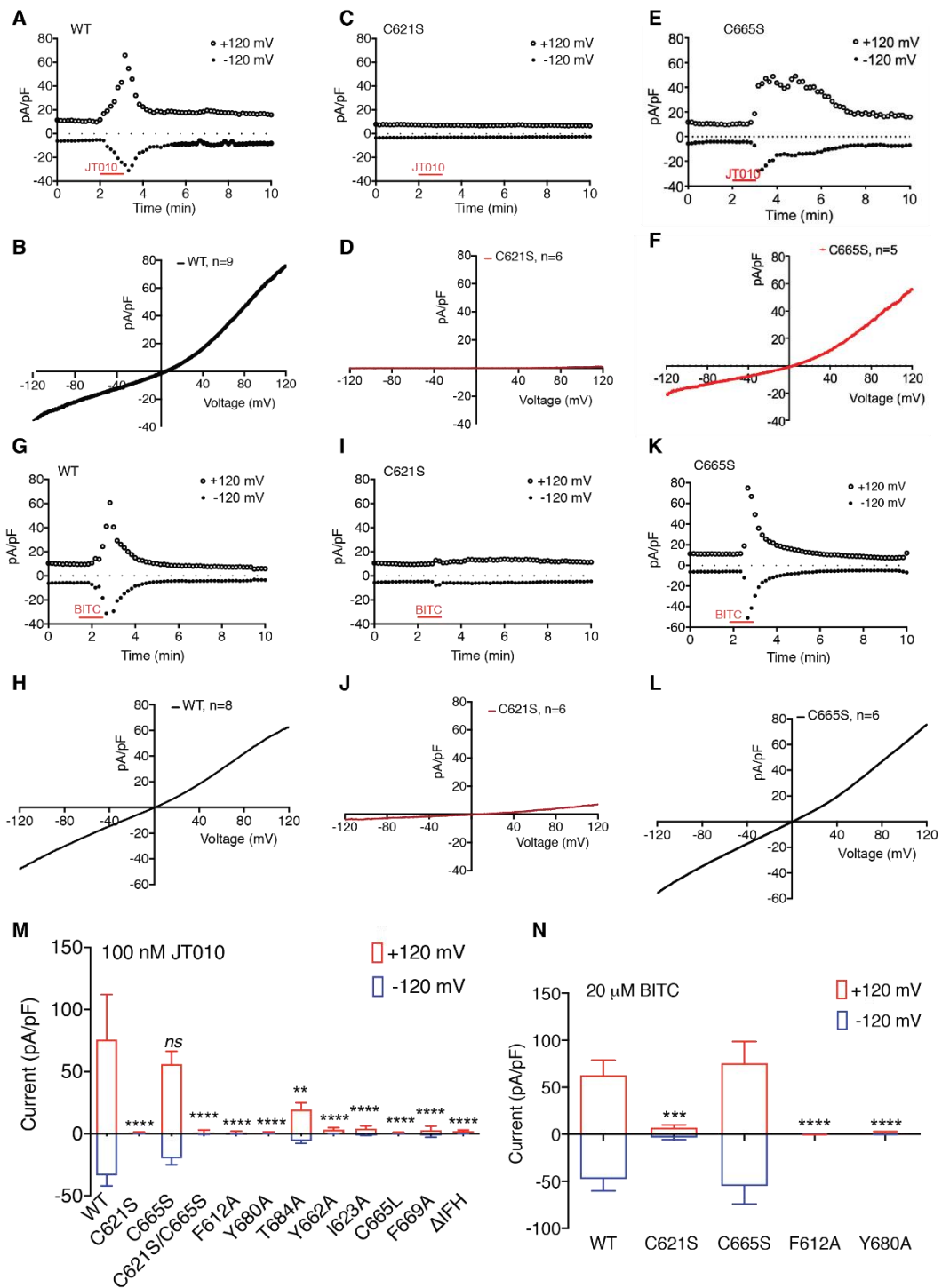


**Figure 23: Electrophysiology characterization of hTRPA1.**

Captions follow in next page.

(A-C) Current recordings of hTRPA1 wild-type (A), Cys621Ser (B) and Cys665Ser (C) mutants elicited by JT010. Wild-type hTRPA1 responds robustly to application of JT010. However, the JT010-induced current is abolished in HEK293T cells transfected with the Cys621Ser mutant. Upper panel represents outward and inward currents recorded at +120 mV and -120 mV, respectively, lower panel represents current-voltage relationship after JT010 application (100 nM). (D-F) Current recordings of hTRPA1 wild-type (D), Cys621Ser (E) and Cys665Ser (F) constructs elicited by BITC. The BITC-induced current is abolished in HEK293T cells transfected with the Cys621Ser mutant while Cys665Ser mutant exhibits a similar response to BITC as wild-type. Upper panel represents outward and inward currents recorded at +120 mV and -120 mV, respectively. Lower panel represents current-voltage relationship after BITC application (20  $\mu$ M). (G) Effect of binding site mutations on the TRPA1 JT010 response. (WT: n = 9, Cys621Ser: n=6, Cys665Ser: n=5, Cys621Ser/Cys665Ser: n=7, Phe612Ala: n=5, Tyr680Ala: n=5, Thr684Ala: n=5, Tyr662Ala: n=9, Ile623Ala: n=6, Cys665Leu: n=7, Phe669Ala: n=9, and  $\Delta$ IFH: n=8 cells per group) \*\*P < 0.01, \*\*\*P < 0.001, \*\*\*\*P < 0.0001, WT vs. mutants, two-way ANOVA, followed by Bonferroni's post hoc test. Only one cell was recorded from each cover slip. Data represent mean  $\pm$  S.E.M. (H) Inward and outward current density of WT and mutant hTRPA1 elicited by 20  $\mu$ M BITC at -120 mV and +120 mV (WT: n = 8, Cys621Ser: n=6, Cys665Ser: n=6, Tyr680Ala: n=8, Phe612Ala: n=8), and by 200  $\mu$ M BITC, (WT: n=5, Cys621Ser: n=8). \*\*P < 0.01, \*\*\*P < 0.001, WT vs. mutants, two-way ANOVA, followed by Bonferroni's post hoc test. Data represent mean  $\pm$  S.E.M.

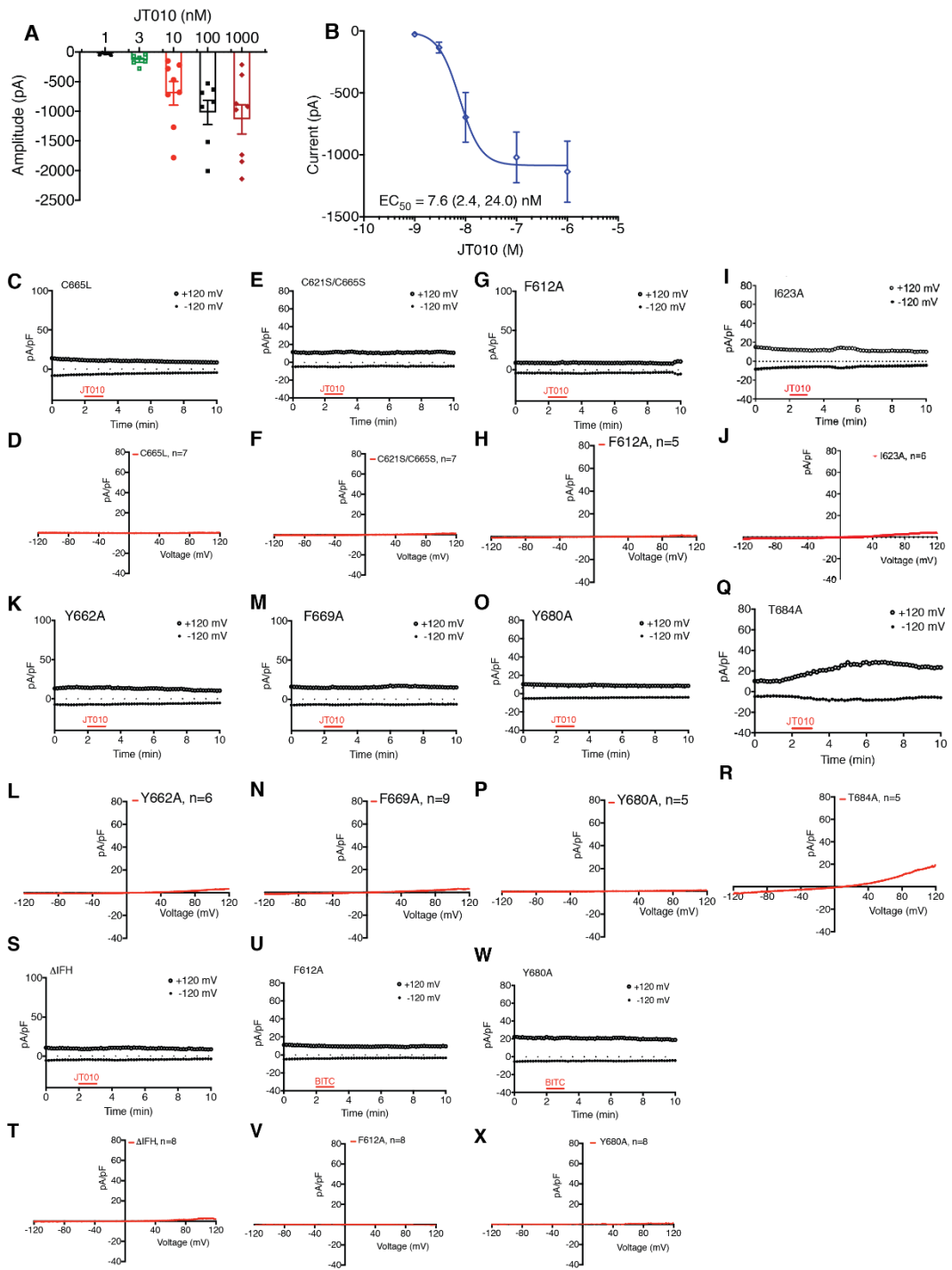


**Figure 24: Electrophysiology characterization of hTRPA1.**

Captions follow on next page.

(A and B) Dose-response curve of inward currents (-70 mV) induced by JT010 in WT-TRPA1. (C) Time-dependent decay was observed upon prolonged (4 minutes) exposure of WT TRPA1 to 100 nM JT010. Data are shown as Mean  $\pm$  S.E.M. n=8. (D-L) Currents and current-voltage relationship in WT and mutant hTRPA1 elicited by 100 nM JT010. Induced inward current (-120 mV) and outward currents (+120 mV) in TRPA1 mutants Cys665Leu (D), Cys621Ser/Cys665Ser (E), Phe612Ala (F), Ile623Ala (G), Tyr662Ala (H), Phe669Ala (I), Tyr680Ala (J), Thr684Ala (K), and  $\Delta$ IFH (L). Upper panel shows JT010-induced currents in TRPA1 mutants at  $\pm$  120 mV while lower panel shows voltage-current relationships in TRPA1 mutants after JT010 application. (M-N) BITC-induced inward currents (-120 mV) and outward currents (+120 mV), as well as the current-voltage relationship in Phe612Ala (M), and Tyr680Ala (N) elicited by application of 20  $\mu$ M BITC; The number of replicates (n) is indicated in the individual panels. (O-P) BITC-induced inward currents (-120 mV) and outward currents (+120 mV), as well as the current-voltage relationship in WT (O), and Cys621Ser (P) after application of 200  $\mu$ M BITC; The number of replicates (n) is indicated in the individual panels.

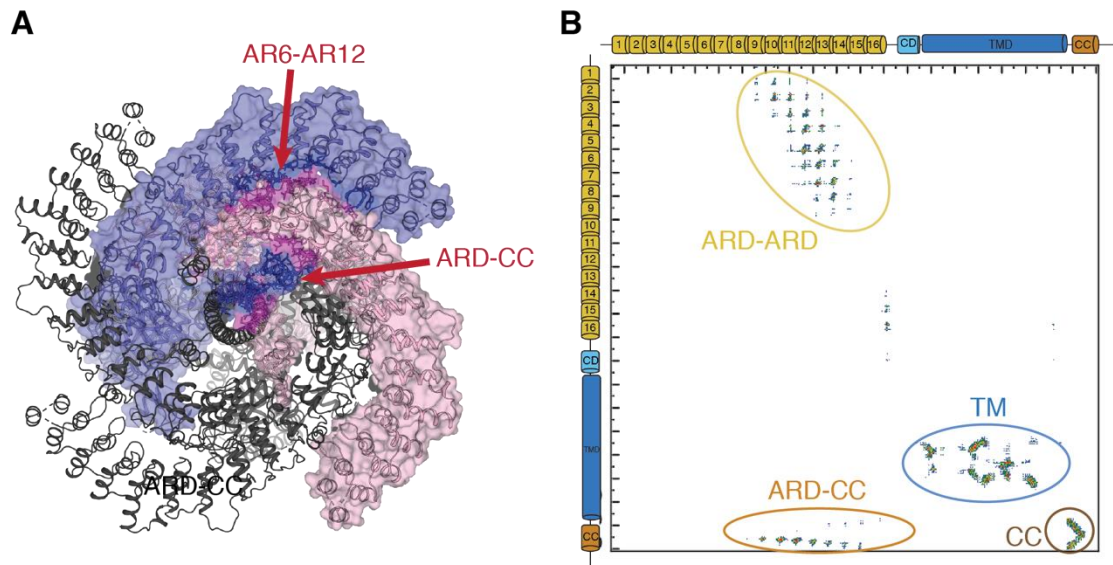


**Figure 25: COCOMAPS analysis of rsTRPA1 interactions.**

(A), COCOMAP identified two major interfaces in ARD, ARD-ARD interface and ARD-CC interface. (B) Protomer-protomer interaction profile. Major inter-protomer interaction clusters are circled. TM: Transmembrane domain, CC: Coiled-coil domain. Surface in (A) and 2D-profile in (B) were generated using COCOMAP server [137].

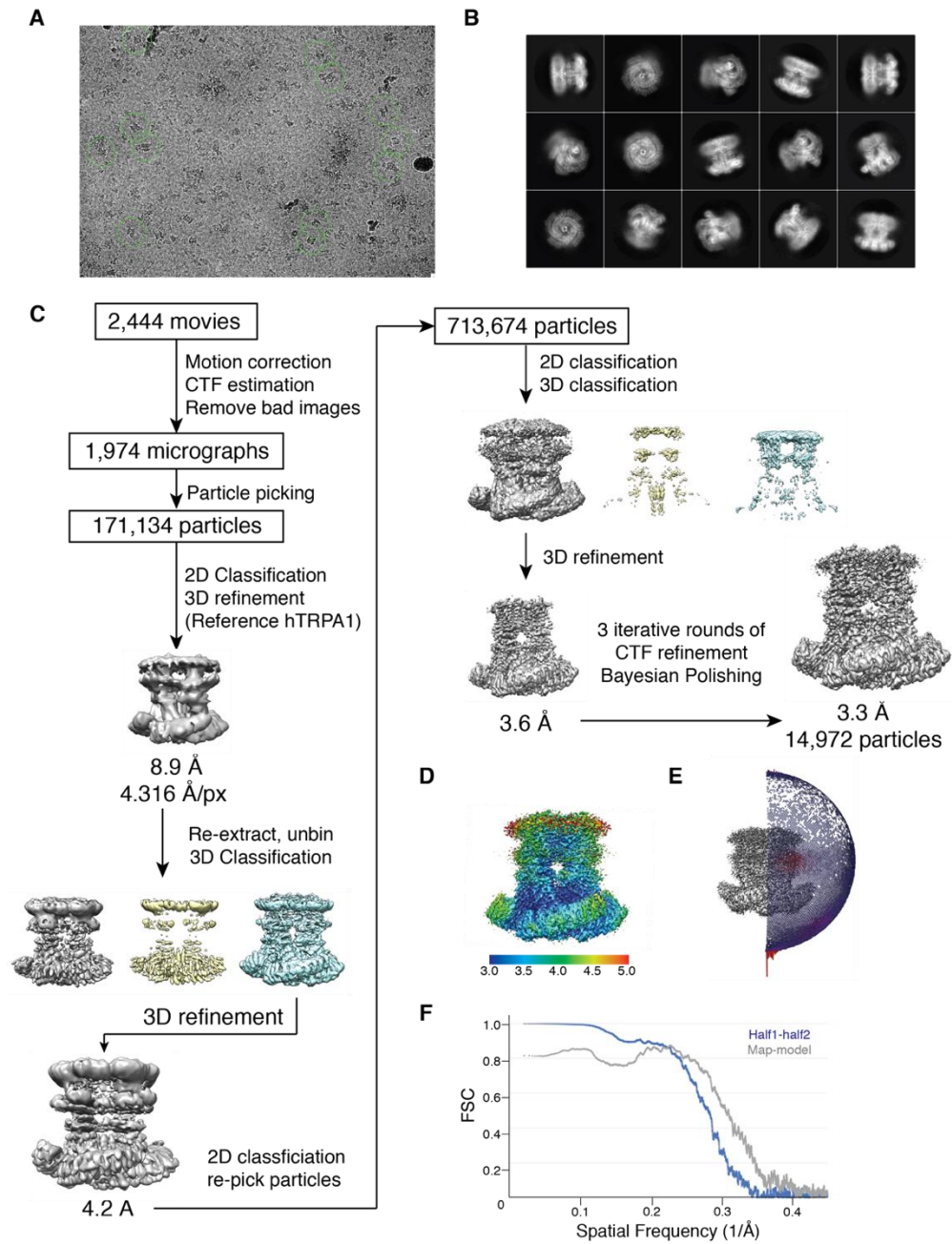


**Figure 26: rsTRPA1 cryo-EM data processing.**

(A), representative micrograph of the rsTRPA1 dataset, representative rsTRPA1 particles are circled. (B), representative 2D class averages. (C) Data processing workflow. (D), Local resolution plot. (E), angular distribution plot. (F) Fourier shell correlation (FSC) plots.

## References

1. Wang, H. and C.J. Woolf, *Pain TRPs*. Neuron, 2005. **46**(1): p. 9-12.
2. Nilius, B. and G. Owsianik, *The transient receptor potential family of ion channels*. Genome biology, 2011. **12**(3): p. 1-11.
3. Jaquemar, D., T. Schenker, and B. Trueb, *An ankyrin-like protein with transmembrane domains is specifically lost after oncogenic transformation of human fibroblasts*. Journal of Biological Chemistry, 1999. **274**(11): p. 7325-7333.
4. Story, G.M., et al., *ANKTM1, a TRP-like channel expressed in nociceptive neurons, is activated by cold temperatures*. Cell, 2003. **112**(6): p. 819-829.
5. Talavera, K., et al., *Mammalian Transient Receptor Potential TRPA1 Channels: From Structure to Disease*. Physiol Rev, 2020. **100**(2): p. 725-803.
6. La, J.-H., E.S. Schwartz, and G. Gebhart, *Differences in the expression of transient receptor potential channel V1, transient receptor potential channel A1 and mechanosensitive two pore-domain K<sup>+</sup> channels between the lumbar splanchnic and pelvic nerve innervations of mouse urinary bladder and colon*. Neuroscience, 2011. **186**: p. 179-187.
7. Bautista, D.M., et al., *Pungent products from garlic activate the sensory ion channel TRPA1*. Proceedings of the National Academy of Sciences, 2005. **102**(34): p. 12248-12252.
8. Bautista, D.M., et al., *TRPA1 mediates the inflammatory actions of environmental irritants and proalgesic agents*. Cell, 2006. **124**(6): p. 1269-1282.
9. Salas, M.M., K.M. Hargreaves, and A.N. Akopian, *TRPA1 - mediated responses in trigeminal sensory neurons: interaction between TRPA1 and TRPV1*. European Journal of Neuroscience, 2009. **29**(8): p. 1568-1578.
10. Fischer, M.J., et al., *Direct evidence for functional TRPV1/TRPA1 heteromers*. Pflügers Archiv-European Journal of Physiology, 2014. **466**(12): p. 2229-2241.
11. Bandell, M., et al., *Noxious cold ion channel TRPA1 is activated by pungent compounds and bradykinin*. Neuron, 2004. **41**(6): p. 849-857.
12. Hinman, A., et al., *TRP channel activation by reversible covalent modification*. Proc Natl Acad Sci U S A, 2006. **103**(51): p. 19564-8.

13. Jordt, S.E., et al., *Mustard oils and cannabinoids excite sensory nerve fibres through the TRP channel ANKTM1*. *Nature*, 2004. **427**(6971): p. 260-265.
14. McNamara, C.R., et al., *TRPA1 mediates formalin-induced pain*. *Proceedings of the National Academy of Sciences*, 2007. **104**(33): p. 13525-13530.
15. Taylor-Clark, T.E., et al., *Nitrooleic acid, an endogenous product of nitrative stress, activates nociceptive sensory nerves via the direct activation of TRPA1*. *Mol Pharmacol*, 2009. **75**(4): p. 820-9.
16. Taylor-Clark, T.E., et al., *Prostaglandin-induced activation of nociceptive neurons via direct interaction with transient receptor potential A1 (TRPA1)*. *Molecular pharmacology*, 2008. **73**(2): p. 274-281.
17. Trevisani, M., et al., *4-Hydroxynonenal, an endogenous aldehyde, causes pain and neurogenic inflammation through activation of the irritant receptor TRPA1*. *Proceedings of the National Academy of Sciences of the United States of America*, 2007. **104**(33): p. 13519-13524.
18. Nassini, R., et al., *The TRPA1 channel in inflammatory and neuropathic pain and migraine*. *Reviews of Physiology, Biochemistry and Pharmacology*, Vol. 167, 2014: p. 1-43.
19. Wilson, S.R., et al., *TRPA1 is required for histamine-independent, Mas-related G protein-coupled receptor-mediated itch*. *Nature neuroscience*, 2011. **14**(5): p. 595-602.
20. Wilson, S.R., et al., *The ion channel TRPA1 is required for chronic itch*. *Journal of Neuroscience*, 2013. **33**(22): p. 9283-9294.
21. Han, Q., et al., *miRNA-711 Binds and Activates TRPA1 Extracellularly to Evoke Acute and Chronic Pruritus*. *Neuron*, 2018. **99**(3): p. 449-463 e6.
22. Weyer-Menkhoff, I. and J. Lotsch, *Human pharmacological approaches to TRP-ion-channel-based analgesic drug development*. *Drug Discov Today*, 2018. **23**(12): p. 2003-2012.
23. Xie, Z. and H. Hu, *TRP Channels as Drug Targets to Relieve Itch*. *Pharmaceuticals (Basel)*, 2018. **11**(4): p. 100.
24. Koivisto, A., et al., *TRPA1 Antagonists for Pain Relief*. *Pharmaceuticals (Basel)*, 2018. **11**(4): p. 117.

25. Skerratt, S., *Recent progress in the discovery and development of TRPA1 modulators*. Progress in medicinal chemistry, 2017. **56**: p. 81-115.
26. Kremeyer, B., et al., *A gain-of-function mutation in TRPA1 causes familial episodic pain syndrome*. Neuron, 2010. **66**(5): p. 671-80.
27. Bahia, P.K., et al., *The exceptionally high reactivity of Cys 621 is critical for electrophilic activation of the sensory nerve ion channel TRPA1*. J Gen Physiol, 2016. **147**(6): p. 451-65.
28. Macpherson, L.J., et al., *Noxious compounds activate TRPA1 ion channels through covalent modification of cysteines*. Nature, 2007. **445**(7127): p. 541-5.
29. Ross, S.E., *Pain and itch: insights into the neural circuits of aversive somatosensation in health and disease*. Current opinion in neurobiology, 2011. **21**(6): p. 880-887.
30. Liu, C., et al., *A Non-covalent Ligand Reveals Biased Agonism of the TRPA1 Ion Channel*. Neuron, 2021. **109**: p. 1-12.
31. King, J.V.L., et al., *A cell-penetrating scorpion toxin enables mode-specific modulation of TRPA1 and pain*. Cell, 2019. **178**(6): p. 1362-1374. e16.
32. Zygmunt, P.M. and E.D. Högestätt, *TRPA1*, in *Mammalian Transient Receptor Potential (TRP) Cation Channels: Volume I*, B. Nilius and V. Flockerzi, Editors. 2014, Springer Berlin Heidelberg: Berlin, Heidelberg. p. 583-630.
33. Meents, J.E., C.I. Ciotu, and M.J. Fischer, *TRPA1: a molecular view*. Journal of neurophysiology, 2019. **121**(2): p. 427-443.
34. Balemans, D., et al., *Transient receptor potential ion channel function in sensory transduction and cellular signaling cascades underlying visceral hypersensitivity*. American Journal of Physiology-Gastrointestinal and Liver Physiology, 2017. **312**(6): p. G635-G648.
35. Beckers, A., et al., *transient receptor potential channels as possible therapeutic targets in irritable bowel syndrome*. Alimentary pharmacology & therapeutics, 2017. **46**(10): p. 938-952.
36. Jardín, I., et al., *TRPs in pain sensation*. Frontiers in physiology, 2017. **8**: p. 392.
37. Simon, S.A. and R. Gutierrez, *TRP Channels at the Periphery of the Taste and Trigeminal Systems*. Neurobiology of TRP channels, 2017: p. 113-124.

38. Saito, S. and M. Tominaga, *Evolutionary tuning of TRPA1 and TRPV1 thermal and chemical sensitivity in vertebrates*. *Temperature*, 2017. **4**(2): p. 141-152.
39. Rosasco, M.G. and S.E. Gordon, *TRP channels: What do they look like*. *Neurobiology of TRP Channels*, 2nd ed.; Emir, TLR, Ed, 2017: p. 1-9.
40. Nazıroğlu, M. and N. Braidı, *Thermo-sensitive TRP channels: novel targets for treating chemotherapy-induced peripheral pain*. *Frontiers in Physiology*, 2017. **8**: p. 1040.
41. Moore, C., et al., *Regulation of pain and itch by TRP channels*. *Neuroscience bulletin*, 2018. **34**(1): p. 120-142.
42. Bandell, M., L.J. Macpherson, and A. Patapoutian, *From chills to chilis: mechanisms for thermosensation and chemesthesis via thermoTRPs*. *Current opinion in neurobiology*, 2007. **17**(4): p. 490-497.
43. Eigenbrod, O., et al., *Rapid molecular evolution of pain insensitivity in multiple African rodents*. *Science*, 2019. **364**(6443): p. 852-859.
44. Takaya, J., et al., *A Potent and Site-Selective Agonist of TRPA1*. *J Am Chem Soc*, 2015. **137**(50): p. 15859-64.
45. Heber, S., et al., *A human TRPA1-specific pain model*. *Journal of Neuroscience*, 2019. **39**(20): p. 3845-3855.
46. Halliwell, B., *Antioxidant defence mechanisms: from the beginning to the end (of the beginning)*. *Free radical research*, 1999. **31**(4): p. 261-272.
47. Zubcevic, L., *Temperature - sensitive transient receptor potential vanilloid channels: structural insights into ligand - dependent activation*. *British Journal of Pharmacology*, 2020.
48. Moparthy, L., et al., *Human TRPA1 is a heat sensor displaying intrinsic U-shaped thermosensitivity*. *Sci Rep*, 2016. **6**: p. 28763.
49. Karashima, Y., et al., *TRPA1 acts as a cold sensor in vitro and in vivo*. *Proceedings of the National Academy of Sciences*, 2009. **106**(4): p. 1273-1278.
50. Saito, S., et al., *Heat and noxious chemical sensor, chicken TRPA1, as a target of bird repellents and identification of its structural determinants by multispecies functional comparison*. *Molecular biology and evolution*, 2014. **31**(3): p. 708-722.

51. Gracheva, E.O., et al., *Molecular basis of infrared detection by snakes*. *Nature*, 2010. **464**(7291): p. 1006-11.
52. Prober, D.A., et al., *Zebrafish TRPA1 channels are required for chemosensation but not for thermosensation or mechanosensory hair cell function*. *Journal of Neuroscience*, 2008. **28**(40): p. 10102-10110.
53. Laursen, W.J., et al., *Species-specific temperature sensitivity of TRPA1*. *Temperature (Austin)*, 2015. **2**(2): p. 214-26.
54. Viswanath, V., et al., *Opposite thermosensor in fruitfly and mouse*. *Nature*, 2003. **423**(6942): p. 822-823.
55. Nagata, K., et al., *Nociceptor and hair cell transducer properties of TRPA1, a channel for pain and hearing*. *Journal of Neuroscience*, 2005. **25**(16): p. 4052-4061.
56. Del Camino, D., et al., *TRPA1 contributes to cold hypersensitivity*. *Journal of Neuroscience*, 2010. **30**(45): p. 15165-15174.
57. Kwan, K.Y., et al., *TRPA1 contributes to cold, mechanical, and chemical nociception but is not essential for hair-cell transduction*. *Neuron*, 2006. **50**(2): p. 277-289.
58. Chen, J., et al., *Species differences and molecular determinant of TRPA1 cold sensitivity*. *Nature communications*, 2013. **4**(1): p. 1-7.
59. Kang, K., et al., *Modulation of TRPA1 thermal sensitivity enables sensory discrimination in Drosophila*. *Nature*, 2012. **481**(7379): p. 76-80.
60. Rosenzweig, M., et al., *The Drosophila ortholog of vertebrate TRPA1 regulates thermotaxis*. *Genes & development*, 2005. **19**(4): p. 419-424.
61. Hamada, F.N., et al., *An internal thermal sensor controlling temperature preference in Drosophila*. *Nature*, 2008. **454**(7201): p. 217-220.
62. Neely, G.G., et al., *TrpA1 regulates thermal nociception in Drosophila*. *PloS one*, 2011. **6**(8): p. e24343.
63. Li, T., et al., *Diverse sensitivities of TRPA1 from different mosquito species to thermal and chemical stimuli*. *Sci Rep*, 2019. **9**(1): p. 20200.
64. Luo, J., W.L. Shen, and C. Montell, *TRPA1 mediates sensation of the rate of temperature change in Drosophila larvae*. *Nature neuroscience*, 2017. **20**(1): p. 34-41.

65. Bullock, T.H. and R.B. Cowles, *Physiology of an infrared receptor: the facial pit of pit vipers*. *Science*, 1952. **115**(2994): p. 541-543.
66. Moparthi, L., et al., *Human TRPA1 is intrinsically cold-and chemosensitive with and without its N-terminal ankyrin repeat domain*. *Proceedings of the National Academy of Sciences*, 2014. **111**(47): p. 16901-16906.
67. Jabba, S., et al., *Directionality of Temperature Activation in Mouse TRPA1 Ion Channel Can Be Inverted by Single-Point Mutations in Ankyrin Repeat Six*. *Neuron*, 2014. **82**(5): p. 1017-1031.
68. Cordero-Morales, J.F., E.O. Gracheva, and D. Julius, *Cytoplasmic ankyrin repeats of transient receptor potential A1 (TRPA1) dictate sensitivity to thermal and chemical stimuli*. *Proc Natl Acad Sci U S A*, 2011. **108**(46): p. E1184-91.
69. Zhong, L., et al., *Thermosensory and nonthermosensory isoforms of Drosophila melanogaster TRPA1 reveal heat-sensor domains of a thermoTRP Channel*. *Cell reports*, 2012. **1**(1): p. 43-55.
70. Yao, J., B. Liu, and F. Qin, *Modular thermal sensors in temperature-gated transient receptor potential (TRP) channels*. *Proceedings of the National Academy of Sciences*, 2011. **108**(27): p. 11109-11114.
71. Clapham, D.E. and C. Miller, *A thermodynamic framework for understanding temperature sensing by transient receptor potential (TRP) channels*. *Proceedings of the National Academy of Sciences*, 2011. **108**(49): p. 19492-19497.
72. Jara-Oseguera, A. and L.D. Islas, *The role of allosteric coupling on thermal activation of thermo-TRP channels*. *Biophysical journal*, 2013. **104**(10): p. 2160-2169.
73. Paulsen, C.E., et al., *Structure of the TRPA1 ion channel suggests regulatory mechanisms*. *Nature*, 2015. **520**(7548): p. 511-7.
74. Nilius, B., J. Prenen, and G. Owsianik, *Irritating channels: the case of TRPA1*. *The Journal of physiology*, 2011. **589**(7): p. 1543-1549.
75. Shi, Y., *A glimpse of structural biology through X-ray crystallography*. *Cell*, 2014. **159**(5): p. 995-1014.
76. Cheng, Y., *Single-particle cryo-EM—How did it get here and where will it go*. *Science*, 2018. **361**(6405): p. 876-880.

77. Taylor, K.A. and R.M. Glaeser, *Electron diffraction of frozen, hydrated protein crystals*. Science, 1974. **186**(4168): p. 1036-1037.
78. Taylor, K.A. and R.M. Glaeser, *Retrospective on the early development of cryoelectron microscopy of macromolecules and a prospective on opportunities for the future*. Journal of structural biology, 2008. **163**(3): p. 214-223.
79. Dubochet, J., et al., *Frozen aqueous suspensions*. Ultramicroscopy, 1982. **10**(1-2): p. 55-61.
80. Adrian, M., et al., *Cryo-electron microscopy of viruses*. Nature, 1984. **308**(5954): p. 32-36.
81. Frank, J., *Averaging of low exposure electron micrographs of non-periodic objects*. Ultramicroscopy, 1975. **1**(2): p. 159-162.
82. Henderson, R., *The potential and limitations of neutrons, electrons and X-rays for atomic resolution microscopy of unstained biological molecules*. Quarterly reviews of biophysics, 1995. **28**(2): p. 171-193.
83. Zivanov, J., et al., *New tools for automated high-resolution cryo-EM structure determination in RELION-3*. Elife, 2018. **7**: p. e42166.
84. Cheng, Y., et al., *A primer to single-particle cryo-electron microscopy*. Cell, 2015. **161**(3): p. 438-449.
85. Böttcher, B., S. Wynne, and R. Crowther, *Determination of the fold of the core protein of hepatitis B virus by electron cryomicroscopy*. Nature, 1997. **386**(6620): p. 88-91.
86. McMullan, G., A. Faruqi, and R. Henderson, *Direct electron detectors*. Methods in enzymology, 2016. **579**: p. 1-17.
87. Li, X., et al., *Electron counting and beam-induced motion correction enable near-atomic-resolution single-particle cryo-EM*. Nat Methods, 2013. **10**(6): p. 584-90.
88. Zheng, S.Q., et al., *MotionCor2: anisotropic correction of beam-induced motion for improved cryo-electron microscopy*. Nat Methods, 2017. **14**(4): p. 331-332.
89. Frank, J., *Three-dimensional electron microscopy of macromolecular assemblies: visualization of biological molecules in their native state*. 2006: Oxford University Press.

90. Scheres, S.H., *A Bayesian view on cryo-EM structure determination*. J Mol Biol, 2012. **415**(2): p. 406-18.
91. Scheres, S.H. and S. Chen, *Prevention of overfitting in cryo-EM structure determination*. Nat Methods, 2012. **9**(9): p. 853-4.
92. Mastronarde, D.N., *Advanced data acquisition from electron microscopes with SerialEM*. Microscopy and Microanalysis, 2018. **24**(S1): p. 864-865.
93. Cheng, A., et al., *Leginon: New features and applications*. Protein Science, 2021. **30**(1): p. 136-150.
94. Lei, J. and J. Frank, *Automated acquisition of cryo-electron micrographs for single particle reconstruction on an FEI Tecnai electron microscope*. Journal of structural biology, 2005. **150**(1): p. 69-80.
95. Carragher, B., et al., *Current outcomes when optimizing 'standard' sample preparation for single - particle cryo - EM*. Journal of microscopy, 2019. **276**(1): p. 39-45.
96. Ohi, M., et al., *Negative Staining and Image Classification - Powerful Tools in Modern Electron Microscopy*. Biol Proced Online, 2004. **6**: p. 23-34.
97. Kastner, B., et al., *GraFix: sample preparation for single-particle electron cryomicroscopy*. Nature methods, 2008. **5**(1): p. 53-55.
98. Naydenova, K., M.J. Peet, and C.J. Russo, *Multifunctional graphene supports for electron cryomicroscopy*. Proceedings of the National Academy of Sciences, 2019. **116**(24): p. 11718-11724.
99. Russo, C.J. and L.A. Passmore, *Ultrastable gold substrates for electron cryomicroscopy*. Science, 2014. **346**(6215): p. 1377-1380.
100. Han, B.-G., et al., *Long shelf-life streptavidin support-films suitable for electron microscopy of biological macromolecules*. Journal of structural biology, 2016. **195**(2): p. 238-244.
101. Noble, A.J., et al., *Routine single particle CryoEM sample and grid characterization by tomography*. Elife, 2018. **7**: p. e34257.

102. Kawate, T. and E. Gouaux, *Fluorescence-detection size-exclusion chromatography for precrystallization screening of integral membrane proteins*. *Structure*, 2006. **14**(4): p. 673-681.
103. Goosen, T.C., D.E. Mills, and P.F. Hollenberg, *Effects of benzyl isothiocyanate on rat and human cytochromes P450: identification of metabolites formed by P450 2B1*. *Journal of Pharmacology and Experimental Therapeutics*, 2001. **296**(1): p. 198-206.
104. Macikova, L., et al., *Putative interaction site for membrane phospholipids controls activation of TRPA1 channel at physiological membrane potentials*. *The FEBS journal*, 2019. **286**(18): p. 3664-3683.
105. Kim, D., E.J. Cavanaugh, and D. Simkin, *Inhibition of transient receptor potential A1 channel by phosphatidylinositol-4, 5-bisphosphate*. *American Journal of Physiology-Cell Physiology*, 2008. **295**(1): p. C92-C99.
106. Marsakova, L., et al., *The First Extracellular Linker Is Important for Several Aspects of the Gating Mechanism of Human TRPA1 Channel*. *Front Mol Neurosci*, 2017. **10**: p. 16.
107. Procko, E., et al., *A computationally designed inhibitor of an Epstein-Barr viral Bcl-2 protein induces apoptosis in infected cells*. *Cell*, 2014. **157**(7): p. 1644-1656.
108. Parsons, L.M., et al., *Glycosylation characterization of an Influenza H5N7 hemagglutinin series with engineered glycosylation patterns: implications for structure-function relationships*. *Journal of proteome research*, 2017. **16**(2): p. 398-412.
109. Oxenoid, K., et al., *Architecture of the mitochondrial calcium uniporter*. *Nature*, 2016. **533**(7602): p. 269-73.
110. Ahuja, S., et al., *Structural basis of Nav1.7 inhibition by an isoform-selective small-molecule antagonist*. *Science*, 2015. **350**(6267): p. aac5464.
111. Shen, H., et al., *Structures of human Nav1.7 channel in complex with auxiliary subunits and animal toxins*. *Science*, 2019. **363**(6433): p. 1303-1308.
112. Hirschi, M., et al., *Cryo-electron microscopy structure of the lysosomal calcium-permeable channel TRPML3*. *Nature*, 2017. **550**(7676): p. 411-414.
113. Zhou, X., et al., *Cryo-EM structures of the human endolysosomal TRPML3 channel in three distinct states*. *Nat Struct Mol Biol*, 2017. **24**(12): p. 1146-1154.

114. Gao, Y., et al., *TRPV1 structures in nanodiscs reveal mechanisms of ligand and lipid action*. *Nature*, 2016. **534**(7607): p. 347-51.
115. Hughes, T.E., et al., *Structural insights on TRPV5 gating by endogenous modulators*. *Nature communications*, 2018. **9**(1): p. 1-11.
116. Yin, Y., et al., *Visualizing structural transitions of ligand-dependent gating of the TRPM2 channel*. *Nat Commun*, 2019. **10**(1): p. 1-14.
117. Yin, Y., et al., *Structural basis of cooling agent and lipid sensing by the cold-activated TRPM8 channel*. *Science*, 2019. **363**(6430).
118. Rohács, T., et al., *PI (4, 5) P 2 regulates the activation and desensitization of TRPM8 channels through the TRP domain*. *Nature neuroscience*, 2005. **8**(5): p. 626-634.
119. Hu, H., et al., *Zinc activates damage-sensing TRPA1 ion channels*. *Nature chemical biology*, 2009. **5**(3): p. 183-190.
120. Bahia, P.K., et al., *The exceptionally high reactivity of Cys 621 is critical for electrophilic activation of the sensory nerve ion channel TRPA1*. *Journal of General Physiology*, 2016. **147**(6): p. 451-465.
121. Zubcevic, L., et al., *Symmetry transitions during gating of the TRPV2 ion channel in lipid membranes*. *Elife*, 2019. **8**: p. e45779.
122. Zubcevic, L., et al., *Conformational plasticity in the selectivity filter of the TRPV2 ion channel*. *Nat Struct Mol Biol*, 2018. **25**(5): p. 405-415.
123. Cao, E., *Structural mechanisms of transient receptor potential ion channels*. *J Gen Physiol*, 2020. **152**(3).
124. Liao, M., et al., *Structure of the TRPV1 ion channel determined by electron cryo-microscopy*. *Nature*, 2013. **504**(7478): p. 107-12.
125. Lin King, J.V., et al., *A Cell-Penetrating Scorpion Toxin Enables Mode-Specific Modulation of TRPA1 and Pain*. *Cell*, 2019. **178**(6): p. 1362-1374 e16.
126. Cao, E., et al., *TRPV1 structures in distinct conformations reveal activation mechanisms*. *Nature*, 2013. **504**(7478): p. 113-8.
127. Suo, Y., et al., *Structural Insights into Electrophile Irritant Sensing by the Human TRPA1 Channel*. *Neuron*, 2020. **105**(5): p. 882-894.

128. Autzen, H.E., et al., *Structure of the human TRPM4 ion channel in a lipid nanodisc*. Science, 2018. **359**(6372): p. 228-232.
129. Zhang, Z., et al., *Structure of a TRPM2 channel in complex with Ca<sup>2+</sup> explains unique gating regulation*. Elife, 2018. **7**: p. e36409.
130. Ritchie, T.K., et al., *Chapter 11 - Reconstitution of membrane proteins in phospholipid bilayer nanodiscs*. Methods Enzymol, 2009. **464**: p. 211-31.
131. Zhang, K., *Gctf: Real-time CTF determination and correction*. J Struct Biol, 2016. **193**(1): p. 1-12.
132. Emsley, P. and K. Cowtan, *Coot: model-building tools for molecular graphics*. Acta Crystallogr D Biol Crystallogr, 2004. **60**(Pt 12 Pt 1): p. 2126-32.
133. Adams, P.D., et al., *PHENIX: a comprehensive Python-based system for macromolecular structure solution*. Acta Crystallogr D Biol Crystallogr, 2010. **66**(Pt 2): p. 213-21.
134. Williams, C.J., et al., *MolProbity: More and better reference data for improved all-atom structure validation*. Protein Sci, 2018. **27**(1): p. 293-315.
135. Goddard, T.D., C.C. Huang, and T.E. Ferrin, *Visualizing density maps with UCSF Chimera*. J Struct Biol, 2007. **157**(1): p. 281-7.
136. Silver, J.T. and E.G. Noble, *Regulation of survival gene hsp70*. Cell Stress and Chaperones, 2012. **17**(1): p. 1-9.
137. Vangone, A., et al., *COCOMAPS: a web application to analyze and visualize contacts at the interface of biomolecular complexes*. Bioinformatics, 2011. **27**(20): p. 2915-2916.
138. Jin, P., et al., *Electron cryo-microscopy structure of the mechanotransduction channel NOMPC*. Nature, 2017. **547**(7661): p. 118-122.
139. Tseng, W.C., et al., *TRPA1 ankyrin repeat six interacts with a small molecule inhibitor chemotype*. Proc Natl Acad Sci U S A, 2018. **115**(48): p. 12301-12306.
140. Buchan, D.W.A. and D.T. Jones, *The PSIPRED protein analysis workbench: 20 years on*. Nucleic acids research, 2019. **47**(W1): p. W402-W407.
141. Sotomayor, M., D.P. Corey, and K. Schulten, *In search of the hair-cell gating spring: elastic properties of ankyrin and cadherin repeats*. Structure, 2005. **13**(4): p. 669-682.

142. Michaely, P., et al., *Crystal structure of a 12 ANK repeat stack from human ankyrinR*. The EMBO journal, 2002. **21**(23): p. 6387-6396.
143. Lee, G., et al., *Nanospring behaviour of ankyrin repeats*. Nature, 2006. **440**(7081): p. 246-249.
144. Zhao, J., et al., *Irritant-evoked activation and calcium modulation of the TRPA1 receptor*. Nature, 2020. **585**(7823): p. 141-145.
145. Zubcevic, L., *TRP Channels, Conformational Flexibility, and the Lipid Membrane*. J Membr Biol, 2020. **253**(4): p. 299-308.
146. Han, Q., et al., *miRNA-711 binds and activates TRPA1 extracellularly to evoke acute and chronic pruritus*. Neuron, 2018. **99**(3): p. 449-463. e6.

## Biography

Yang Suo received Bachelor of Science degree at Shanghai Jiao Tong University in 2013 with Top 1% Bachelor's Thesis honor. In 2013-2014, he was a research assistant in Dabing Zhang's lab in Shanghai Jiao Tong University and Zihao Rao's lab In Tsinghua University, studying the structure and function of plant fatty-acyl reductase. He began his doctoral studied at Duke University in 2014 under the guidance of Dr. Seok-Yong Lee, working on the structural biology of membrane transporters and channels.

### Publications:

Suo, Y., Zhang, F., and Lee, S.Y.. Structural insights into heat sensing by the rattlesnake TRPA1 channel. (Tentative title, manuscript in preparation)

Suo, Y. and Lee S.Y. (2021). Sample preparation of the human TRPA1 ion channel for cryo-EM studies. *Methods in enzymology*, Academic Press. (in press)

Suo, Y., Wang, Z., Zubcevic, L., Hsu, A.L., He, Q., Borgnia, M.J., Ji, R.R. and Lee, S.Y., 2020. Structural insights into Electrophile Irritant Sensing by the human TRPA1 channel. *Neuron*, 105(5), pp.882-894.

Hirschi, M., Herzik Jr, M.A., Wie, J., Suo, Y., Borschel, W.F., Ren, D., Lander, G.C. and Lee, S.Y., 2017. Cryo-electron microscopy structure of the lysosomal calcium-permeable channel TRPML3. *Nature*, 550(7676), pp.411-414.

Daniels, K.G., Suo, Y. and Oas, T.G., 2015. Conformational kinetics reveals affinities of protein conformational states. *Proceedings of the National Academy of Sciences*, 112(30), pp.9352-9357.

Wang, W., Ma, Y., Suo, Y., Yan, L., Zhang, D. and Miao, C., 2014. Crystallization and preliminary crystallographic analysis of defective pollen wall (DPW) protein from *Oryza sativa*. *Acta Crystallographica Section F: Structural Biology Communications*, 70(6), pp.758-760.